Densification of permeable liquids and magmas

Fabian B. Wadsworth

SIGILL. UNIVERSITAT. LUDOVIC. MAXIM.

München 2016

Densification of permeable liquids and magmas

Fabian B. Wadsworth

Dissertation
an der Fakultät für Geowissenschaften
der Ludwig–Maximilians–Universität
München

vorgelegt von
Fabian B. Wadsworth
aus Trowbridge, Wiltshire, Großbritannien

München, den 25. Februar 2016

Erstgutachter: Prof. Dr. Donald B. Dingwell
Zweitgutachter: Priv.-Doz. Dr. Bettina Scheu
Tag der mündlichen Prüfung: 14. Juni 2016

To my Mum.
And to my Dad, who saw the beginning but sadly, not the end.

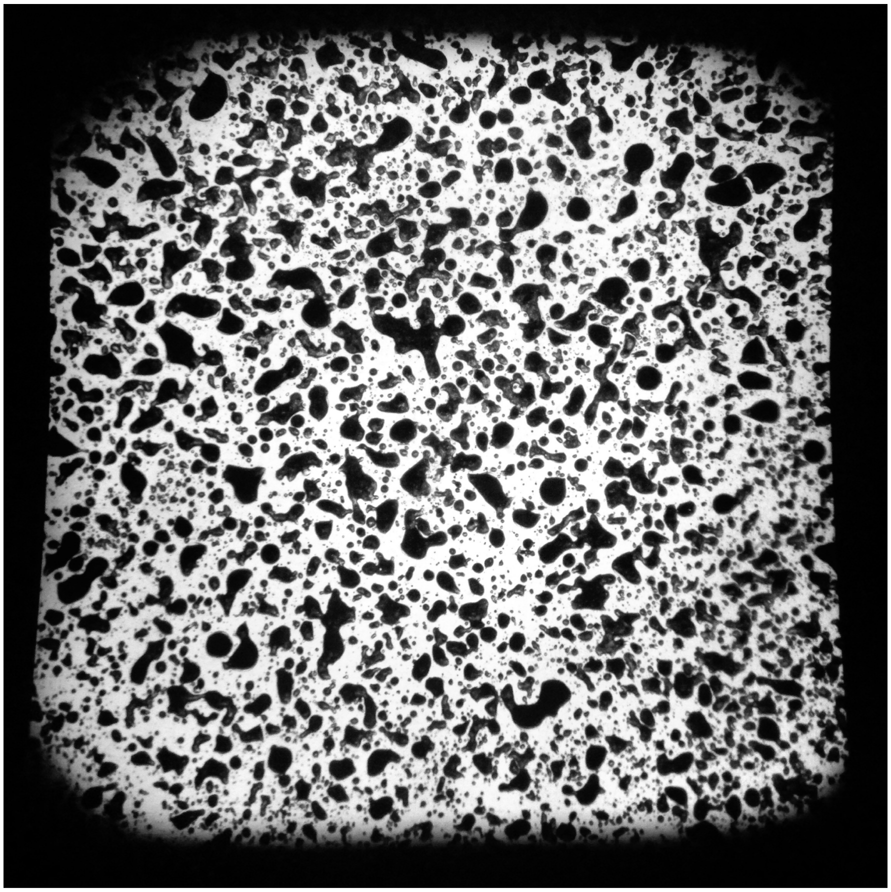

Partially sintered and agglomerated volcanic ash from AD 79 Pompeii, by *Helena Petersen* (in collaboration with Corrado Cimarelli) and exhibited in Munich (2015)

Summary

A central question pertinent to our understanding of volcanic eruptions is: how long can magma remain permeable during shallow ascent? The answer to this complex question has implications for whether or not volcanic plugs can form at the top of silicic conduits and for the longevity of overpressure in magma, which is key to understanding the likelihood that a magma will fragment explosively in eruption. In this thesis a conceptual, and then mathematical framework for addressing this problem is established before experimental data is presented. The mathematical treatment of the problem progresses from processes that affect single droplets and that can be explicitly constrained, such as heat and mass transfer and shape changes in volcanic droplets, before applying these concepts to arrays of many droplets and porous liquids in general. In testing experimental data, a step-by-step approach is taken in which (1) a controlled analogue dataset is used to differentiate the model that best describes the data; (2) the chosen model is extended to more volcanically relevant conditions by testing it against experiments performed using natural materials; and (3) the consequences of the densification process for the time dependence of permeability are assessed. A universal scaling is found between the porosity and the permeability of densifying systems and this is used to calibrate a numerical model for the kinetics of permeability decay in volcanic plugs. Finally, a densification map is provided on which the dominant timescales and lengthscales are compared such that specific volcanic conditions or observations can be plotted to assess whether or not they are consistent with the densification process. In conclusion, it is noted that permeable magmas and viscous liquids in general will densify until an equilibrium volume is reached. This densification is driven by either the surface tension stresses internal to the permeable pore network or by additional external stresses and is limited by the liquid viscosity and the lengthscale of the pores.

All volcanic eruptions are driven by exsolved gas and the buoyancy and pressure they contribute to the system and must be outgassed in either explosive or passive events. While the explosive contribution of magma outgassing has received much attention, the physical process by which passive outgassing, and the resultant densification, occur remains poorly understood. Future work could constrain the

regime in which explosive and passive degassing are coincident and compete to release the gas-pressure built up during the shallowest portions of magma ascent to the Earth's surface.

ZUSAMMENFASSUNG

Eine wichtige Schlüsselfrage für unser Verständnis von Vulkanausbrüchen lautet: wie lange bleibt Magma während des Aufstiegs permeabel? Die Antwort auf diese Frage beeinflusst, ob der Vulkanschlot von einem vulkanischen Plug verschlossen wird und hat Auswirkungen auf die Langlebigkeit des magmatischen Überdrucks, welcher wegweisend für die Explosivität eines Ausbruches ist. Zur Behandlung dieses Problems werden in dieser Arbeit zunächst ein konzeptioneller, sowie ein mathematischer Rahmen aufgespannt, anschließend werden experimentelle Daten gezeigt. Die mathematische Behandlung der Fragestellung führt über vereinfachte Prozesse, die nur einzelne Tropfen betreffen und exakt begrenzt werden können – wie etwa Wärmeübertragung, Stoffübertragung und Formveränderung – zur Anwendung auf eine Anordnung von mehreren Tropen bis hin zu porösen flüssigen Phasen im Allgemeinen. Die schrittweise Vorgehensweise besteht aus (1) der Herausbildung eines Models, welches die Ergebnisse von Experimenten mit Analog Materialien am besten beschreibt, (2) der Erweiterung dieses Models auf vulkanisch relevantere Bedingungen, indem es mit natürlichen Materialien getestet wird und (3) der Auswertung der Auswirkung des Verdichtungsprozesses auf Permeabilität in Abhängigkeit der Zeit. Der durchgängige Zusammenhang zwischen Porosität und Permeabilität während des Verdichtungsprozesses dient zur Kalibrierung eines numerischen Models, welches die Kinetik der Permeabilitätsabnahme in einem vulkanischen Plug berechnet. Eine finale Graphik zeigt die dominanten Zeit- und Längenskalen, auf welcher individuelle vulkanische Bedingungen abgebildet werden können, um zu beurteilen, ob sie mit dem Verdichtungsprozess übereinstimmen. Abschließend wird angemerkt, dass permeable Magmen und viskose Flüssigkeiten im Allgemeinen verdichten bis sich ein Volumen Gleichgewicht einstellt. Angetrieben wird diese Verdichtung entweder von der internen Oberflächenspannung im permeablen Porennetzwerk oder von zusätzlicher externer Belastung. Limitierend auf den Prozess wirken die Viskosität der Flüssigkeit und die Größe der Poren.

Vulkanausbrüche werden von der ausgeschiedenen Gasphase und deren Auftriebskraft und Druck angetrieben, was zur explosiven oder passiven Entgasung führt. Obgleich der explosiven Komponente der Magmenentgasung viel Beachtung geschenkt

wird, bleibt der physikalische Prozess, der zu passiver Entgasung und resultierender Verdichtung führt, unzulänglich verstanden. Zukünftige Forschungsarbeit könnte das Regime untersuchen, in dem explosive und passive Entgasung überlappen und im Wettstreit stehen um den Abbau des Gasüberdrucks, der sich während des Magmen Aufstiegs zur Erdoberfläche aufbaut.

Contents

List of figures

Nomenclature

α	Arrhenius constant $[\mathrm{K}^{-1}]$.
$\bar{\alpha}$	Dimensionless Arrhenius constant.
$\bar{\phi}$	Normalized porosity.
$\bar{C_e}$	Dimensionless water solubility.
$\bar{C_w}$	Dimensionless water concentration.
$\bar{D_T}$	Dimensionless thermal diffusivity.
$\bar{D_w}$	Dimensionless water diffusivity.
$\bar{e}$	Dimensionless water diffusion coefficient.
$\bar{k}$	Normalized permeability.
$\bar{q}$	Dimensionless temperature rate.
$\bar{r}$	Dimensionless radial position.
$\bar{t_b}$	Dimensionless bubble relaxation time.
$\bar{t_n}$	Dimensionless neck formation time.
$\bar{T}$	Dimensionless temperature.
$\bar{t}$	Dimensionless time.
χ	Concentration of a diffusing species.
η_r	Relative viscosity.
Γ	Surface tension $[\mathrm{N\,m^{-1}}]$.
$\hat{o}$	Empirical constant.
κ	Thermal conductivity $[\mathrm{W\,m^{-1}\,K^{-1}}]$.
κ_0	Pore-free thermal conductivity $[\mathrm{W\,m^{-1}\,K^{-1}}]$.
λ_b	Bubble relaxation time [s].
λ_b	Characteristic capillary time [s].
λ_n	Neck formation time [s].
λ_{Da}	Darcy compaction timescale [s].
$\langle \xi^n \rangle$	*nth* moment of the probability density function of ξ.
μ	Liquid viscosity [Pa s].
μ_g	Gas viscosity [Pa s].
Φ	Connected porosity.
ϕ	Porosity.
ϕ_f	Final sample porosity.
ϕ_i	Initial porosity.
ϕ_m	Maximum packing fraction of crystals.
ϕ_x	Volume fraction crystals.
ϕ_{m*}	Maximum packing fraction of spherical crystals.

ψ	A constant in pressure-sintering.
ρ	Liquid density [$\mathrm{kg\,m^{-3}}$].
ρ_f	Pore-fluid density [$\mathrm{kg\,m^{-3}}$].
Eo	Eötvös number.
Oh	Ohnesorge number.
Fo	Fourier number.
Θ	Cylindrical radius [m].
Υ	VFT parameter [Pa s].
Υ_i	VFT parameter [Pa s].
Υ_{ii}	VFT parameter.
ξ	a/R.
A	Sample area in the $\Theta : L$ plane [$\mathrm{m^2}$].
A_i	Initial sample area in the $\Theta : L$ plane [$\mathrm{m^2}$].
a_i	Initial bubble radius [m].
b	VFT parameter [K].
b_i	VFT parameter [K].
b_{ii}	VFT parameter [K].
c	VFT parameter [K].
C_e	Water solubility [wt%].
c_i	VFT parameter [K].
C_p	Specific heat capacity [$\mathrm{J\,kg^{-1}\,K^{-1}}$].
C_{e0}	Solubility parameter [$\mathrm{K^{-1}}$].
C_{ei}	Water solubility at an initial temperature [wt%].
c_{ii}	VFT parameter [K].
C_{pf}	Specific heat capacity of pore fluid [$\mathrm{J\,kg^{-1}\,K^{-1}}$].
C_{wi}	Initial water concentration [wt%].
C_w	Water concentration [wt%].
D	Diffusivity (species not specified) [$\mathrm{m^2\,s^{-1}}$].
d	Empirical constant.
d_i	Empirical constant.
D_T	Thermal diffusivity [$\mathrm{m^2\,s^{-1}}$].
D_w	Diffusivity of bulk water [$\mathrm{m^2\,s^{-1}}$].
d_{ii}	Empirical constant.
D_{T0}	Extrapolated thermal diffusivity at zero temperature [$\mathrm{m^2\,s^{-1}}$].
D_{Ti}	Initial thermal diffusivity [$\mathrm{m^2\,s^{-1}}$].
D_{wi}	Initial diffusivity of water [$\mathrm{m^2\,s^{-1}}$].
e	Empirical constant.
e_i	Empirical constant.
$E_V(\xi)$	Pore nearest neighbour exclusion probability function.
$e_V(\xi)$	Polydisperse form of $E_V(\xi)$.
e_{ii}	Empirical constant.
$F(\xi)$	Cumulative probability density function.
g	Acceleration due to gravity [$\mathrm{m\,s^{-2}}$].
h_n	Radius of curvature of a neck [m].

k	Permeability [m^2].
k_i	Initial permeability [m^2].
L_i	An initial length [m].
L_q	Length of a series of droplets [m].
L_{Da}	Darcy compaction lengthscale [m].
m	Crystal roughness factor.
m'	The Schultz factor.
m_i	Initial sample mass [kg].
N_b	Bubble number density [m^{-3}].
P	External pressure in a sintering system [Pa].
p	Hydrostatic pressure [Pa].
p_n	A set of constants for microstructure constraint.
q	Temperature rate [K s^{-1}].
q_n	A set of constants for microstructure constraint.
R	Particle or droplet radius [m].
r	Radial position [m].
R_i	Initial particle radius [m].
R_n	Inter-particle neck radius [m].
r_p	Aspect ratio of crystals.
R_w	Characteristic length for water diffusion [m].
R_{Fo}	Charateristic Fourier length [m].
S	Specific surface area ratio.
s	Specific surface area [m^{-3}].
T	Temperature [K].
t	time [s].
T_f	Final temperature [K.
T_i	Initial temperature [K.
V	Sample volume [m^3].
V_f	Final sample volume [m^3].
V_i	Initial sample volume [m^3].
y	The vertical position in a cylindrical sample.

Acknowledgments

This long road is ended. Among the multitude to whom I am indebted, I name here but a few, and to my remaining silent partners, I raise my glass in deep thanks.

First, I thank the masters of my guild who have guided my apprentice-hand. That's Don, who has boiled down the magma of the world into a crucible of glass, through which I see things all the more clearly. And Betty, who conspired to give me a chance at this craft and encouraged every endeavour, allowing me to mistake my enthusiasm for wisdom many times and to learn from these moments. Yan, who was instantly a friend and mentor and whose infectious wonder at this volcanic planet is a source of constant inspiration. To Ed who has schooled me at the chalkboard and guided my organisation of the Greek alphabet, patiently, and who has answered my confusions with clarity. Mike, whose taste for the good things has kept me fed with beer and rock-mechanical musing along the way. Hugh, Jon and Ian who took me up to that remote Chilean plateau and initiated me in the mysteries of obsidian. Kai and Ulli, who each have taken me under their wing at some point and who are deeply knitted into my Munich experience; thanks. To Corrado, for taking me along the Guatemalan chain of active volcanoes. To Benewan, who navigated me to Munich and promised it would be worth it: it was! To all these, the elders, I'm truly grateful.

Next, I owe thanks to the journey-people and apprentice-folk with whom I've learned and grown. To Jeremie, Et voilà ! Le prix est partagé entre nous deux. Tu vois les choses sous une lentille disciplinée de clarté, et tu peux métamorphoser les idées en réalité devant mes yeux. Tu m'as appris à rester simple. Ta grande douceur est un océan de calme contagieux. Sans toi, ce travail n'aurait jamais été possible. Jackie, for helping me through the early days with frothy beers flowing and an inspiring example to which to look. Paul, for the ever-kind moments and the ever-bemusing puns. To David, for, among many other things, running by my side through the parks and wildernesses, for the fruits of the gnocchi tree, and for keeping my cup full at all times. To Jenny, who first taught me the whispering secrets of the Bavarian Alps and without whom, I would be lost. And, to the many others with whom I've shared a beer on the way, Kate, Dominik, Jamie, Mathieu, Danilo, Wenjia, Oryaelle, Sebastian, Klaus, Cristian, Guilhem and Donja. Thanks to Helena Petersen for also finding the beauty in sintering textures and providing the *Frontispiece* to this work.

To the Hartingtonians of Liverpool, who took me in, and feasted at the same table for that Winter. Our time was the mid-point of this endeavour and spurred me on. Steve, Oliver, Eva, Gloria and Adrian: the eggs and the hollandaise are ever ready at my home for you.

To Felix, my old friend without whom this was not to be, without whom this would never have begun and on whose shoulders all the blame lies. I often return to our tent by Blue Lake or the slopes of the Tarawera fissure and remember the places whence we come. You taught me the value of learning, knowing for oneself, among countless other Balkan things. I have fallen in love with your Bavaria, as I hope you have with my great English North.

To those who don't live beneath the volcano-eye; these friends who remind me of all the other great things. That's, among so many others, Ralph, Nat, Gianni, Odjbox, Tim, Dorothea, Ivo, Moni, Susanne, Nathan, Marine, Marie, Matthew, Matthias, Jamie, Dunton, Parsons, Edd, MDT, Salv and Nadine. To Goetz and Ike who were the gatekeepers to Munich's wonders and secret places and who reminded me that science can take us only so far, after that there is only music and dancing. To Ray, Jayne and Emily for all the kindness, generosity and warmth that filled me up. And to Rebecca, who was there at the beginning and who folded me in a cherished heritage, in folk music and who taught me the songs I most love, while showing me a voice of my own. Dear thanks.

To Mum and my sister. We bore the loss of our great family man during this thesis and out of that came a shared strength that has spilled into this work. I am ever proud of you both and so lucky to have you be proud of me too.

To my Alexandra. Thank you for everything. You ground and balance me, you share with me, you wrap me up and keep me, you travel the world with me and laugh at it all with me. You feast and dance with me and all of this, we do endlessly. Most importantly, you inspire me in this, and in everything I do. I hope to do it all, with you.

Thank you all.

Preamble

This thesis contains peer-reviewed published work or work in review at the time of writing. Below is a list of publications relevant to this thesis which I have first-authored or to which I have contributed. Where a co-authored publication is used, only my contribution is reproduced herein.

Wadsworth, F.B., Vasseur, J., Llewellin, E.W., Schauroth, J., Dobson, K.J., Scheu, B., Dingwell, D.B. Sintering of viscous droplets under surface tension. *Accepted to Proc. Roy. Soc. A*

[Appears in Chapters 3, 4 & 5]

Kendrick, J., Lavallée, Y., Varley N., **Wadsworth, F.B.**, Lamb, O.D., Vasseur, J. Blowing off steam: Tuffisite formation as a regulator for lava dome eruptions. *Submitted to Front. Earth Sci.*

[Appears in Chapter 4]

Wadsworth, F.B., Vasseur, J., Scheu, B., Kendrick, J.E., Lavallée, Y., Dingwell, D.B. 2016. Universal scaling for fluid permeability during volcanic welding and sediment diagenesis. *Geology.* doi: 10.1130/G37559.1

[Appears in Chapter 5]

Kennedy, B.M., **Wadsworth, F.B.**, Schipper, C.I., Vasseur, J., Jellinek, M., von Aulock, F.W., Hess, K.-U., Russell, K., Lavallée, Y., Nichols, A.R.L., Dingwell, D.B. 2016. Surface tension densifies magma but maintains permeability. *Earth and Planet. Sci. Lett.* doi: 10.1016/j.epsl.2015.10.031

[Appears in Chapter 4]

Heap, M.J., Farquharson, J.I., **Wadsworth, F.B.**, Kolzenburg, S., Russell, J.K. 2015. Timescales for permeability and strength reduction in densifying magma. *Earth and Planet. Sci. Lett.* doi: 10.1016/j.epsl.2015.07.053

[Appears in Chapter 4 & 5]

Wadsworth, F.B., Vasseur, J., von Aulock, F.W., Scheu, B., Lavallée, Y., Hess, K.-U., Dingwell, D.B. 2014. Nonisothermal viscous sintering of volcanic ash. *J. Geo. Res.* doi: 10.1002/2014JB011453.

[Appears in Chapters 2, 3 & 4]

Wadsworth, F.B., Heap, M.J., Dingwell, D.B. 2016. Friendly fire: Engineering a fort wall in the Iron Age. *J. Arch. Sci.* doi: 10.1016/j.jas.2016.01.011

Wadsworth, F.B., Damby, D.E., Hearne, R.L., Le Blond, J., Vasseur, J., Hess, K.-U., Dingwell, D.B. 2015. The feasibility of vitrifying a sandstone enclosure in the British Iron Age. *J. Arch. Sci. Rep.* doi: 10.1016/j.jasrep.2015.06.007

[Referred to in Chapter 6]

Happy were those who dwelt within the eye

Of the volcanos, and their mountain-torch

Lord Byron

1

Introduction

THIS THESIS IS CONCERNED WITH a problem central to volcano-science; namely, how do magmas lose volatile gas? All explosive eruptions on Earth are driven by gas exsolution, which confers buoyancy, drives ascent, builds overpressure and can lead to explosive fragmentation of viscous magma [*e.g.* Gonnermann, 2014;

Gonnermann & Manga, 2007; Alidibirov & Dingwell, 1996; Spieler et al., 2004]. However, it is only recently that the complexities of the final shallowest portion of the magmatic journey to the surface have been appreciated. Most prominently, the realization that magma becomes highly permeable at some point during its ascent [*e.g.* Klug & Cashman, 1996; Mueller et al., 2005], and that volatile phases outgassing from magma conduits contain components that likely come from significant depths [Schipper et al., 2013], implying that, once established, magma permeability may extend over huge lengthscales in magma-filled conduits. The conceptual underpinning of this thesis is that if a hot viscous liquid is highly permeable and connected to the ambient atmosphere, it is unstable and can densify. Speaking broadly, it is this problem which is central to understanding outgassing cycles at the most-dangerous silicic volcanoes because the longevity of permeability dictates the time interval between catastrophic pressure-building events leading to explosions.

1.1 Outgassing: The state of the art

In all models of magma ascent-driven degassing, the traditional view was that bubbles nucleate at a depth at which the magma is sufficiently supersaturated in a volatile phase [Gonnermann & Manga, 2007]. The conceptual model then requires that these bubbles grow during continued ascent and depressurization [Llewellin & Manga, 2005]. For most volcanic scenarios, the viscosity of the bubble walls is sufficient to inhibit equilibrium bubble volumes being attained and the consequence is that the gas pressure rises inside the bubble, exerting high stresses on the surrounding liquid [Prousevitch et al., 1993]. Based on a variety of criteria for the failure of liquids under shear stresses, this can be converted to a critical ascent rate at which bubbles will rupture and fail, which is a fragmentation event thought to be analogous to the mechanisms driving large eruptions [Alidibirov & Dingwell, 1996; Spieler et al., 2004; Gonnermann & Manga, 2007; Mungall et al., 1996]. This scenario of bubbles growing until a critical stress is achieved at the bubble wall when eruption occurs is certainly highly relevant. However, I start from the observation that silicic magmas and the rocks they produce rarely show a textural record of simple bubble growth dynamics. Rather, they typically display complex porous network geometries [*e.g.* Mueller et al., 2005; Shea et al., 2010; Giachetti et al., 2011]. This may be due to the non-zero crystallinity or the high viscosity of the liquid phase preventing simple-geometry gas bubble formation [Oppenheimer et al., 2015]. Whatever the mechanism, these more complex geometries favour the development of permeability compared with a scenario in which spherical growing bubbles coalesce at a critical point that depends on their initial nucleation number density [Blower, 2001]. The state of the art is, therefore, contradictory in that numerical models have focused on the case where bubbles are growing spheres of gas in shells of liquid, while experimental and natural observations have highlighted the shortcomings of such a model.

Permeable magmas for which the liquid phase is viscous are unstable if the gas pressure is not balancing the hydrostatic liquid pressure. For the majority of volcanic scenarios in which large quantities of gas are emitted without coincident magmatic eruption [*see* Edmonds & Herd, 2007], this is likely to be the case.

Then the magma volume may decrease until such a point as the pressures are in equilibrium. There are many observations that are complementary to the view that magma volumes change significantly with time. The best example of this is the concept of shallow plug formation at the top of silicic conduits. This is summarized below.

1.2 Plug formation: There and back again

A key step toward incorporating the fact that permeable magmas must change volume if their gas phase is connected to the low pressure ambient environment, was the concept of densification-driven shallow plug formation [*e.g.* Giachetti et al., 2010; Diller et al., 2006; Clarke et al., 2007; Kennedy et al., 2016]. It is thought that if the shallowest part of a magma-filled conduit can densify in a time-dependent manner, then the plug permeability would decrease and pressure would build beneath such a plug [Diller et al., 2006]. The plug-formation timescale provides a tantalizing candidate for understanding inter-eruptive times. While alternative explanations have been provided for inter-eruptive times [*e.g.* Mason et al., 2006; Costa et al., 2007], plug-formation timescales remain an under-explored constraint ripe for further investigation [Melnik et al., 2005]. The conceptual link between processes that lead to increases in porosity (*e.g.* bubble nucleation and growth) and permeability (*e.g.* bubble coalescence and crack formation), and competing processes which decrease these properties (*e.g.* densification by compaction and sintering), leads to a view of permeability as a dynamic and transient phenomenon that can undergo hysteresis loops during magma ascent [Michaut et al., 2009; Rust et al., 2004].

1.3 A novel concept: Granular liquids and magmas and the origin of obsidian

The final motivating observation is that fragmentation can occur within magma itself and does not necessarily require catastophic failure of the whole magma-filled conduit [Gonnermann & Manga, 2003]. This is congruent with extensive textural work in silicic obsidian showing that discrete veins of often fine-grained pyroclastic material can be preserved in otherwise dense obsidian [Tuffen & Dingwell, 2005]. The veins – often called "tuffisites" – contain the textural record of magma fragmentation, fluidized transport of the resultant particle mixture through hot cracks, deposition and subsequent sintering and densification [Tuffen et al., 2003]. Diffusion of water into these cracks can be used to model timescales of crack closure that show that this occurs rapidly [Castro et al., 2012] and cross-cutting relationships in such veins suggest the process is repetitive during ascent [Tuffen et al., 2003]. Castro et al. [2014] and Cabrera et al. [2011] suggest that this fracturing and localized explosivity is a dominant mechanism for degassing of high-viscosity rhyolitic obsidian. Presumably densification then must be sufficiently efficient to completely heal the fractured and clastic mixture back to a dense glass, obliterating the textural evidence for the fragmentation event altogether. In this framework the tuffisite veins found in surficial deposits of obsidian and in pyroclastic bombs [Tuffen & Dingwell, 2005; Schipper et al., 2013; Castro et al., 2012] are then the final examples that did not reside at high temperature for long enough to completely heal.

A novel concept in this thesis is then that it is a scenario special to magmas in Earth's silicate crust that after fragmentation a particulate granular mixture is produced [Kueppers et al., 2006] and that, if the magma remains hot, this granular material is indeed droplets of high viscosity liquid. The viscosity of these magmas is typically high and in the glass-transition region. The consequence is that the granular material can behave like a particulate mixture or like a viscous densifying array of droplets; a concept that is embodied in the kinetic nature of the glass transition [Dingwell, 1996; Dingwell & Webb, 1990]. In this thesis in many places the definition of volcanic ash as particles or droplets is used interchangeably and the reader should be aware that these terms refer often to the same material. However, this is only done where it is appropriate, such as when referring to scenarios in which the volcanic ash is in fact hot enough to be relaxed on the timescale of observation. Almost all the densification processes discussed herein are for the densification of these granular magmas or array of granular droplets and attention is focused on the regime where the densification is viscous and not elastic or visco-elastic.

The proposal that all obsidian is formed by fragmentation followed by densification in repetitive cycles has consequences for the cyclicity or hysteresis of permeability in those events. Although they are different in detail, it is another central theme of this work that, in essence, the granular (fragmentation of stiff magma) and the vesicular (bubble growth in viscous magma) cases will, once permeable, densify under similar physical processes [Kennedy et al., 2016]. This hypothesis is explicitly tested herein.

1.4 Structure of this thesis

I will outline the methods used, the materials selected and the quantities that are central to the constraints herein but which were not necessarily measured or defined as part of this work (Chapter 2). In doing so I will briefly review work that provides constraint of magma viscosity, diffusivity, surface tension, component solubility, and density. These surveys are not exhaustive as each of these fields is vast, however, these constraints are necessary later in the thesis.

Next, I will guide the reader through the theory that underpins the treatment of experimental data (Chapter 3). The theoretical work is a central part of this wider thesis because previous experimental work on densification has focused on a few foundations, some of which are faulty and corrected here. Where this is the case, I have provided quantification of the errors associated with these faults and advise future investigators as to the limits of applicability of each model.

In Chapter 4, I will present the results of the experimental work that forms the core of this thesis. I will compare these results with the models presented in the previous chapter. Using an analogue dataset, I will determine which model best describes the process of densification before then extending this analysis to a few datasets using natural materials from explosive volcanoes. In doing so, I hope to build a case for the favoured model and where necessary, provide adaptations that boulster its applicability to the widest range of scenarios. I finally present a novel dataset from experiments at a synchrotron facility in which the densification is imaged *in situ*. This final step provides invaluable additional insight into the microstructural evolution of densifying magmas.

Finally, I provide a quantitative discussion in Chapter 5 in which I will review the consequences of densification for permeable outgassing. To do this I first construct an argument for the best relationship between porosity and permeability for rock-forming materials using a large catalogue of published data. In conclusion I provide a densification map that may be of wide utility to volcano-scientists to estimate the timescale involved in the densification of magma at a particular case-locality and I work through what information would be required to use this tool to maximum effect.

...half a mountain shakes off dust
the other half is throwing up.

...on the slopes of Santiaguito volcano,
Guatemala, *by* Adrian Hornby

2

Materials, Methods and Fundamental Quantities

THIS CHAPTER IS CONCERNED WITH THE EXPERIMENTAL METHODOLOGY employed in this thesis, the experimental materials that have been selected, and

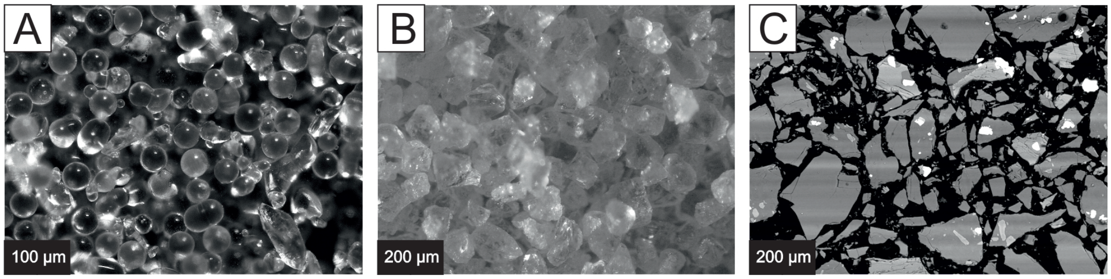

Figure 2.1: Photographs of the experimental materials that are used to explore densification processes in this thesis. (A) Soda-lime silica glass beads. (B) Angular glass powder from either the Deutsche Glastechnische Gesellschaft (DGG) or the National Institute of Standards and Technology (NIST). Here pictured as an example is DGG. (C) A scanning electron microscope image of natural volcanic ash from Volcán de Colima, Mexico.

constraint of parameters that were not measured as part of this thesis but which are essential to understanding the processes here explored. In this constraint of quantities, such as viscosity of a volcanic liquid, I briefly explore and select models that are experimentally validated over the range of conditions used in the experiments in this thesis.

2.1 Experimental materials

This thesis is concerned with the densification of packed volcanic ash and permeable magma. In order to approach this problem, I begin with simple analogue materials before incorporating the complexities associated with using natural, heterogeneous materials. I show example photographs and photomicrographs of the initial sample materials in Figure 2.1.

2.1.1 Glass beads and angular glass fragments

Synthetic silicate glass has advantages over natural glass and volcanic ash particles in that the geometry, chemistry and properties can all be designed to suit the physical process of interest, while maintaining the high viscosity range appropriate to magmatic conditions. To this end, I start with spherical glass beads of a soda-lime-silica composition (from Potters Industries LLC) that have a particle size range 1-250 µm, which can be sieved to discrete fractions if necessary. These beads have a defined geometry which simplifies the comparison with a model derived for a specific geometry (*see* Chapter 3).

Following experimental validation of the models derived herein using the idealized glass bead materials, the problem is extended to angular particles using synthetic, standard glasses from the Deutsche Glastechnicsche Gesellschaft (DGG) and the National Institute of Standards and Technology (NIST). These glasses are provided as blocks or sheets which I then crush carefully by hand using an agate pestle-and-mortar. As with the glass beads, particle sizes can be sieved to desired fractions. The DGG glass (DGG 1) is a soda-lime-silica with a similar composition to the glass beads, and the NIST glass (NIST 717a) is a borosilicate.

As will be shown below in Chapter 2.2.1, these synthetic glass materials do not exhibit evidence for volatile degassing, liquid-liquid immiscibility or crystallization at the temperatures or on the timescales used in this work.

2.1.2 Volcanic ash

Following an exploration of the effects of viscosity, particle size, and particle shape using the standard glasses and the glass beads, natural volcanic ash can be used. In this work volcanic ash from Volcán de Colima, Mexico, was used as a case example. This sample came from an AD 2012 eruption and was collected shortly after eruption. While material properties for the synthetic materials discussed above are measured and repeated here, I rely on the published constraints of the Volcán de Colima found in Kendrick et al. [2013]. Namely, the multi-component viscosity model by Giordano et al. [2008] is used to constrain the temperature dependence of the liquid viscosity and to give an approximate temperature for the glass transition, which matches measurements on the same material made at a nominal heating rate of 10 $\mathrm{K\,min^{-1}}$. The initial dissolved water content of this sample is negligible [Kendrick et al., 2013]

2.1.3 Permeable volcanic pumice

The final material tested is pumice from the 2350 BP Pebble Creek formation of Mt Meager volcano, Canada. This sample was collected from a vent-proximal deposit with characteristic coarse meter-sized pyroclasts. This sample represents an opportunity to test how the models for granular sintering can be extended to initially non-granular, highly porous and permeable materials. As I will show in Chapter 3, the physics involved in the densification process is similar and only distinguished by pore-geometric differences. The initialy dissolved water content of this sample is negligible [Kennedy et al., 2016].

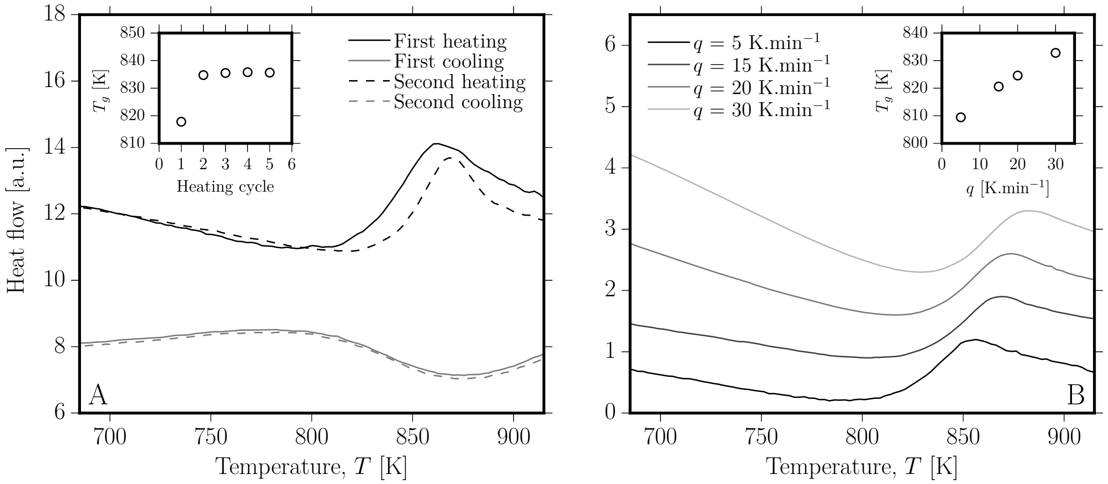

Figure 2.2: Differential scanning calorimetric measurements using a soda-lime-silica glass bead experimental material (Chapter 2.1). (A) The heat flow signal (here reported in arbitrary units) associated with repeat heating and cooling cycles at 10 $\mathrm{K\,min^{-1}}$. On first heating (from an unknown cooling rate of material manufacture) there is an endothermic peak marking the glass transition interval after which the material has relaxed to high viscosity liquid droplets and on subsequent heating the glass transition occurs at higher temperature (*inset*) and is reproducible as long as the thermal history remains the same (repetitively cooled at 10 $\mathrm{K\,min^{-1}}$ before reheating). (B) The shift of the glass transition on first heating at different rates when a fresh sample of glass beads is used for each run.

2.2 Experimental methods

2.2.1 Differential scanning calorimetry & thermogravimetric analysis

For each sample material used (*see* Chapter 2.1), 30-60 mg were loaded into lidded Pt crucibles and heated at a given rate to a desired high temperature. During heating, the heat flow and mass were recorded at high resolution (100-200 pts $\mathrm{K^{-1}}$). This method is appropriate for measuring the temperature or temperature range

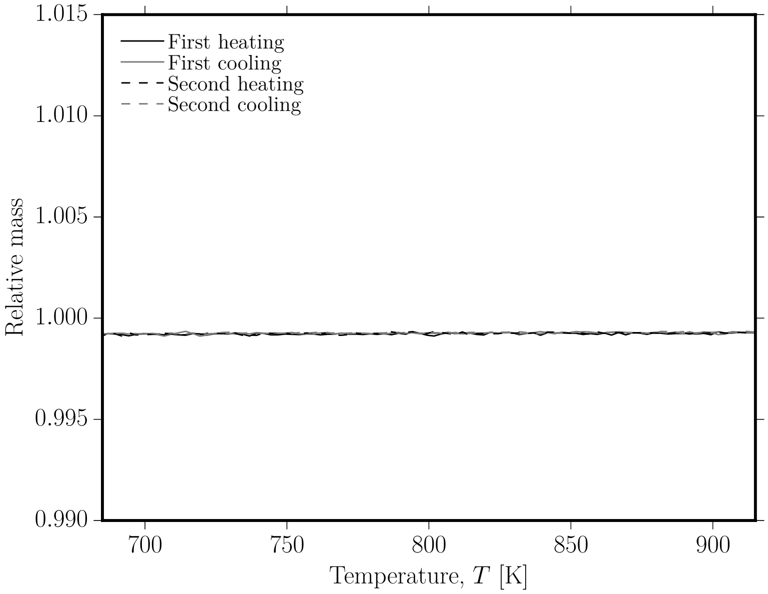

Figure 2.3: The evolution of mass as a function of temperature during linear heating and cooling cycles to high temperature.

over which phase transitions occur (*e.g.* Wadsworth et al. [2015] measure the phase transition from α-quartz to β-quartz by this technique) or over which the structure of an amorphous material relaxes to a liquid configuration [Dingwell & Webb, 1990; Gottsmann et al., 2002]. The valence (endothermic or exothermic) and enthalpy of a transition can be measured by this technique (by using a ratio technique after measuring the heat flow in a sapphire standard crystal under the same imparted thermal history).

Here I report the example of a measurement of the glass beads that were used throughout this thesis as an experimental material (Figure 2.2) where the measurement of the heat flow is not converted to a specific heat capacity as herein the interest is only in knowing the temperature, and not the enthalpy, of a transition.

In Chapter 3 it will become apparent that the glass transition, is a fundamental quantity that is essential to constrain. This is because it represents the temperature range above which a glassy particle, such as a glassy volcanic ash particle, transitions to a viscous droplet that may stick and undergo coalescence with other droplets.

In Figure 2.2 I show how the onset of the glass transition interval, through which the glass particles relax to viscous droplets, is stable when the cooling history of glass-formation is repeated, but shifts when the cooling history is changed. This is the expected finding consistent with a huge body of previous work [*e.g.* Gottsmann et al., 2002; Dingwell & Webb, 1990; Stevenson et al., 1995]. Because the cooling history that was imparted upon material manufacture is consistent, but unknown, when the glass beads are heated at different rates directly from manufacture, their glass transition onset temperature also shifts.

Additional to differential scanning calorimetry, the other thermal analysis technique employed is thermogravimetry, in which samples are similarly prepared but where a mass-balance measures the evolution of sample mass. This is useful to constrain whether a sample contains volatile elements that are released on heating, or whether during a particular phase transition (such as a crystallisation event), mass is gained or liberated. For the glass bead materials the mass is stable over multiple heating cycles to high temperature (Figure 2.3).

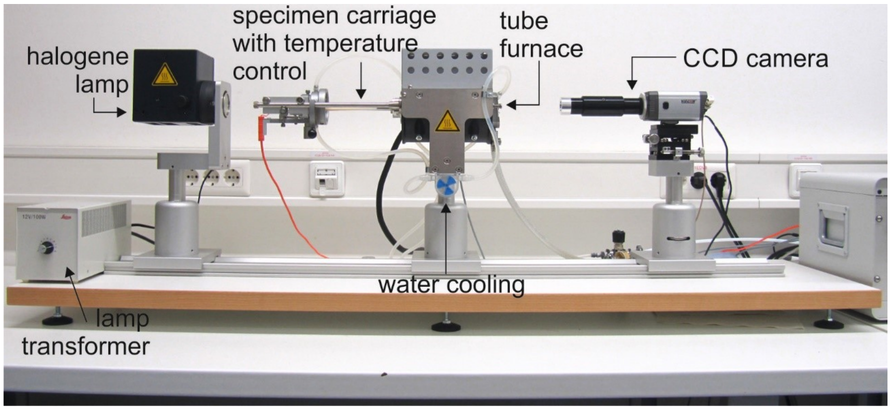

Figure 2.4: A photograph of the optical dilatometer used in this thesis with the main components labelled. *Photograph by* Jenny Schauroth.

2.2.2 Optical dilatometry: A new method for the measurement of sample volume

An optical dilatometer consists of a halogen lamp, a furnace, and a camera in series such that the camera captures an image through the tube-furnace. In the tube furnace a sample is loaded on a carriage (*see* Figure 2.4). The sample image(s) is converted to binary. The camera captures images at 1 Hz and can do so during dynamic heating, or during isothermal holds. The resultant images can then be processed using techniques outlined in this thesis. The temperature is recorded in the furnace casing and also in the sample carriage by S-type thermocouples.

The binary images are processed using a Canny edge detection algorithm, in which the edge of the sample and the basal sample plate surface are detected (*see* Figure 2.5 for an example). In this thesis I am most interested in changes in the geometry of the sample and, most importantly, the sample volume. To extract a volume from the sample edge position data, two techniques can be compared.

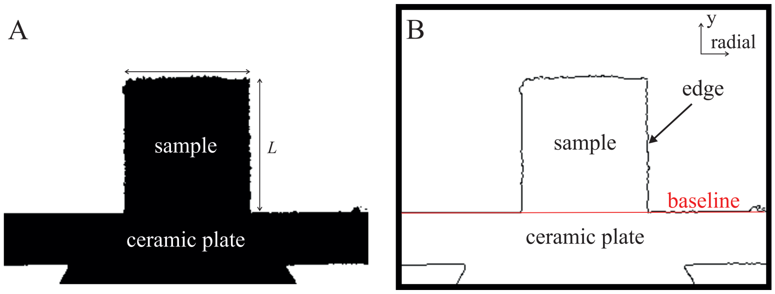

Figure 2.5: (A) A raw binary image of the cross section of a sample (*see* also Figure 4.1. (B) The result of applying the Canny edge detection algorithm to isolate a 1-pixel wide edge position for processing by the solid-of-rotation (Chapter 2.2.2).

In the first method, the sample geometry is assumed to remain unchanged during volume changes. Herein, initially cylindrical samples are used such that this method would assume that any volume changes do not result in deviations from a cylindrical sample shape, and rather the sample cylinder is simply shrinking or growing. The second method is one in which the only assumption made is that the sample maintains a vertical axis of rotational symmetry but that otherwise, the geometry is free to change. Both will be explained and the results from both methods will be compared in Chapter 4.

The cylindrical approximation

Herein the samples are always initially cylindrical and change size or shape with time and temperature. If we assume that the shape changes are minimal, and therefore that the sample maintains approximately cylindrical shape, then we can derive the change in sample volume with time. The cylinder height is L, and the radius is Θ, so that the volume is $V = \pi\Theta^2 L$. When the cylinder shrinks by a factor β from an initial volume, radius and height, V_i, Θ_i and L_i, respectively, then the new volume is $V = \beta^3 \pi \Theta_i^2 L_i$. The cross sectional area in the $R : L$ plane is $A = 2\beta^2 \Theta_i L_i$. The parameter A can be measured continuously and directly from the images and the volume V_i can be found prior to experimentation. Thus we can find a solution for V as a function of V_i and A_i only

$$V = V_i \left(\frac{A}{A_i} \right)^{\frac{3}{2}} \tag{2.1}$$

Sample V in Eq. 2.1 can be then converted to bulk sample porosity ϕ by

$$\phi = 1 - \frac{m_i}{\rho V} \tag{2.2}$$

where m_i is the initial sample mass and ρ is the density of the liquid or the solid component (not the pore-fluid). This approach explicitly assumes that the pore fluid is of negligible mass compared with the liquid (or solid) component, which is the case here where air or argon is exclusively used. In practice, A is measured in squared pixels, not in m^2. Therefore, a conversion is required which will be dealt with when I present experimental results in Chapter 4.

THE SOLID OF ROTATION

While the cylindrical approximation may be useful for the majority of cases, it is not general. Therefore, I here provide a solid-of-rotation method for integrating the detected edges around an axis of symmetry to recover volumes of samples. To do this the radial distance from the axis of symmetry must be integrated as a function of vertical position to give

$$V = \int_0^L \pi \Theta^2 dy \tag{2.3}$$

where y is the vertical position. V can be converted to ϕ as described above. It is sometimes challenging to measure the initial volume for some samples and can be easier to measure the final porosity ϕ_f. This is the case for initially granular, fragile samples. Where this is the case, the porosity at any point can be found knowing the final volume V_f

$$\phi = 1 - \left(\frac{V_f}{V}\right)(1 - \phi_f) \tag{2.4}$$

Results using Eq. 2.1 and those using Eq. 2.3 will be compared in Chapter 4.

2.2.3 X-ray computed tomography

X-ray computed tomography can be used to calibrate the measurements of A by measuring ϕ_f in post-experimental samples. To do this post-experimental samples are mounted onto alumina rods and clamped to a rotation rig. Image radiographs were captured using a Phoenix Nanotom E system operating at 80 kV using a 0.1 mm Cu filter to reduce beam-hardening. 3D data sets were reconstructed from 1440 projections using standard proprietary filtered back projection algorithms and voxel resolutions were 1.42–1.59 µm. Image visualization and analysis were performed using Avizo$^{\text{TM}}$ in which pore volumes were segmented from central regions of each sample to avoid edge effects. Segmentation was performed using a standard gradient-based algorithm using the moments of the intensity distribution. All pores with volumes <125 voxels were discarded from the anaylsis as below this value the error on absolute volume exceeded 5%. Objects of these size classes only comprised 0.06–0.18 vol % of the samples. Pore volumes were then calculated using the remaining segmented pore objects. X-ray tomography forms a volume-calibration in the context of this thesis and does not play a central role, therefore, rendered 3D volumes are not reported.

2.2.4 The TOMCAT beamline at the Swiss Light Source

While X-ray tomography can yield important information about the volume distribution of phases in post-experimental samples, there are potential problems associated with quenching samples. For example, because the methodology described above in Chapter 2.2.2 involves the measurement of A at high temperature and then calibrating these volumes on post-experimental quenched samples, the opportunity to measure the same process *in situ*, recording 3D data sets during densification, is paramount. To address this problem and to gather *in situ* data during rapid volume changes in arrays of liquid droplets (*see* Chapter 5), I also used the TOMCAT beamline at the Swiss Light Source synchrotron. This comprised identical sample preparation as for the optical dilatometry, but on the rotation stage at the Swiss Light Source directly. An alumina sleeve was gently placed over the samples to homogenise the temperature. An in-house designed laser system served to heat the samples and a description of the set up can be found in Fife et al. [2012]; Baker et al. [2012].

2.3 Fundamental quantities

It will become clear in Chapter 3 that in order to understand how the dynamics involved in densification of magmas can be extended from isothermal to non-isothermal conditions, I must first establish how the fundamental properties of magmas vary with temperature. In this section, I'll briefly summarize the most widely-used models for viscosity, thermal diffusivity, the diffusivity of water, density and surface tension in silicate magmas. Where possible, I emphasize that this is not an exhaustive summary and it is not a critical review. Rather these parametrizations are documented for use with the theoretical underpinning that follows in subsequent chapters.

2.3.1 Viscosity

The liquid viscosity μ of silicates is a function of temperature T, composition (most significantly on the dissolved water content C_w) and is a weak function of the hydrostatic pressure P, for low pressures relevant in the upper crust [Hess & Dingwell, 1996].

For synthetic silicate liquids of industrial interest, the generalized composition-dependent Fluegel [2007] model is widely applied. When the composition of the soda-lime-silica glass used in this thesis is input, the Fluegel [2007] model viscosity agrees well with measurements made using an identical composition (Figure 2.6).

The most widely-used models for natural silicate liquids are the Hess & Dingwell [1996] and Giordano et al. [2008] models for calc-alkaline (metaluminous and peraluminous) rhyolitic liquids, such as those implicated in the AD 2008 Chaitén

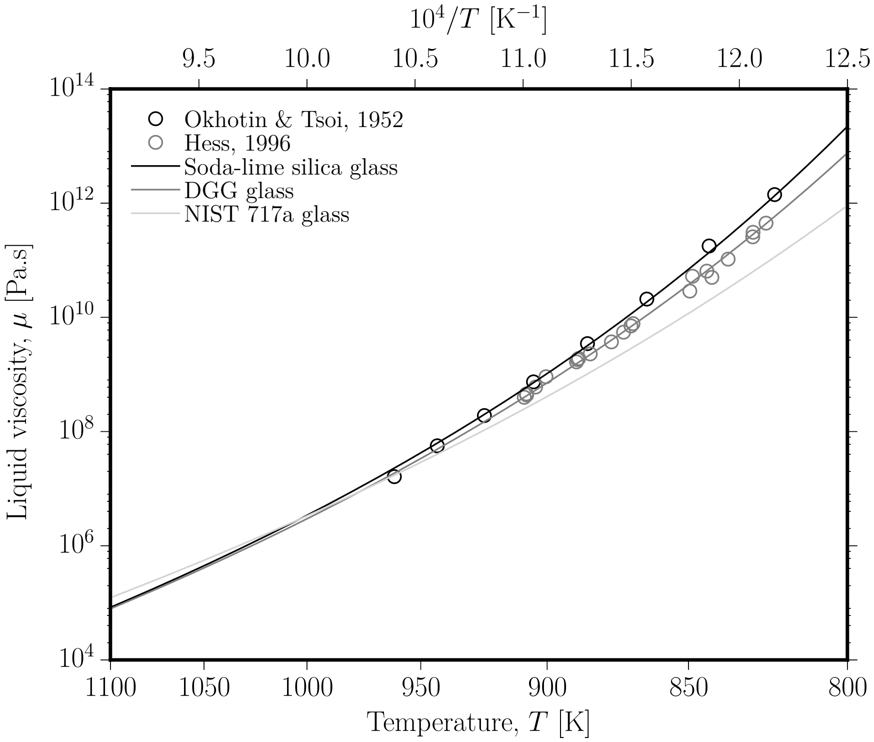

Figure 2.6: The temperature dependence of the liquid viscosity for synthetic compositions used in this thesis. The model lines are from a model for industrial silicate liquids [Fluegel, 2007] and is compared with experimental data for the glass bead samples of soda-lime-silica composition. For the standard glasses (NIST and DGG) the viscosity curves are calibrated by the manufacturing institutions and compared with data from Hess [1996]. In all cases the liquids are nominally anhydrous

eruption Castro & Dingwell [2009], and for general volcanic liquids, respectively.

In all cases, the model takes the form of an experimentally calibrated Vogel-Fulcher-Tammann expression

$$\mu = \Upsilon \exp\left(\frac{b}{T-c}\right) \tag{2.5}$$

for which Υ, b, and c are empirical parameters that are compositionally-dependent

Table 2.1: Examples of the empirical parameters for use with the Vogel-Fulcher-Tammann expression (Eq. 2.5).

Liquid composition	C_{H_2O}	Υ	b	c	viscosity model
–	wt%	Pa s	K	K	–
rhyolite	0.01	4.16×10^{-8}	47216.91	47.18	Hess & Dingwell [1996]
rhyolite	0.1	3.44×10^{-6}	34662.01	121.44	Hess & Dingwell [1996]
rhyolite	1	2.85×10^{-4}	22107.12	195.7	Hess & Dingwell [1996]
basalt*	0	2.82×10^{-5}	11031.45	645.2	Giordano et al. [2008]
basalt*	0.1	2.82×10^{-5}	11109.97	617.8	Giordano et al. [2008]
basalt*	1	2.82×10^{-5}	11337.01	520.1	Giordano et al. [2008]
soda-lime-silica	0	2.3×10^{-3}	9908.85	530.75	Fluegel [2007]
DGG-glass	0	1.52×10^{-3}	10479.06	510.07	Fluegel [2007]
NIST-glass	0	2.75×10^{-3}	11172.6	465.76	Fluegel [2007]

*Composition from [Zhang et al., 1991]

(defined for calc-alkaline rhyolitic liquids below), and T is in units of kelvin. Hess & Dingwell [1996] showed that for calc-alkaline rhyolitic liquids Υ, b, and c are dependent on C_w only, thus, for this class of composition, they rendered Eq. 2.5 independent of cationic composition

$$\begin{cases} \Upsilon = \Upsilon_i C_w^{\Upsilon_{ii}} \\ b = b_i + b_{ii} \ln\left(C_w\right) \\ c = c_i + c_{ii} \ln\left(C_w\right) \end{cases} \tag{2.6}$$

where the empirical constants were defined as $\Upsilon_i = -2.851 \times 10^{-4}\,\mathrm{Pa\,s}$, $\Upsilon_{ii} = 1.918$, $b_i = 22\,107.12\,\mathrm{K}$, $b_{ii} = 5452.52\,\mathrm{K}$, $c_i = 195.7\,\mathrm{K}$, and $c_{ii} = 32.25\,\mathrm{K}$ [*adapted from* Hess & Dingwell, 1996].

A similar approach to the compositional dependence of viscosity is used in the model of Giordano et al. [2008] but where the empirical constants in Eq. 2.5 are

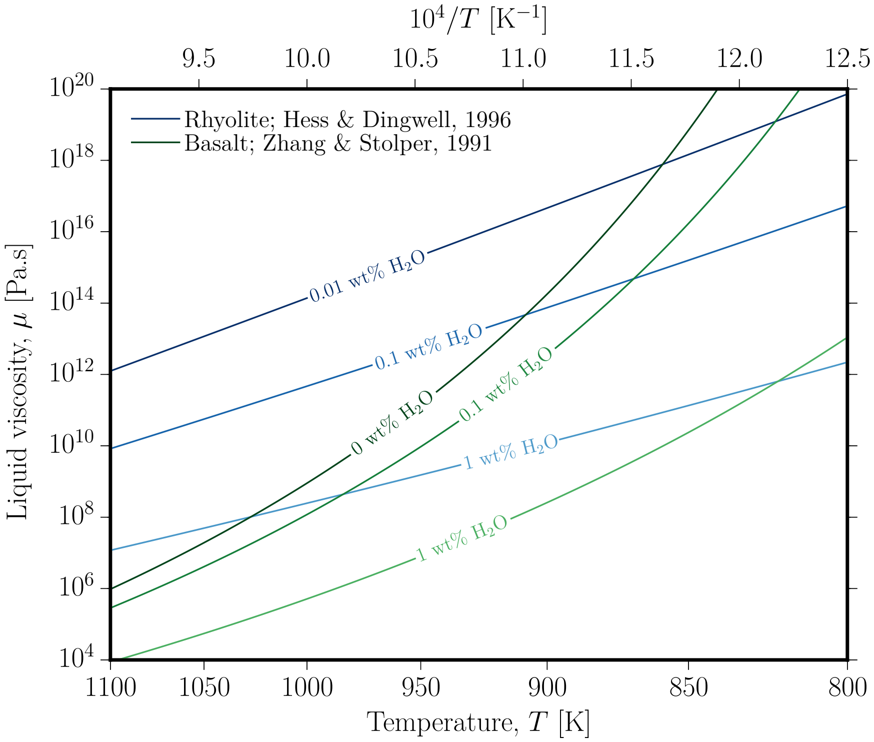

Figure 2.7: The temperature dependence of the liquid viscosity for natural compositions. Results for typical volcanic liquids are shown, including a metaluminous to peraluminous rhyolite with 0.01–1 wt% [Hess & Dingwell, 1996] and typical basalt composition [Zhang et al., 1991] calculated using a more general viscosity model [Giordano et al., 2008]

decomposed into parameters that depend on the partial molar contributions of each cation to the bulk viscosity. The result is more involved than that found in Eq. 2.6 for rhyolites [Hess & Dingwell, 1996] and so is not repeated here. However, the example of the coefficients to be used in Eq. 2.5 for the type-example basalt used in Figure 2.7 is given in Table 2.1.

In Figure 2.7 there are shown the results of Eqs 2.5 & 2.6 for rhyolitic liquid with C_w of 0.01–1 wt% [Hess & Dingwell, 1996] and for a type-example basaltic liquid (from the Juan de Fuca Ridge [Zhang et al., 1991]) for which the normative composition has been recalculated to 100 wt% after incorporation of 0–1 wt% C_w. This composition has then been converted to a temperature-dependent viscosity via the Giordano et al. [2008] model. While other basaltic compositions could be used, this is an illustrative example and I highlight that the degree to which the viscosity is temperature dependent and is strongly dependent on the composition of the liquid. This phenomenon is known as the fragility of the liquid and is discussed later in Chapter 4.

2.3.2 DIFFUSIVITY

It is beyond the scope of this thesis to go into detail about the measurement and conceptual complications involved in diffusivity in silicate liquids. However, as this parameter is used in this thesis, I provide the parametrization for both thermal diffusivity D_T and the diffusivity of water D_w. An example of a complexity that is not addressed but which is certainly worth mentioning, is that the diffusivity of water in silicate melts involves as yet unresolved issues. Namely, there remains a lack of consensus surrounding the relative role of different species of water, most prominently the hydroxyl OH^- and molecular H_2O water species, in the measurements of bulk diffusivities [McIntosh et al., 2014]. This complexity is glossed over here as general solutions for the diffusivity of bulk water are given, rather than a decomposed diffusivity for each species. This is done for simplicity because in order to treat diffusivities of OH^- and H_2O separately, one would have to know the inter-conversion reaction rate as a function of temperature, which is very poorly understood, although attempts have been made to find solutions thereof [Zhang & Ni, 2010]. In both cases of D_T and D_w, the diffusivity is dependent on the absolute concentration of the diffusing species, T and C_w, and D_w is additionally temperature dependent.

THERMAL DIFFUSIVITY

The thermal diffusivity of rhyolites has been measured and parametrized using Little Glass Mountain obsidian (U.S.) [Bagdassarov et al., 1994]. The parametrization of D_T found by Bagdassarov et al. [1994] is in the form of a second-order polynomial dependence on T

$$D_T = 9.14 \times 10^{-7} - 1.4 \times 10^{-9}(T - 273) + 1.9 \times 10^{-12}(T - 273)^2 \tag{2.7}$$

In Chapter 3, it will be shown that this form of D_T is less easy to use than an Arrhenius approximation. Therefore, over the temperature range 300–1200 K, I fit Eq. 2.7 to the following simpler form

$$D_T = D_{T0} \exp{(\alpha T)} \tag{2.8}$$

for which D_{T0} is the extrapolated thermal diffusivity at zero temperature and α is a fitted constant. Over the stated temperature range, I find good agreement between Eq. 2.7 and Eq. 2.8 for values $D_{T0} = 2.61 \times 10^{-7}\,\mathrm{m^2\,s^{-1}}$ and $\alpha = 1.24 \times 10^{-3}\,\mathrm{K^{-1}}$. Although this exponential form for D_T diverges from Eq. 2.7 below $T = 900\,\mathrm{K}$

(Figure 2.8), the experimental data for which it was originally calibrated do not extend below this temperature either. Therefore it is not possible to tell which expression, Eq. 2.7 or Eq. 2.8, is favoured.

Additionally, the thermal diffusivity is a function of the porosity ϕ. While this is a complex topic, simple scaling arguments can be used to decompose D_T into the solid or liquid and the pore components. When using a simple scaling approach such as this, it is implicitly assumed that D_T is a negative function of ϕ. This is most likely the case when the pores are isolated such that the porous liquid or porous solid can be treated as an effective medium through which heat must be conducted. This would not be such a simple case were the pore phase thoroughly interconnected. In the case of interconnected pores, the advection of pore fluid may be sufficient to increase a measured D_T, rather than decrease it, depending on the absolute temperature. This complexity would require knowledge of the pore geometry because the advection is most likely to be convection-driven. For simplicity I show a simple scaling with explicit statement of the limitations thereof. This scaling has been used in thermal problems associated with cooling of large basaltic sills [Connor et al., 1997]

$$D_T = \frac{\kappa}{\rho C_p(1-\phi) + \rho_f C_{pf}\phi} \tag{2.9}$$

where κ is the thermal conductivity, ρ is the solid or liquid matrix density, ϕ is the porosity and C_p is the specific heat capacity. A subscript f denotes a parameter for the pore-fluid rather that the matrix solid or liquid. Parametrization of ρ will be given below. We can take an approximately temperature-independent value of

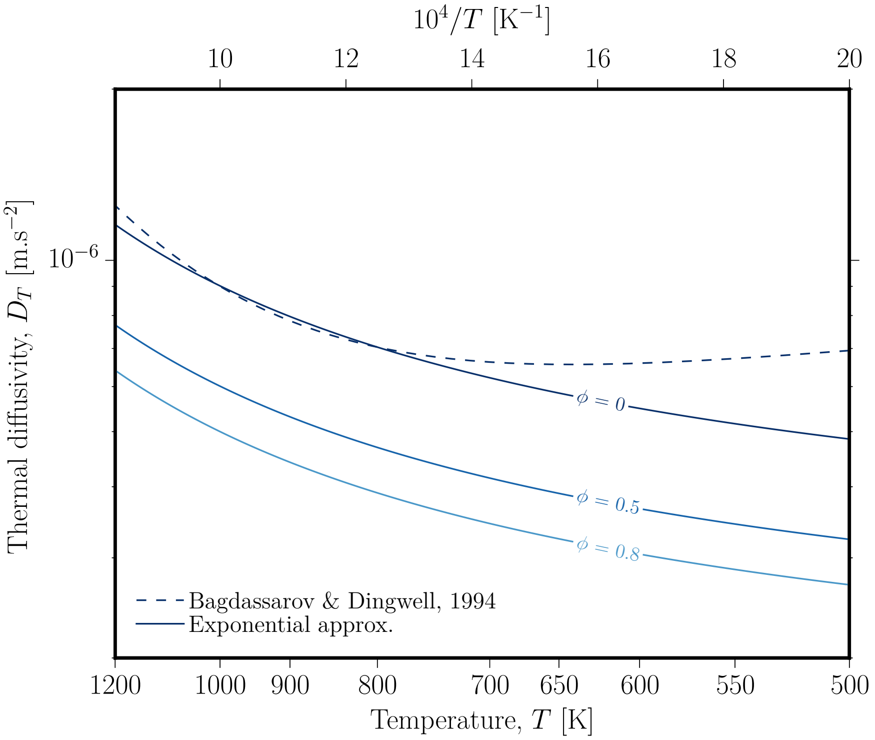

Figure 2.8: The temperature dependence of the thermal diffusivity for rhyolite liquids using the parametrization of Bagdassarov et al. [1994] and the exponential approximation thereof via Eq. 2.7 & 2.8. Additional incorporation of the insulating effect of pores is achieved by using the simple scaling of Connor et al. [1997] via Eq. 2.9 & 2.10.

$\rho_f = 1.275\,\mathrm{kg\,m^{-3}}$ and $C_{pf} = 1007\,\mathrm{J\,kg^{-1}\,K^{-1}}$ for air as the pore fluid.

Use of Eq. 2.9 directly with Eq. 2.8 would imply that κ is not dependent on ϕ directly. However, Bagdassarov et al. [1994] found that κ was indeed dependent on ϕ in the following way

$$\kappa = \kappa_0 \left(\frac{1-\phi}{1+\phi} \right) \tag{2.10}$$

where κ_0 is the pore-free thermal conductivity (*i.e.* that of the volcanic liquid or

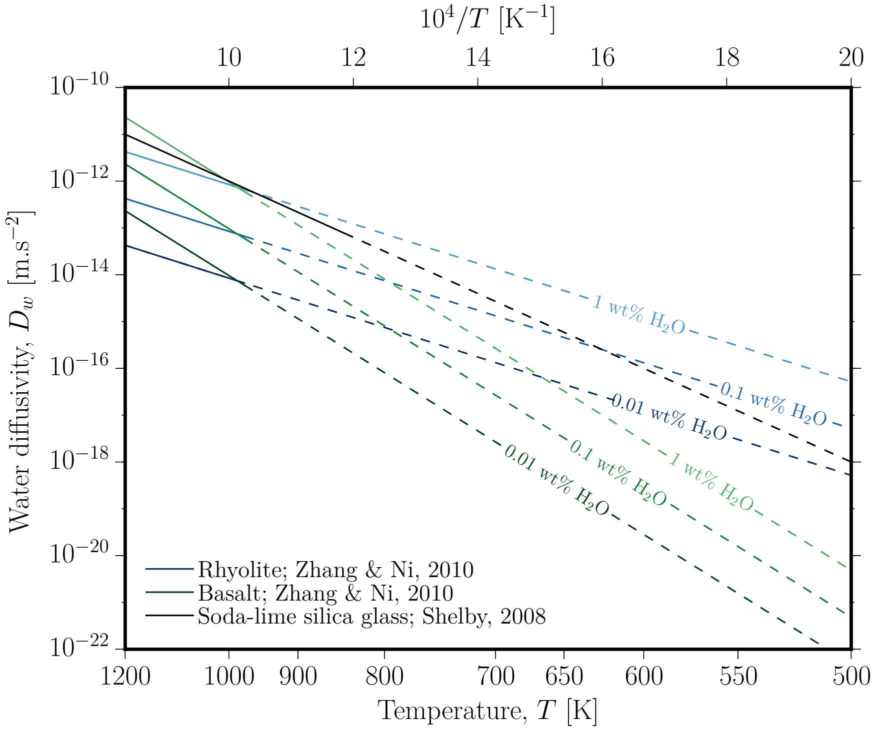

Figure 2.9: The temperature dependence of the diffusivity of bulk water in rhyolite liquids using the parametrization of Zhang & Ni [2010] via Eq. 2.11 & 3.17. Additionally shown are the solutions for variably hydrous basaltic liquids Zhang & Ni [2010] and the soda-lime-silica glass additionally used in this thesis [Shelby, 2008].

solid matrix). This provides the tool kit necessary to find the D_T as a function of T and ϕ, which is provided in Figure 2.8 for this rhyolitic composition (additional parameterization would be possible for other compositions but is not summarized here).

Diffusivity of water in rhyolites

In all silicate liquids, the diffusivity of water is highly dependent on the water concentration C_w and the hydrostatic pressure P as well as T. Using the work of Zhang et al. [2010] and Zhang & Ni [2010] we can cast D_w for the case of rhyolites, which are the best-investigated composition, and find that it is a simple form similar to that of D_T

$$D_w = C_w \exp\left(d - \frac{e}{T}\right) \tag{2.11}$$

for which

$$\begin{cases} d = d_i + d_{ii}p \\ e = e_i + e_{ii}p \end{cases} \tag{2.12}$$

where, for rhyolites, d and e can be decomposed into $d_i = -18.1$, $d_{ii} = 1.888$, $e_i = 9699$ and $e_{ii} = 3626$ [Zhang & Ni, 2010]. While solutions exist for D_w in other liquid systems, it is beyond the scope of this thesis to compile all of them and rhyolites are the most applicable to the processes considered here. In Chapter 3 I will apply Eq. 2.11 to scenarios in which single droplets are hydrated or dehydrated.

2.3.3 Solubility of water

Water is soluble in silicate liquids and bulk water solubility depends on T and P. There are many models for this parameter, however, herein I reproduce one such model that is calibrated for moderate crustal pressures across a wide range of water contents [Lowenstern et al., 2012]. This model is as follows

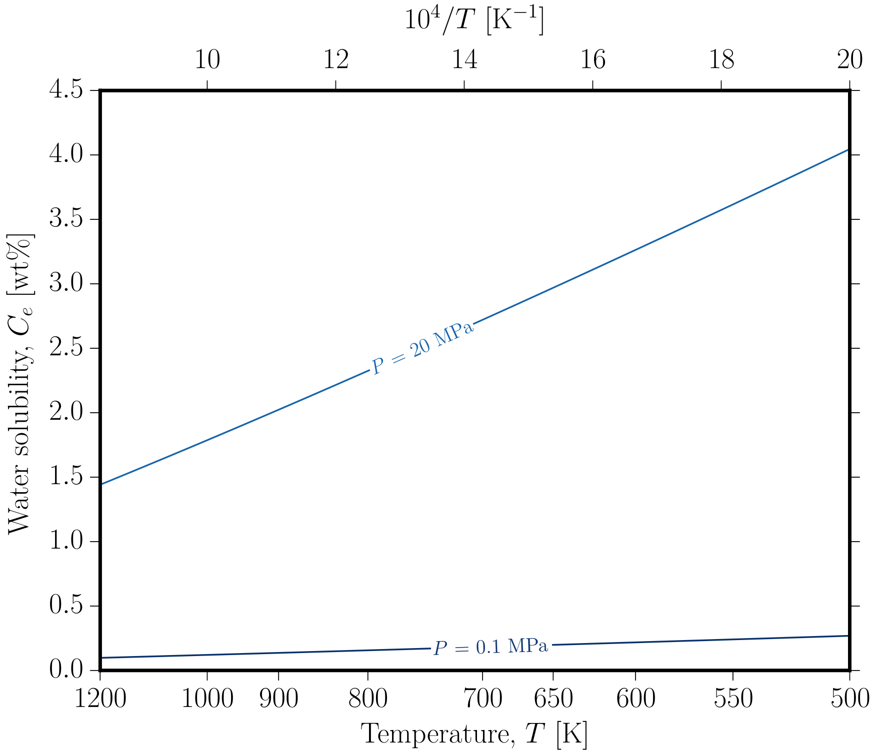

Figure 2.10: The solubility of water in rhyolitic liquids at two example pressures P chosen to represent end member values for the shallowest crustal magmas. These curves are drawn after the model of Lowenstern et al. [2012].

$$C_e = C_{e0} T^{\hat{o}} \tag{2.13}$$

where C_e is related to C_{e0} and to the exponent $\hat{o}$. For 0.1 MPa, C_{e0} and $\hat{o}$ are 353.32 K^{-1} and -1.16, respectively. Similarly at 20 MPa, C_{e0} and $\hat{o}$ are 6156.92 K^{-1} and -1.18, respectively. I note that the negative sign of $\hat{o}$ indicates that the solubility is a negative function of temperature. This is the origin of the observation that exsolved water can be dissolved into silicate melts on cooling, causing the shrinking of isolated bubbles [McIntosh et al., 2014] and the hydration of vol-

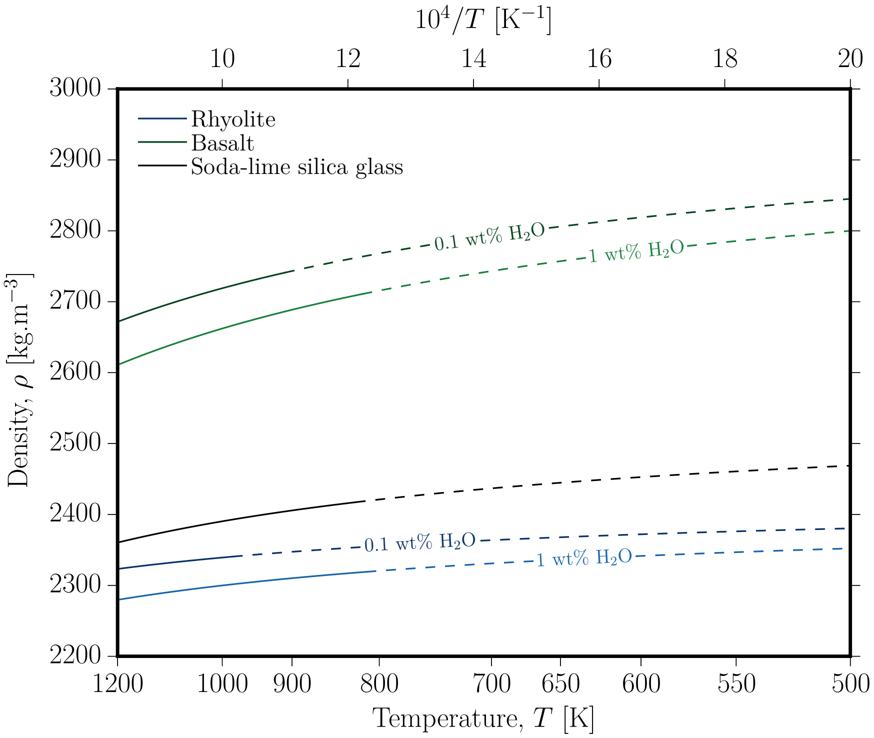

Figure 2.11: The density of type-compositions of silicate liquids of volcanic relevance at $0.1\,\mathrm{MPa}$. The composition of rhyolite is that of Castro & Dingwell [2009], the basalt is that of Zhang et al. [1991] and the soda-lime-silica glass is the experimental material used herein. The density curves are dashed below a temperature at which the material is a glass as these values are for liquid densities only.

canic surfaces [Castro et al., 2012]. This retrograde solubility is also a feature of soda-lime-silica liquids [Shelby, 2008]. This will be discussed further later in Chapter 3.

2.3.4 Liquid density

The density of magmatic liquids has been a topic of prodigious investigation [*e.g.* Lange & Carmichael, 1987; Knoche et al., 1995]. In the context of density, the simplest method to treat these silicate liquids has been to decompose the measured liquid volume into the partial molar volume contributions of each oxide component. This is typically done by systematically varying the liquid composition such that a single value of the partial molar volume can be found from a fitted expression [Dingwell et al., 1988]. As with both the viscosity and the diffusivities discussed above, within a single class of compositions, *e.g.* rhyolites, the role of the dissolved water content is the most significant in changing the liquid density at magmatic conditions. This model comes in the form of a sum of the partial molar volumes of each oxide component. This is not repeated here in detail as this is not a central parameter, but an example is given for the composition of basalt, rhyolite and soda-lime-silica that correspond to the other Figures in this chapter (Figure 2.11).

2.3.5 Surface tension

The interfacial tension Γ between pore fluid and volcanic liquid is a central parameter in this thesis. This has been measured for the case when the pore fluid is air and when the liquid is a silicate. Specifically, values have been reported where the liquid is soda-lime-silica [Wiederhorn, 1969], borosilicate [Kraxner et al., 2009], basalt, andesite, dacite and rhyolite (*see* Table 2.2 for references). These values are summarized in Table 2.2. Furthermore, these values have been found to be broadly temperature independent between T_g and magmatic temperatures [Gardner & Ketcham, 2011].

Table 2.2: Liquid-vapour interfacial tension values for which the vapour composition is air.

Liquid composition –	T K	C_w wt%	Γ $\mathrm{N\,m^{-1}}$	SiO_2 wt%	reference –
basalt	1773	0	0.355	50.28	Walker & Mullins Jr [1981]
basalt	1770	0	0.354	21.29	Walker & Mullins Jr [1981]
basalt	1569	0	0.371	49.66	Walker & Mullins Jr [1981]
andesite	1783	0	0.352	61.79	Walker & Mullins Jr [1981]
limburgite	1772	0	0.348	43.31	Walker & Mullins Jr [1981]
haplogranite	1073	9.26	0.073	78.6	Bagdassarov et al. [2000]
haplogranite	1173	8.9	0.084	78.6	Bagdassarov et al. [2000]
haplogranite	1273	8.9	0.09	78.6	Bagdassarov et al. [2000]
haplogranite	1373	8.91	0.097	78.6	Bagdassarov et al. [2000]
haplogranite	1473	8.92	0.103	78.6	Bagdassarov et al. [2000]
haplogranite	1423	0	0.351	78.6	Bagdassarov et al. [2000]
rhyolite	1423	0	0.282	75.6	Bagdassarov et al. [2000]
rhyolite	1358	4.98	0.088	76.53	Gardner & Ketcham [2011]
rhyolite	1248	4.98	0.087	76.53	Gardner & Ketcham [2011]
rhyolite	1148	4.98	0.078	76.53	Gardner & Ketcham [2011]
rhyolite	1098	4.98	0.078	76.53	Gardner & Ketcham [2011]
rhyolite	1048	4.98	0.088	76.53	Gardner & Ketcham [2011]
dacite	1423	3.51	0.083	66.93	Gardner & Ketcham [2011]
phonolite	1148	5.37	0.061	61.47	Gardner [2012]
phonolite	1423	5.37	0.052	61.47	Gardner [2012]
trachyte	1423	4.5	0.073	62.57	Gardner et al. [2013]
dacite	1423	4.72	0.072	69.85	Gardner et al. [2013]
rhyolite	1423	5.05	0.066	76.53	Gardner et al. [2013]
phonotephrite	1423	4.44	0.072	51.13	Gardner et al. [2013]
basaltic andesite	1423	4.63	0.067	54.12	Gardner et al. [2013]
dacite	1423	3.51	0.065	66.93	Gardner et al. [2013]

Computation is merely the last useful stage of a scientist's activity.

in a letter from C.S. Smith

3

Theoretical framework and numerical predictions

In this chapter I explore the theories underpinning heat and mass transfer in spherical droplets, sintering and densification under surface tension or additional external pressures, and microstructural indicators that can be derived for packings of particles. I show how these principles can be extended to non-isothermal conditions and how the problem can be rendered dimensionless, providing a versatile system of computational tools to compare with experimental data in subsequent chapters. Finally, I provide a case-example of how the principles outlined herein can be used to explore rapid changes in temperature and shape of particles subjected to changes in thermal environment. In all cases simple examples of volcanic relevance are given. As outlined in Chapter 1, throughout this chapter the term ”particle” and ”droplet” are only distinguishable by whether the material state of the volcanic pyroclast is solid and glassy, or viscous and deformable, respectively.

3.1 Heat and mass transfer in spherical particles

In this section I'll deal with a single particle before, in Chapter 3.3, extending these concepts to arrays of many droplets. Heat and mass transfer are first dealt with using Fourier's and Fick's general laws for diffusion. Additional radiative components of heat transfer relevant to high temperature volcanic particles and droplets are then briefly considered. Finally, additional viscous mass transport processes are considered where these are driven by droplet-scale surface tension stresses.

The simplest case of heat or mass transfer is given by Fick's second law, which is a generalization of Fourier's laws for heat conduction. Throughout this thesis I'll assume that in volcanic ash particles and volcanic droplets, the concentration of diffusing species is spherically symmetrical. This means that the problem reduces to 1D, for which in spherical coordinates [Crank, 1975], the diffusion equation is

$$\frac{\partial \chi}{\partial t} = \frac{1}{r^2}\frac{\partial}{\partial r}\left(r^2 D \frac{\partial \chi}{\partial r}\right) \tag{3.1}$$

and this can be used to predict the concentration of a diffusing species χ as a function of time t, radial position r in a spherical particle or droplet, and the diffusivity of the species D. Chapter 2.3.2 gives values of D for the specific case of heat D_T and water D_w diffusion. Here the kinetics of the transfer of these two species will be dealt with in turn.

3.1.1 HEAT TRANSFER

In the most simple cases, heat transfer is conductive, and this is captured well by Fourier's law (a special case of Fick's second law; Eq. 3.1). For heat diffusion, Eq. 3.1 can be recast such that $\chi = T$ and $D = D_T$ and, as originally shown by Fourier, can be decomposed into the contributions of the thermal conductivity κ, the droplet or particle density ρ and the specific heat capacity C_p (*see* Chapter 2.3.2 for details of how these parameters scale when the particle is porous). C_p and ρ can then be extracted from the derivative if we assume that they are much less temperature dependent than κ, which appears to be the case for silicate liquids [Bagdassarov et al., 1994].

$$\frac{\partial T}{\partial t} = \frac{1}{r^2}\frac{\partial}{\partial r}\left(r^2 D_T \frac{\partial T}{\partial r}\right) \tag{3.2}$$

and equivalently, if we decompose D_T into κ, ρ and C_p,

$$\rho C_p \frac{\partial T}{\partial t} = \frac{1}{r^2} \frac{\partial}{\partial r} \left(r^2 \kappa \frac{\partial T}{\partial r} \right) \tag{3.3}$$

If we now make the following substitutions, we can render Eq. 3.2 dimensionless (here a bar above a parameter denotes that it is in dimensionless form)

$$\begin{gathered} \bar{T} = T/T_i \\ \bar{r} = r/R \\ \bar{D_T} = D_T/D_{Ti} \\ \bar{t} = D_{Ti} t/R^2 \\ \bar{\alpha} = \alpha T_i \\ D_{Ti} = D_{T0} \exp(\alpha T_i) \end{gathered} \tag{3.4}$$

where T_i and D_{Ti} are initial values of temperature and diffusivity, respectively, and T_f is the final temperature after the temperature change outside the particle is complete. Using Eq. 3.4 we can give Eq. 3.2 in non-dimensional form

$$\frac{\partial \bar{T}}{\partial \bar{t}} = \frac{1}{\bar{r}^2} \frac{\partial}{\partial \bar{r}} \left(\bar{r}^2 \bar{D_T} \frac{\partial \bar{T}}{\partial \bar{r}} \right) \tag{3.5}$$

and Eq. 2.8 (Chapter 2) becomes

$$\bar{D_T} = \exp\left(\bar{\alpha} (\bar{T} - 1) \right) \tag{3.6}$$

For each individual case of heat transfer processes, the boundary conditions should be posed. A simple, relevant example would be the case in which a volcanic droplet

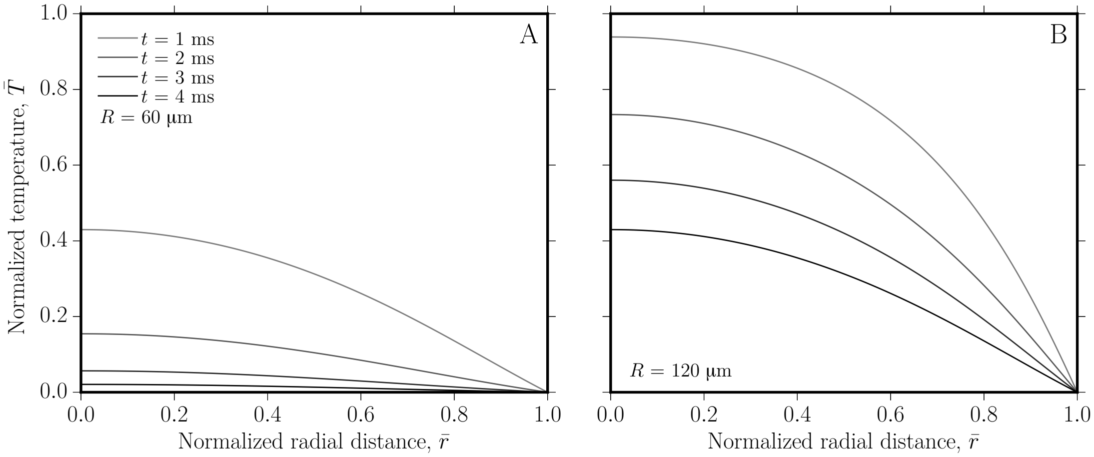

Figure 3.1: Dimensional results for the evolution of temperature internal to rhyolitic volcanic ash particles of two radii; (A) 60 µm and (B) 120 µm. The initial temperature was 1100 K, corresponding to the predicted eruptive temperature the AD 2008 Chaitén eruption [Castro & Dingwell, 2009], and the simulation is designed to replicate the case when a particle is immediately transferred to an environment in which the ambient temperature is 290 K.

is cooling from high temperature toward an ambient value by conduction alone. As a worked example, I'll show this result for a range of particle sizes. For this case, we might consider that the boundary condition at the particle rim ($\bar{r} = 1$) is instantaneously at the ambient value such that $\bar{T} = 0$ at $\bar{t} > 0$. The condition for the centre of the particle must be symmetric and the initial condition might be that of thermal equilibrium in the particle at the initial temperature such that

$$\begin{cases} \partial \bar{T}/\partial \bar{r} = 0 \text{ at } \bar{r} = 0 \text{ for } \bar{t} > 0 \\ \bar{T} = \bar{T}_i = 1 \text{ for all } \bar{r} \text{ at } \bar{t} = 0 \end{cases} \tag{3.7}$$

In Figure 3.1 I give a case example of a spherical rhyolitic volcanic droplet cooling from 1100 K, which was the eruptive temperature for Chaitén volcano in the AD

2008 eruption [Castro & Dingwell, 2009], and I show the thermal profile for a range of times. Eq. 3.4 is used to convert parameters back to the dimensional values, such as t. The most prominent finding of such simple models is that the temperature evolution is strongly dependent on the particle size. This will be summarized below.

Other boundary conditions of interest might be useful to explore. The two addressed here are (1) those often applied in experimental work in which the boundary matches a controlled furnace temperature that is cooling; and (2) those for which the boundary cools dominantly by radiation, rather than by conduction.

In the former case, I define a constant cooling rate as $q = dT/dt$. This can be made non-dimensional as follows

$$\bar{q} = \frac{R^2}{D_{Ti}T_i} q \tag{3.8}$$

The other case of a boundary condition in which radiation controls the flux at the particle rim can be assessed by applying Stefan's law to the boundary; $q = \sigma \epsilon T^4$. Here σ is Stefan's constant and ϵ is the emmissivity. For any value of ϵ we choose at 0.6-0.9, the result is similar.

These two cases for which the particle boundary condition is constant flux, rather than constant temperature, allows us to plot the dependence of the heat transfer problem on the particle size R because we can assess the results at a relevant t. This reference-t is chosen to be the time when the particle rim ($\bar{r} = 1$) reaches a temperature at which the droplet viscosity is sufficiently high that the particle can be considered to be glassy (no longer viscous). This is done via Eq. 2.5

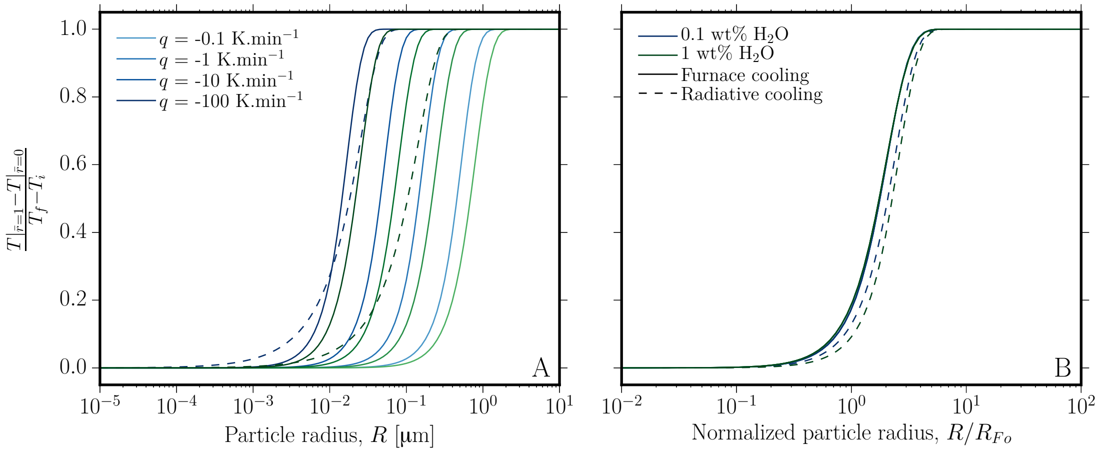

Figure 3.2: A measure of the thermal disequilibrium in a cooling rhyolite droplet as it crosses the glass transtion at its rim $r = R$ under controlled cooling in a furnace environment or during coupled conductive-radiative cooling in an ambient atmosphere. (A) The dependence of the thermal disequilibrium on the particle radius where the small particles are very close to equilibrium temperature throughout whereas large particles preserve a large temperature gradient. (B) The same results for which the particle radius R is normalized to the characteristic Fourier length R_{Fo} showing that the results collapse to a common description of thermal disequilibrium.

and the definition of no longer viscous is taken to be $\mu = 10^{12}$ Pa s. This value is a crude approximation of the glass transition that is appropriate here but not strictly true in detail [Hess & Dingwell, 1996; Gottsmann et al., 2002; Stevenson et al., 1995]. From Eq. 2.6 [Hess & Dingwell, 1996], we have the dependence of this critical μ on T, and also on C_w when assessed at the glass transition for cooling particles. The effect of C_w is to depress the glass transition to lower temperatures, effectively permitting more time for heat transfer to occur before we assess equilibrium or disequilibrium in the particle or droplet.

In Figure 3.2 I show the result of this snapshot in time. This effectively shows us that the temperature difference between the particle rim and the particle centre, captured after cooling to the glass transition region of temperature, is a strong function of the particle size. If this ratio is near to 0, then the particles are in thermal equilibrium throughout the heat transfer process, and if this ratio is near to 1 then the heat transfer process has not penetrated to the centre of the particle. In this latter case, strong thermal gradients are expected in the particle (Figure 3.1). The transitional behaviour, where the ratio is between 0 and 1, means that the heat transfer has penetrated to the particle centre but that there was insufficient time to equilibrate the temperature at that depth in the particle.

It's critical when modelling processes such as heat transfer, that an analytical scaling argument is also posed, as this is more readily useful. So I define a Fourier number as

$$\mathrm{Fo} = \frac{D_T t}{R_{Fo}^2} \tag{3.9}$$

where R_{Fo} is a characteristic length. If $\mathrm{Fo} \gg 1$ then t is insufficient for heat transfer in a particle of R_{Fo} size, while if $\mathrm{Fo} \ll 1$ then t is sufficient for equilibrium temperature to be achieved. If we set Eq. 3.9 to 1 and rearrange for R_{Fo}, we find a Fourier length, which is used in Figure 3.2 as a normalization for the particle radius R. For particles in thermal disequilibrium, we must integrate the temperature over the spatial position in the particle to account for the distribution of temperature dependent parameters; which in this case is D_T. This means that Eq. 3.9 becomes

$$\mathrm{Fo} = \frac{3t}{R_{Fo}^2} \int_0^1 D_T \bar{r}^2 d\bar{r} \tag{3.10}$$

and rearranged to get R_{Fo},

$$R_{Fo} = \sqrt{3t \int_0^1 D_T \bar{r}^2 d\bar{r}} \tag{3.11}$$

The collapse of all curves in Figure 3.2 by use of R_{Fo} demonstrates that Eq. 3.9-3.11 are good scaling methods for heat transfer in spherical particles regardless of the boundary conditions when the temperature change is of volcanic relevance. Additionally, the approach outlined here shows versatility of application in that it is adaptable to lab-environments or natural cases using the boundary conditions discussed (Figure 3.2).

3.1.2 MASS TRANSFER: THE EXAMPLE OF WATER DIFFUSION

As I did with for the heat transfer problem, Eq. 3.1 can be recast to be appropriate for the diffusion of water in a volcanic droplet or particle assuming that D_w is known (*see* Chapter 2.3.2) and where the diffusing species χ is C_w. Then Eq. 3.1 becomes

$$\frac{\partial C_w}{\partial t} = \frac{1}{r^2} \frac{\partial}{\partial r} \left(r^2 D_w \frac{\partial C_w}{\partial r} \right) \tag{3.12}$$

The parameters r, D_w and t can be cast in non-dimensional form as in Eq. 3.4 but were $D = D_w$ instead of $D = D_T$ (for the heat transfer case). The following substitutions are made

$$\begin{aligned}
\bar{C_w} &= C_w/C_{wi} \\
\bar{r} &= r/R \\
\bar{C_e} &= C_e/C_{ei} \\
\bar{t} &= D_{wi}t/R^2 \\
\bar{D_w} &= D_w/D_{wi} \\
\bar{T} &= T/T_i \\
\bar{e} &= e/T_i \\
D_{wi} &= C_{wi}\exp(d - e/T_i)
\end{aligned} \tag{3.13}$$

In which C_e is the equilibrium solubility of water, and C_{ei}, D_{wi} are the water solubility and diffusivity at the initial temperature T_i, and the initial water concentration C_{wi}, respectively. This leads to a new dimensionless form of Eq. 3.12

$$\frac{\partial \bar{C_w}}{\partial \bar{t}} = \frac{1}{\bar{r}^2}\frac{\partial}{\partial \bar{r}}\left(\bar{r}^2 \bar{D_w}\frac{\partial \bar{C_w}}{\partial \bar{r}}\right) \tag{3.14}$$

As with the heat transfer problem, I can use Eq. 3.14 to assess many scenarios of hydration or dehydration of volcanic droplets or particles. In Figure 3.3 I show an illustrative example designed to capture the dehydration of a spherical particle that is instantaneously erupted in a hot plume that is poor in water vapour such that the particle is over-saturated in water with respect to the ambient atmosphere. Here I exploit the intriguing experimental observation that the equilibrium solubility of water in silicate melts is a negative function of temperature in the region of the glass transition (Figure 2.10). This means that when a constant flux of temperature is applied to the boundary of the particle or droplet such that the environment is cooling, water moves into the particle or droplet. This cooling-induced hydration then moves toward equilibrium in the particle and the extent to which equilibrium is achieved by the point when the glass transition is reached at the particle rim is highly dependent on the particle size.

While any temperature profile may be employed, it is most simple to consider an imposed boundary condition at the particle rim such that the temperature flux is constant, via $q = dT/dt$. This can be made non-dimensional as follows

$$\bar{q} = \frac{R^2}{D_{wi} T_i} q \tag{3.15}$$

and Eq. 3.15 can be used to find dimensionless solution solubility law (after Eq. 2.13) such that

$$\bar{C_e} = \bar{T}^{\hat{o}} = (1 + \bar{q}\bar{t})^{\hat{o}} \tag{3.16}$$

and D_w (after Eq. 2.11)

$$\bar{D_w} = \bar{C_w} \exp\left[\bar{e}\left(1 - \frac{1}{1 + \bar{q}\bar{t}}\right)\right] \tag{3.17}$$

Now the system of equations presented in this section can be used to track water movement by diffusion in spherical particles or droplets that are changing temperature. If Eq. 2.13 were cast to include the effect of pressure, which can be done via the model of Lowenstern et al. [2012], then the problem can also be solved for changing pressure environments.

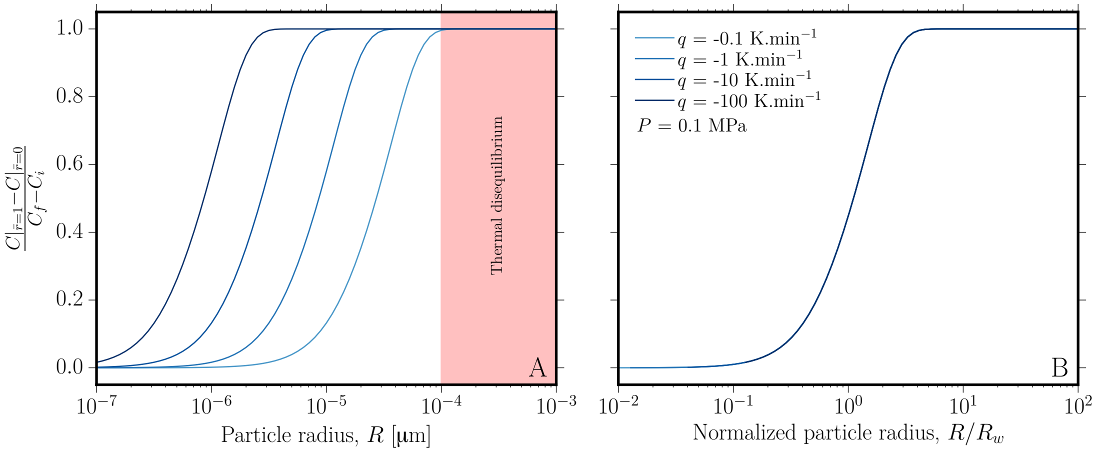

Figure 3.3: Rhyolitic droplets that cool can hydrate due to the negative dependence of water solubility on temperature (here shown for 0.1 MPa but different pressures could be used). (A) The dependence of the final water distribution recorded at the glass transition depending on the cooling rate imposed. Note that all the particle sizes considered here maintain thermal equilibrium during cooling at these rates. (B) The model from (A) where the particle size is normalized by the diffusion length for water.

The boundary and initial conditions are

$$\begin{cases} \partial \bar{C_w}/\partial \bar{r} = 0 \text{ at } \bar{r} = 0 \text{ for } \bar{t} > 0 \\ \bar{C_w} = \bar{C_{wi}} = 1 \text{ for all } \bar{r} \text{ at } \bar{t} = 0 \end{cases} \tag{3.18}$$

and, as stated in Eq. 3.15, the boundary at $r = R$ is given by a constant temperature change.

As with the heat-transfer problem, a characteristic time at which we can assess the distribution of water in the droplets or particles is the time at which the rim of reaches the glass transition. In reality, the droplet or particle may continue to redistribute water and to exchange water with the ambient environment beyond this point, however below the glass transition it remains unclear if the solutions for $D_w(T)$ are valid [McIntosh et al., 2014]. I show the results of solving Eq. 3.14 with Eq. 3.15-3.17 for a range of cooling rates in Figure 3.3. These results are found when the temperature cools to a point where the particle or droplet rim reaches a viscosity of 10^{12} Pa s (again, via Eq. 2.5-2.6). And as before, I find that the right lengthscale by which to normalize the particle radius by

$$R_w = \sqrt{3t \int_0^1 D_w \bar{r}^2 d\bar{r}} \tag{3.19}$$

As a final step, which is pertinent to the problems that are addressed below, the water distribution inside a cooling particle can be converted to a distribution of viscosity via Eq. 2.5-2.6. The spatial integral of the water concentration and the temperature leads to a maximum average viscosity increase that can be expected in the scenario where a cooling particle or droplet is hydrating due to the temperature-controlled increase in solubility. The effect of water concentration on viscosity will be critical in later analysis of vicously limited processes in densification, such as sintering. For now it is sufficient to note that these large gradients of water that can develop in cooling particles and droplets will drastically change the distribution of viscosity in the liquid.

3.2 SCALING SHAPE CHANGES IN SINGLE PARTICLES UNDER SURFACE TENSION

Volcanic ash particles that contain a prodigious liquid phase and are above the glass transition of that liquid are droplets and can change shape by viscous processes. This can occur by deformation of the droplet, for example during flight, or, if the droplet is already deformed or angular, this shape change can occur under

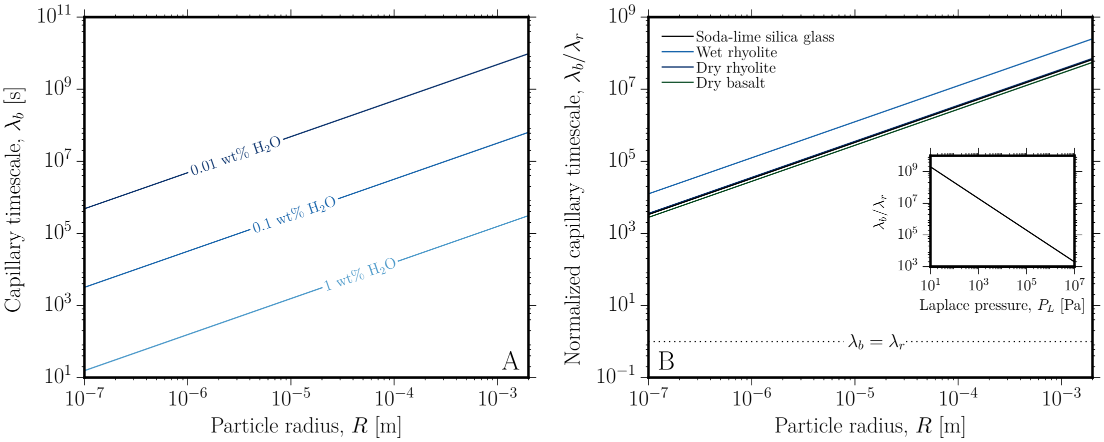

Figure 3.4: The particle size-dependence surface tension-dependent capillary timescale. (A) A case example of rhyolitic droplets based on the example of the AD 2008 eruption of Chaitén volcano. (B) Comparing the capillary timescale in droplets of different size and composition. *Inset:* the Laplace pressure in droplets.

the action of surface tension which rounds the droplet (a relaxation process). I will focus on this relaxation process, which acts on small particles (size-dependence is discussed later) and is characterized by the Capillary timescale λ_b

$$\lambda_b = \frac{\mu R}{\Gamma} \tag{3.20}$$

where Γ is the liquid-vapour interfacial tension. Rounding is then driven by the Laplace surface pressure P_L that acts to minimize the surface area of the droplet. The minimal surface area for a droplet is a sphere. Exact solutions for rounding of an initially arbitrary shaped particle are elusive [Rallison, 1984], however, Eq. 3.20 serves for scaling the time involved in the process. As we are interested here in scaling arguments, we can take P_L for a sphere, for which the principle radii of curvature are equal and so $P_L = \Gamma/2R$ [*e.g.* Prado et al., 2001].

As Γ has been shown to be nominally temperature independent (*see* Table 2.2 and references therein), I can plot the radius-dependence of λ_b as a function of R, showing different results for C_w, assuming again a volcanic liquid relevant to the AD 2008 eruption of Chaitén volcano [Castro & Dingwell, 2009] (rhyolite liquid at $T = 1100\,\mathrm{K}$; Figure 3.4). I note that for $C_w = 1\,\mathrm{wt\%}$ I took the nominally hydrous value of $\Gamma = 0.07\,\mathrm{N\,m^{-1}}$ while for the lower values of C_w I took the anhydrous $\Gamma = 0.3\,\mathrm{N\,m^{-1}}$ (Table 2.2). The differences between these end-member values of Γ are small compared with the large effect of C_w on μ. I also show λ_b normalized by the relaxation timescale of the liquid λ_r, rendering the result independent of any temperature-dependent parameter. Here $\lambda_r = \mu/G_\infty$ where G_∞ is the shear modulus at high frequency and is approximately $10^{10}\,\mathrm{Pa}$ for all silicate liquids [Dingwell & Webb, 1989]. This plot additionally reminds us that relaxation of surfaces of volcanic ash droplets by surface tension is slower than relaxation of the liquid structure, as expected for viscous processes.

The relaxation time for droplets λ_b has been used to scale most surface tension driven processes where the relaxation of shape is to spherical, such that the characteristic length is indeed R. Examples are bubble-relaxation in shear flows [Llewellin et al., 2002; Rust et al., 2003], deformation of viscous droplets in shear flow [Rallison, 1984], and sintering of many viscous droplets in arrays and packings [*e.g.* Prado et al., 2001; Soares et al., 2012]. So far, in this chapter I have shown how temperature and water equilibrium is transient in typical volcanic environments, because both T and C_w affect μ, which is a key parameter in Eq. 3.4. Therefore, if the considerations presented thus far are combined, one can see how

λ_b can be scaled to disequilibrium processes. However, it remains poorly understood how gradients in viscosity affect the stress distribution imparted by surface tension in small droplets [Rallison, 1984] and as such, I limit my argumentation to scaling arguments. In the below Chapter 3.3, I will expand this scaling to prove that it is effective in non-dimensionalizing surface-tension driven sintering on any scale for which the stresses driving particle surface relaxation do indeed arise from Γ.

3.3 Sintering of many viscous droplets

Now that we have the single-particle case for heat and mass transfer and shape relaxation, it's important to extend these analyses to a system in which many viscous liquid droplets are in contact and can interact. In such a case, mass transfer by diffusion or heat transfer by conduction may have to be approximated over the array of droplets, rather than explicitly solved for in each single droplet. Furthermore, in arrays of droplets, mass transfer is dominantly by viscous processes rather than by diffusive processes. This more complex example is the case when volcanic ash particles are deposited in ignimbrites, or in cracks within magma itself [Tuffen et al., 2003; Tuffen & Dingwell, 2005]. The sintering of high viscosity droplets to form a denser, connected mass is important in a range of industrial and natural scenarios, including the fabrication of ceramics [Soares et al., 2012], metals and glass [Prado et al., 2001], the welding of volcanic ash [Lavallée et al., 2015], and the vitrification of Iron Age fortification walls [Wadsworth et al., 2015]. In each case the dynamics may differ because the physical origins of the stresses that drive and oppose sintering may vary, and the materials may be variably heterogeneous. Here I focus on what is commonly called ‘viscous sintering’ – the sintering of two or more viscous droplets in the regime where interfacial tension drives fluid flow – which constitutes a viscous end-member of droplet coalescence problems. The viscous sintering problem has been studied extensively since the early theoretical works of Frenkel [1945] and Mackenzie & Shuttleworth [1949]. More recent studies have built on those works using both experimental [Vasseur et al., 2013; Quane & Russell, 2005; Russell & Quane, 2005] and theoretical constraints [Prado et al., 2001]. Implicit in models of surface-tension driven viscous sintering is that the liquid droplets are in the low Eötvös number and high Ohnesorge number regimes. The Eötvös Eo number is given by

$$\mathrm{Eo} = \frac{\rho g R^2}{\Gamma} \tag{3.21}$$

where g is the acceleration due to gravity and R is the radius of the droplet. For $\mathrm{Eo} \ll 1$, the surface-tension stresses dominate the gravitational stresses acting on the droplet. The Ohnesorge number Oh is given by

$$\mathrm{Oh} = \frac{\mu}{\sqrt{\rho R \Gamma}} \tag{3.22}$$

and for $\mathrm{Oh} \gg 1$, μ is sufficiently high that inertial effects resulting from surface-tension driven motion can be neglected.

In liquid-phase sintering, droplets that share contacts undergo time-dependent coalescence driven by the interfacial tension between the liquid and the ambient fluid in the interstitial pore space. In the high Oh regime Eq. 3.22, this process is dominated by the viscosity of the liquid droplets, and in the low Eötvös number regime Eq. 3.21 the stress driving flow arises from the excess surface pressure P_L, which is proportional to the local radii of curvature. As stated in Chapter 3.2, for spherical liquid droplets, the two principle radii of curvature are equal to one another and to the radius of the droplet so this excess pressure is given by the Laplace general spherical solution $P_L = 2\Gamma/R$. The characteristic timescale associated with viscous flow, driven by interfacial tension, and neglecting inertia and buoyancy, is the general capillary time, given in Eq. 3.20. Normalizing the time of observation t by Eq. 3.20 provides a non-dimensional timescale useful in the characterization of sintering. Frenkel [1945] proposes a model for the growth of necks between particles that share an initial contact, in which the initial radius of the droplet R_i is the characteristic lengthscale in Eq. 3.20, yielding a dimensionless neck formation time (denoted by subscript n)

$$\bar{t_n} = \frac{t}{\lambda_n} = \frac{\Gamma}{\mu R_i} t \tag{3.23}$$

Another model by Mackenzie & Shuttleworth [1949] was derived for the shrinking of pores interstitial to liquid droplets, in which it is the pore or bubble radius a_i that is the characteristic lengthscale, yielding a dimensionless bubble relaxation time (denoted by subscript b)

$$\bar{t_b} = \frac{t}{\lambda_b} = \frac{\Gamma}{\mu a_i} t \tag{3.24}$$

In many scenarios of practical interest, temperature is not constant, but is a function of time. Viscosity is a function of temperature, hence from Eq. 3.20, we see that the capillary relaxation timescale is also a function of temperature, hence also time. Expressing Eq. 3.23 in differential form, we can find the expression for the instantaneous variation in the dimensionless neck formation time as a function of time

$$\frac{d\bar{t_n}}{dt} = \frac{1}{\lambda_n(t)} = \frac{\Gamma}{\mu(T)R_i} \tag{3.25}$$

Integrating, we obtain an expression for the dimensionless neck formation time for non-isothermal conditions

$$\bar{t_n} = \int_0^t \frac{1}{\lambda_n(t)} dt = \frac{\Gamma}{R_i} \int_0^t \frac{1}{\mu(T)} dt \tag{3.26}$$

and similarly for the dimensionless bubble relaxation time

$$\bar{t_b} = \int_0^t \frac{1}{\lambda_b(t)} dt = \frac{\Gamma}{a_i} \int_0^t \frac{1}{\mu(T)} dt \tag{3.27}$$

These integrals can be evaluated if $\mu(T)$ and $T(t)$ are known. For isothermal conditions Eqs 3.26-3.27 reduce to Eqs 3.23-3.24. These considerations permit me to extend the neck-formation model [Frenkel, 1945] and the bubble relaxation model [Mackenzie & Shuttleworth, 1949] to non-isothermal conditions in non-dimensional form, for the first time.

In what follows I will present the model for neck-formation [Frenkel, 1945] and then vented bubble shrinking [Mackenzie & Shuttleworth, 1949]. A schematic of

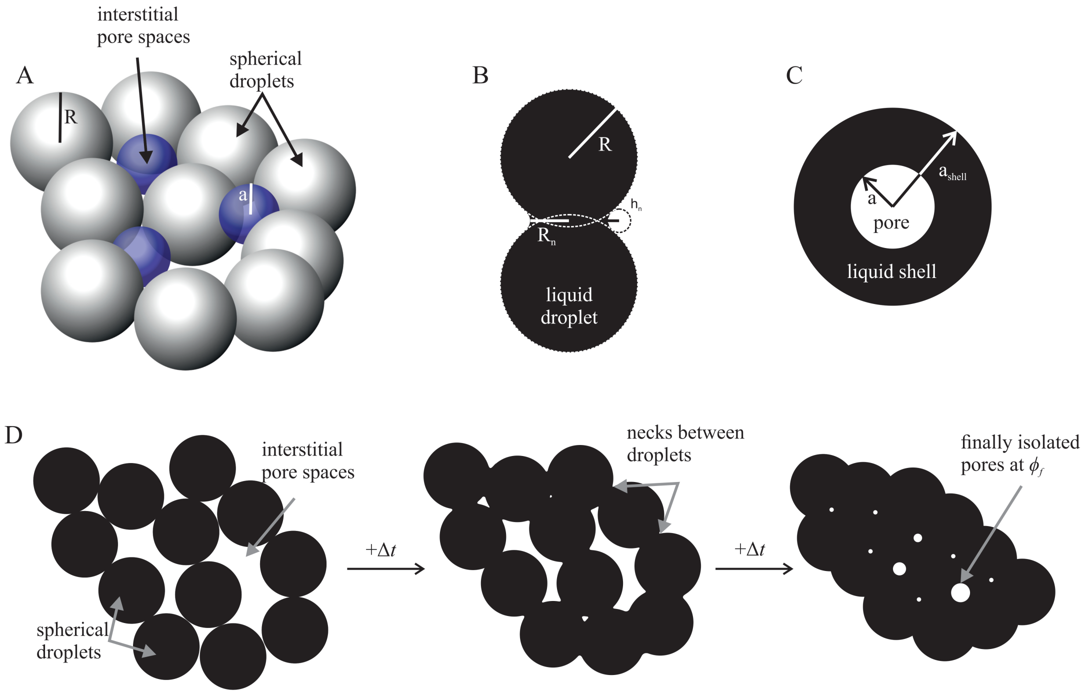

Figure 3.5: A schematic representation of the geometries invoked in the models for sintering end-members of densification described here. (A) A 3D representation of spherical particles or droplets of radius R with interstitial pore spaces which are approximated as equivalent spheres with radius a. (B) The model geometry proposed by Frenkel [1945] in which necks form between droplets. (C) The model geometry proposed by Mackenzie & Shuttleworth [1949] in which a bubble is permeably vented and shrinks. (D) A 2D view of how sintering of droplets evolves with time t.

the geometries used in the model fomulation is provided in Figure 3.5.

3.3.1 The neck-formation model

Frenkel [1945] derives a solution for the growth of the radius of a neck R_n forming between two liquid droplets of equal radius, as a function of time.

$$R_n^2 = \frac{3R_i\Gamma}{2\mu}t \tag{3.28}$$

Kang [2004] proposes that the external radius of the neck region, h_n can be related to R_n and R_i via $h_n \approx R_n^2/(4R_i)$. Combining this approximation with Eq. 3.28 derives a linear shrinkage equation for spheres in series, cast as the length of the system L_q relative to the initial length L_i

$$\frac{\Delta L_q}{L_i} = 1 - \frac{L_q}{L_i} \approx \frac{h_n}{R_i} = \frac{3\Gamma}{8\mu R_i} t \tag{3.29}$$

Prado et al. [2001] extends this analysis to the volumetric isotropic strain in an array of cubically packed monodisperse spheres, deriving a model for the porosity ϕ as a function of time

$$\phi = 1 + (\phi_i - 1)\left(1 - \frac{3\Gamma}{8\mu R_i} t\right)^{-3} \tag{3.30}$$

where ϕ_i is the initial porosity at $t = 0$. Introducing the normalization $\bar{\phi} = \phi/\phi_i$ and using Eq. 3.23, I obtain a dimensionless form of Eq. 3.30

$$\bar{\phi} = \frac{1}{\phi_i} + \left(1 - \frac{1}{\phi_i}\right)\left(1 - \frac{3}{8}\bar{t_n}\right)^{-3} \tag{3.31}$$

If the non-isothermal definition of $\bar{t_n}$ is used (Eq. 3.26) then Eq. 3.31 can be applied to sintering under arbitrary thermal history.

In Figure 4.4 I show the solution to Eq. 3.31. It's clear that the form of this model is such that $\bar{\phi}$ goes to 0 t a finite $\bar{t_n}$.

3.3.2 The vented bubble model

Mackenzie & Shuttleworth [1949] present an idealized model of sintering in which

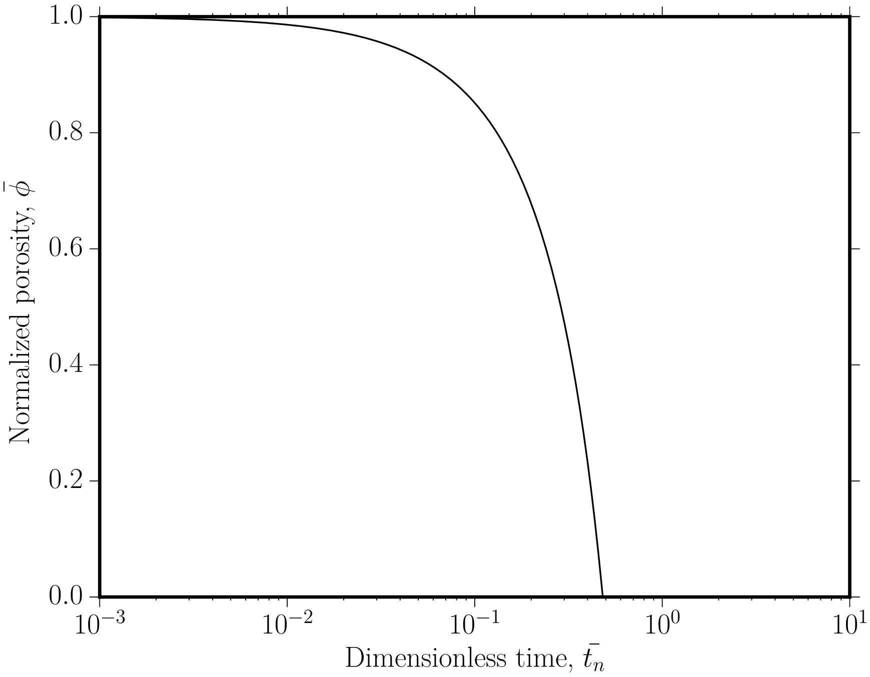

Figure 3.6: The result of the neck-formation model proposed by Frenkel [1945] cast here non-dimensionally and for arbitrary thermal history using Eq. 3.31. Note that this model predicts that $\bar{\phi}$ is a decreasing function of $\bar{t_n}$ and the characteristic length is the initial particle radius R_i.

the interstitial, gas-filled pore-space surrounding the droplets is represented as an array of spherical bubbles, evenly distributed throughout the liquid. Each bubble of radius a sits in a spherical liquid shell of radius a_s, and shrinks under the action of the surface tension between bubble and liquid. They derive an expression for the evolution of the bulk density of the bubble–shell unit as a function of time. In this scenario the gas is assumed to be able to escape freely (despite the lack of physical escape routes) so we term this the 'vented bubble' model. Conceptually, the formulation is very similar to that used in studies of the growth of bubbles in magma [Proussevitch et al., 1993]. The Mackenzie & Shuttleworth [1949] solution can be cast as a rate of change of porosity to give

$$\frac{d\phi}{dt} = -\frac{3\Gamma}{2\mu}\left(N_b\frac{4\pi}{3}\right)^{\frac{1}{3}}\phi^{\frac{2}{3}}(1-\phi)^{\frac{1}{3}} \tag{3.32}$$

where N_b is the bubble number density in the system. I find it convenient to recast N_b in terms of the initial porosity ϕ_i via the equivalence $N_b 4\pi a_i^3/3 = \phi_i/(1-\phi_i)$, to give

$$\frac{d\phi}{dt} = -\frac{3\Gamma}{2\mu a_i}\left(\frac{\phi_i}{1-\phi_i}\right)^{\frac{1}{3}}\phi^{\frac{2}{3}}(1-\phi)^{\frac{1}{3}} \tag{3.33}$$

which carries the implicit assumption that N_b is constant throughout the sintering process. As with the Frenkel [1945] model, I normalize ϕ by ϕ_i and here I use Eq. 3.24 to obtain a dimensionless form of Eq. 3.8

$$\frac{d\bar{\phi}}{d\bar{t_b}} = -\frac{3}{2}\left(\frac{1-\phi_i\bar{\phi}}{1-\phi_i}\right)^{\frac{1}{3}}\bar{\phi}^{\frac{2}{3}} \tag{3.34}$$

As before, if the non-isothermal definition of $\bar{t_b}$ is used (Eq. 3.27) then Eq. 3.47 is applicable to sintering under arbitrary thermal history.

The differential equations above cannot be cast as simple, analytical functions of time or temperature. However, if I make the simplifying assumption that $\phi \ll 1$ so that Eq. 3.47 becomes

$$\frac{d\bar{\phi}}{d\bar{t_b}} = -\frac{3}{2}\frac{\bar{\phi}^{\frac{2}{3}}}{(1-\phi_i)^{\frac{1}{3}}} \tag{3.35}$$

and this simplified form can be integrated subject to the initial condition that

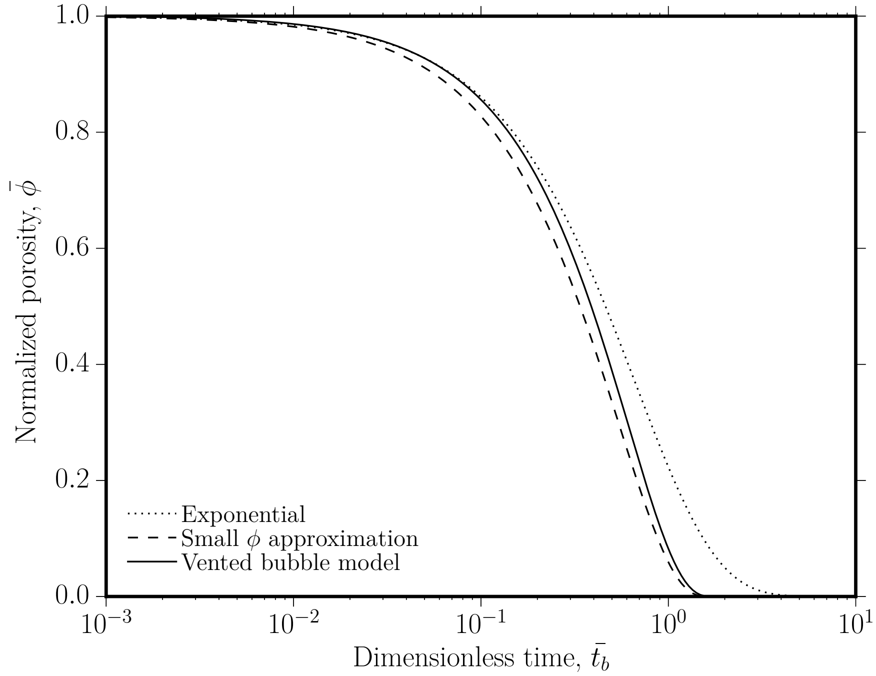

Figure 3.7: The result of the bubble relaxation models for viscous sintering propsed by Mackenzie & Shuttleworth [1949] and cast here in non-dimensional form by Eq. 3.47. Additionally shown are the approximations for when $\bar{\phi}$ is small (Eq. 3.36) and when the commonly-used exponential solution is used (Eq. 3.40).

$\bar{\phi} = 1$ at $\bar{t_b} = 0$ to give

$$\bar{\phi} = \left(1 - \frac{1}{2(1-\phi_i)^{\frac{1}{3}}}\bar{t_b}\right)^3 \tag{3.36}$$

which I will call the "small-ϕ approximation". In Figure 3.7 solutions to the vented bubble model and the small-ϕ approximation are shown.

3.3.3 An exponential approximation

Chiang et al. [1997] make the observation that the relationship $N_b 4\pi a^3/3 =$

$\phi/(1-\phi)$ allows the Mackenzie & Shuttleworth [1949] vented bubble model to be simplified to give

$$\frac{d\phi}{dt} = -\frac{3\Gamma}{2\mu a}\phi \tag{3.37}$$

Note that this formulation uses the time-dependent bubble radius and porosity a & ϕ rather than the initial radius and porosity a_i & ϕ_i that are used in Eq. 3.8. Consequently, non-dimensionalization requires the use of a modified bubble relaxation time in which the radius is a function of time. Following the approach outlined earlier, I couch $\bar{t_b}(t)$ in differential form, then integrate to find

$$\frac{d\bar{t_b^*}}{dt} = \int_0^t \frac{1}{\lambda_b(t)}dt = \Gamma\int_0^t \frac{1}{\mu a(t)}dt \tag{3.38}$$

where superscript * indicates that a is a function of time. Again, if μ is taken to be a function of time, then this can account for non-isothermal conditions. The dimensionless form of Eq. 3.38 then reduces to

$$\frac{d\bar{\phi}}{d\bar{t_b^*}} = -\frac{3}{2}\bar{\phi} \tag{3.39}$$

permitting an analytical solution with an exponential dependence of $\bar{\phi}$ on $\bar{t_b^*}$

$$\bar{\phi} = \exp\left(-\frac{3}{2}\bar{t_b^*}\right) \tag{3.40}$$

Eq. 3.40 is of little practical use as $a(t)$ is not known *apriori*. Nonetheless, it is the most widely-used model for viscous sintering [Prado et al., 2001; Soares et al.,

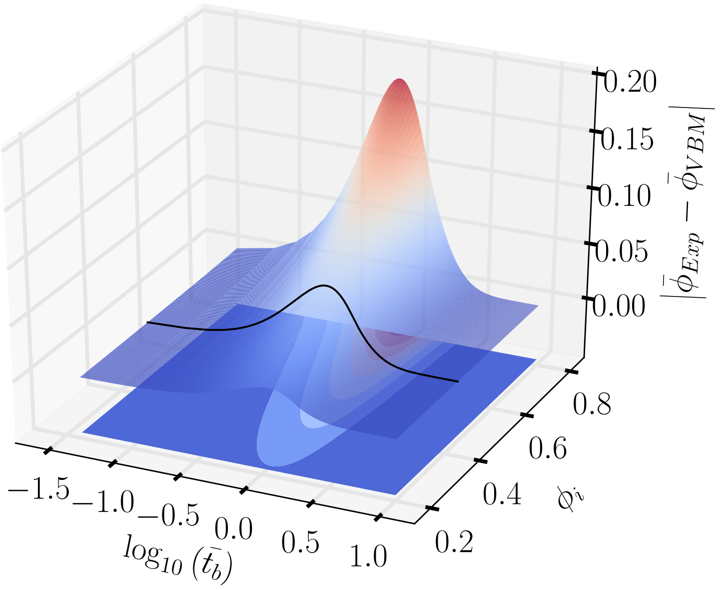

Figure 3.8: The mismatch between the vented bubble model [Eq. 3.47 Mackenzie & Shuttleworth, 1949] and the exponential model [Chiang et al., 1997; Prado et al., 2001]. This plot serves to demonstrate that while the mismatch is small at low initial porosities, if samples of permeable bubbly liquid were used with ϕ_i near to 1, then the exponential model would not be a good approximation, despite its ubiquitous application [e.g. Prado et al., 2001; Soares et al., 2012]. The black line indicates the initial porosity typically used in sintering experiments. I note that much larger initial porosities are expected for volcanic pumice, for example.

2012; Prado et al., 2003a]. This model also appears in Figure 3.7 for reference. In Figure 3.8 I show that while the exponential approximation (Eq. 3.40) may provide good agreement with the vented bubble model (Eq. 3.47) at low initial porosities typical of packed granular media, for higher porosities the discrepancy is much larger and thus the exponential approximation is inappropriate.

3.3.4 Non-zero final porosity

It is a common observation that the porosity of a sintered mass does not reach zero, but instead approaches a final porosity ϕ_f [Prado et al., 2001; Soares et al., 2012; Prado et al., 2003a; Eberstein et al., 2009]. This will be discussed in Chapter 4, but I provide here a semi-empirical extension of the sintering models that have gone before in light of this expectation by substituting $\phi - \phi_f$ for ϕ and $\phi_i - \phi_f$ for ϕ_i in the system of equations. The normalisation of ϕ then becomes $\bar{\phi}^* = (\phi - \phi_f)/(\phi_i - \phi_f)$, and Eqs 3.47, 3.36 & 3.40 become

$$\frac{d\bar{\phi}^*}{d\bar{t_b}} = -\frac{3}{2}\left(\frac{1-(\phi_i-\phi_f)\bar{\phi}^*}{1-(\phi_i-\phi_f)}\right)^{\frac{1}{3}} \bar{\phi}^{*\frac{2}{3}} \tag{3.41}$$

$$\bar{\phi}^* = \left(1 - \frac{1}{2(1-(\phi_i-\phi_f))^{\frac{1}{3}}}\bar{t_b}\right)^3 \tag{3.42}$$

$$\bar{\phi}^* = \exp\left(-\frac{3}{2}\bar{t}_b^*\right) \tag{3.43}$$

This empirical adjustment is not strictly consistent with the derivation of the models; nonetheless, I expect that any loss of fidelity will be inconsequential for the small ϕ_f values expected. This will be tested in Chapter 4.

3.3.5 The case when the pore-fluid pressure is not equal to the liquid pressure

The derivation provided by Mackenzie & Shuttleworth [1949] for the vented bubble model starts from the valid and necessary assumption that the pore fluid pressure is in equilibrium with the pressure of the sintering liquid droplets. However, in many scenarios of practical, volcanic interest, the pressures of the liquid phase (the droplets) and the pore-phase (exsolved gases) are not equal. In this scenario, surface tension may not be the dominant force acting to change the bulk volume of the system. This would include scenarios where Eo (Eq. 3.21) is much larger than unity. For example, the pore phase may be overpressured relative to the liquid phase and in this scenario volume of the system may increase, not decrease. Conversely, if the pores are underpressured, such that the liquid pressure is under an external hydrostatic load, then the pore shrinking and bulk volume decreases may be faster than in the case where surface tension is dominant. To address these two additional scenarios, I explore the incorporation of pressure in the sintering theory. However, I note that these propositions will not be experimentally tested in this thesis and therefore, while they are posed rigorously, they remain unvalidated thus far. In lieu of validation, I will discuss caveats to this approach and state the bounds of applicability of this part of my theory of sintering.

Pressure can be incorporated by defining the following ratio of an external

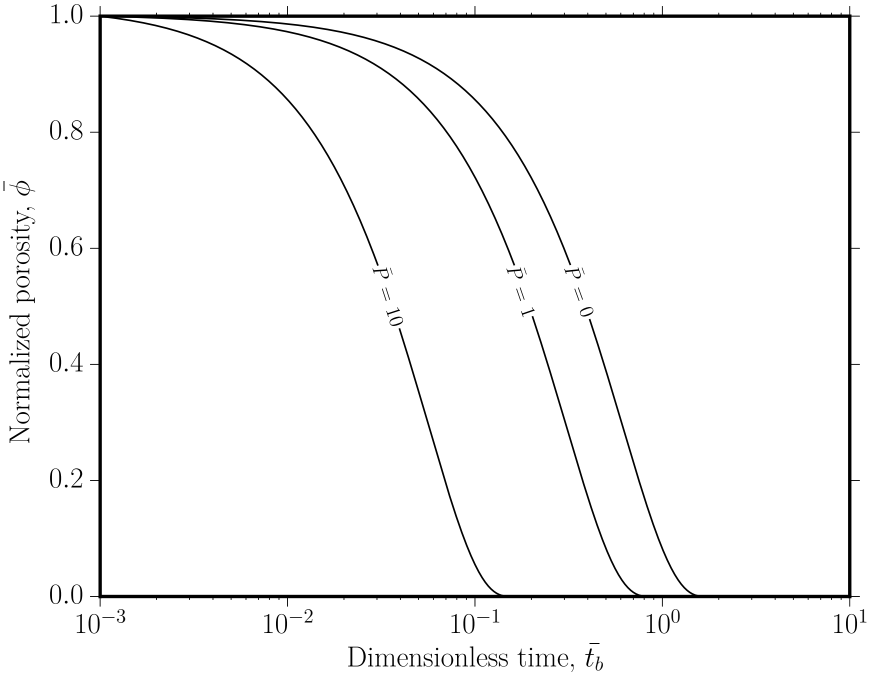

Figure 3.9: Densification of silicate droplets under pressure. Here I show how the pressure significantly decreases the sintering time. I note that this result is highly applicable to volcanic interiors.

pressure on the liquid P to the Laplace pressure P_L which will be termed $\bar{P}$

$$\frac{d\phi}{dt} = -\frac{3\Gamma}{2\mu}\left(N_b\frac{4\pi}{3}\right)^{\frac{1}{3}}\phi^{\frac{2}{3}}(1-\phi)^{\frac{1}{3}}\left(1+\psi\left(\frac{\phi}{1-\phi}\right)^{\frac{1}{3}}\right) \tag{3.44}$$

where

$$\psi = \frac{P}{2\Gamma}\left(\frac{3}{4\pi N_b}\right)^{\frac{1}{3}} \tag{3.45}$$

such that if $\psi = 0$, then we recover the case where sintering is driven only by surface tension Eq. 3.7. Now following the steps outlined in the manipulation of the vented bubble model, I can convert N_b to a_i and ϕ_i leading to

$$\frac{d\phi}{dt} = -\frac{3\Gamma}{2\mu a_i}\left(\frac{\phi_i}{1-\phi_i}\right)^{\frac{1}{3}} \phi^{\frac{2}{3}}(1-\phi)^{\frac{1}{3}}\left(1+\bar{P}\right) \tag{3.46}$$

where $\bar{P} = P/P_L$. This is non-dimensionalized as before using $\bar{\phi} = \phi/\phi_i$ and Eq. 3.24 so that

$$\frac{d\bar{\phi}}{d\bar{t}_b} = -\frac{3}{2}\left(\frac{1-\phi_i\bar{\phi}}{1-\phi_i}\right)^{\frac{1}{3}} \bar{\phi}^{\frac{2}{3}}\left(1+\bar{P}\right) \tag{3.47}$$

In Figure 3.9 I show the predictions for when $\bar{P} \gg 0$, which implies that the external pressure is greater than the pressure in the pore phase, thus the sintering is more rapid than the case where the sintering is only driven by surface tension. If $\bar{P} \ll 0$ then the system would expand rather than shrink due to pore overpressure and ϕ would increase. As mentioned, this will not be experimentally tested and is rather a hypothesis that I leave to future work to test. However, this prediction is likely to be volcanically relevant. A caveat rests on the derivation of the vented bubble model [Mackenzie & Shuttleworth, 1949] such that at elevated liquid pressures, the analogy of the sintering units as bubbles with concentric shells may no longer be sufficient, especially if deformation of the particles from spherical is to be expected [Quane & Russell, 2005, 2003].

3.3.6 The effect of crystals

Another complexity that has received less attention is the case where crystals are involved in the system. Crystals can be thought of as purely rigid bodies that are not subject to internal flow when stresses are applied. In volcanic systems, crystals can be abundant. Here I first explore two likely end-member scenarios before showing how crystal content could be incorporated into the sintering models.

If the size of a crystal is R_x, then the two end-member cases are defined as $R_x \ll R$ and $R_x \gg R$. The former case, where the crystals are smaller than the sintering glass particles (droplets at high temperature) is a case where it is reasonable to consider the crystals as suspended in the liquid. In this case, the value of μ is modified by the fraction of crystals ϕ_x, which will be dealt with here. The other case is for when the crystals are much larger than the sintering particles (droplets). In this case, the crystals are obstacles that demark clusters of sintering droplets. Here it's less clear how this might be treated and is therefore left as another consideration and I do not provide an explicit hypothesis to test.

For the former case ($R_x \ll R$), the system can be thought of as an effective medium where the droplets that are sintering are suspensions, rather than being pure liquids. To cast this quantitatively, we can decompose the suspension viscosity η into the liquid viscosity μ, which is remains dependent on temperature, composition and water content (*see* Chapter 2.3.1), and the relative viscosity contribution of the crystals η_r. Once achieved, η should replace μ in the solutions for the sintering time in Chapter 3.3.

There are many models for the η_r [Costa et al., 2007; Mueller et al., 2010; Cimarelli et al., 2011]. However, the model that is most well-validated is that of

Mueller et al. [2010] in which η_r follows a Maron-Pierce form such that

$$\eta_r = \left(1 - \frac{\phi_x}{\phi_m}\right)^{-2} \tag{3.48}$$

where ϕ_m is the maximum packing fraction of crystals and η_r is related to η by μ so that $\eta = \mu\eta_r$. The term ϕ_m is further related to the particle aspect ratio [Mueller et al., 2010; Mader et al., 2013; Truby et al., 2015]

$$\phi_m = \phi_{m*} \exp\left(-\frac{(\log_{10} r_p)^2}{2m^2}\right) \tag{3.49}$$

where ϕ_{m*} is the maximum packing fraction for crystals that are spherical, taken as a reference value, r_p is the aspect ratio and m is a dimensionless factor. In Mader et al. [2013], m is calibrated to be 1.08 or 1, depending if the particles are smooth or rough, respectively, and ϕ_{m*} is 0.656 or 0.55, also for smooth or rough particles respectively.

Now to incorporate this effect into the models for sintering, we can modify Eq. 3.47 as follows

$$\frac{d\bar{\phi}}{d\bar{t_b}} = -\frac{3}{2\eta_r}\left(\frac{1 - \phi_i\bar{\phi}}{1 - \phi_i}\right)^{\frac{1}{3}} \bar{\phi}^{\frac{2}{3}} \tag{3.50}$$

In Figure 3.10 I show the results of varying ϕ_x from zero, which represents the sintering behaviour given by the vented bubble model (Chapter 3.3), to a value close to the maximum packing fraction. I leave this as the ratio of ϕ_x/ϕ_m to avoid contouring for individual cases of particle aspect ratios. But it's clear that by increasing the suspended particle volume fraction, the sintering is retarded

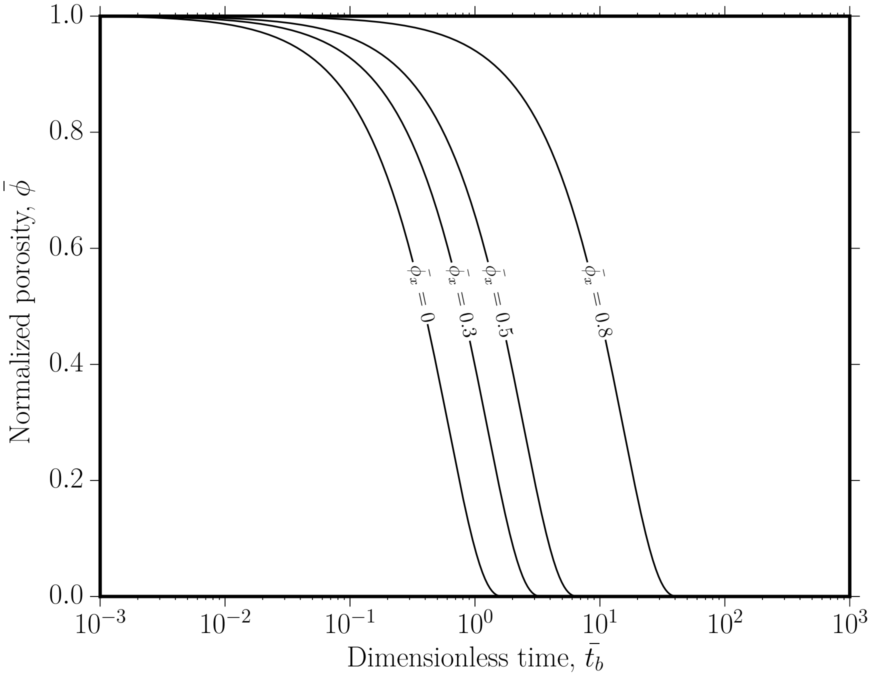

Figure 3.10: The effect of suspended crystals on sintering of viscous droplets predicted by the vented bubble model, Eq. 3.47 adapted in Eq. 3.50. Here $\bar{\phi}_x$ is ϕ_x/ϕ_m and is used to modify μ via Eq. 3.48. Suspended crystal loads retard sintering rates significantly.

relative to the zero-crystallinity case. This theoretical incorporation of crystal-content in sintering theory would need experimental validation, which is beyond the scope of this thesis. However, in the Chapter 6 I provide examples of how this might be done in the future.

3.4 Microstructural geometry in densifying heterogeneous media

The radii of initially spherical glass spheres are trivial to constrain using a variety of techniques providing constraint of the lengthscale R_i for use with the neck-formation model [Frenkel, 1945]. However, the lengthscale a_i that appears in the vented bubble model [Mackenzie & Shuttleworth, 1949] and my extensions thereof is a less easy-to-constrain parameter. However, Torquato [2013] and Torquato & Avellaneda [1991] provide a rigorous expression for a mean pore size $\langle a_i \rangle$ occurring between particles in arbitrary packing. Their scheme can be cast for a packing of completely impenetrable 'hard' spheres: an arrangement identical to the initial case of packed glass beads. This is given in the form of a cumulative probability density $F(\xi)$ of the pore size distribution for which $\xi = a/R$

$$F(\xi) = \frac{E_V(\xi)}{\phi} \tag{3.51}$$

where $E_V(\xi)$ is a pore nearest-neighbour exclusion probability function. In the granular systems described herein, this is a conceptual tool akin to finding the expected fraction of space available to a pore of radius a. To solve for $E_V(\xi)$ is a non-trivial problem that has received significant attention [Torquato & Avellaneda, 1991; Torquato, 2013]. A validated expression for $E_V(\xi)$ as a function of R is given by Torquato [2013] based on Torquato & Avellaneda [1991] and reproduced here for completeness, where we cast it in terms of the porosity ϕ

$$E_V(\xi) = \phi \exp\Big((\phi - 1)[q_0(1+\xi)^3 + 3q_1(1+\xi)^2 + 12q_2(1+\xi) + q_3]\Big) \tag{3.52}$$

Eq. 3.52 is valid for $\xi \geq 0$ and contains coefficients q_n that are given by

$$\begin{cases} q_0 = (2 - \phi + (1 - \phi)^2 - (1 - \phi)^3)/\phi^3 \\ q_1 = (1 - \phi)(3(1 - \phi)^2 + 4\phi - 7)/2\phi^3 \\ q_2 = (1 - \phi)^2(1 + \phi)/2\phi^3 \\ q_3 = -(q_0 + 3q_1 + 12q_2) \end{cases} \tag{3.53}$$

The *nth* moment of the probability density function of ξ, termed $\langle \xi^n \rangle$, is then related to the cumulative probability density function $F(\xi)$ in Eq. 3.51 by integrating as follows

$$\langle \xi^n \rangle = n \int_0^\infty \xi^{n-1} F(\xi) d\xi \tag{3.54}$$

hence the mean (*i.e.* $n = 1$) value of a is $\langle a \rangle = \langle \xi \rangle \langle R \rangle$. Eqs 3.51-3.54 can be used to find a in the monodisperse limit of R.

Torquato [2013] additionally describes a polydisperse solution from Lu & Torquato [1992] which, as with the monodisperse limit, is validated by those authors against data or simulations and so I repeat it here for completeness. In this model, the pore nearest-neighbour exclusion probability function is the polydisperse $e_V(\xi)$ instead of $E_V(\xi)$ and is

$$e_V(\xi) = \phi \exp\left(2S(\phi - 1)\left[\frac{p_0}{8}(1 + \xi)^3 + \frac{p_1}{4}(1 + \xi)^2 + \frac{p_2}{2}(1 + \xi)\right]\right) \tag{3.55}$$

for which S is the ratio of the specific surface area of the polydisperse system to that of the monodisperse system at the same ϕ. S is given by

$$S = \frac{\langle R^2 \rangle}{\langle R^3 \rangle} \langle R \rangle \tag{3.56}$$

where again, $\langle R^n \rangle$ is the *nth* moment of the distribution of R. As before, coefficients, p_n appear in $e_V(\xi)$, and are defined here

$$\begin{cases} p_0 = \left[4\phi\langle R\rangle^2 \left(\phi + 3S(1-\phi)\right)/\langle R^2\rangle + 8\left(S(1-\phi)\right)^2\right]/\phi^3 \\ p_1 = \left[6\phi\langle R\rangle^2/\langle R^2\rangle + 9S(1-\phi)\right]/\phi^2 \\ p_2 = 3/\phi \end{cases} \tag{3.57}$$

Finally, to recover the value of $\langle a \rangle$ that represents the polydispersivity of R, the same method is employed as before, via Eq. 3.51 where Eq. 3.55 is used in place of Eq. 3.52 and then Eq. 3.54 is solved numerically.

An example of polydispersivity is the Schulz distribution [Schultz, 1939]. If we introduce a polydispersivity factor m', the the Schultz expression related this to $\langle R^n \rangle$ by

$$\langle R^n \rangle = \frac{\langle R \rangle^n (m'+n)!}{m'!(m'+1)^n} \tag{3.58}$$

so that at $m = 0$ the polydisperse limit is reached where particle sizes are skewed heavily toward smaller classes and the tail to large sizes is broad. In Figure 3.11 I show how the Schulz distribution, Eq. 3.58, with the solutions given by Eqs 3.51-3.57, can be used to solve for pore sizes when particle sizes are known. This is

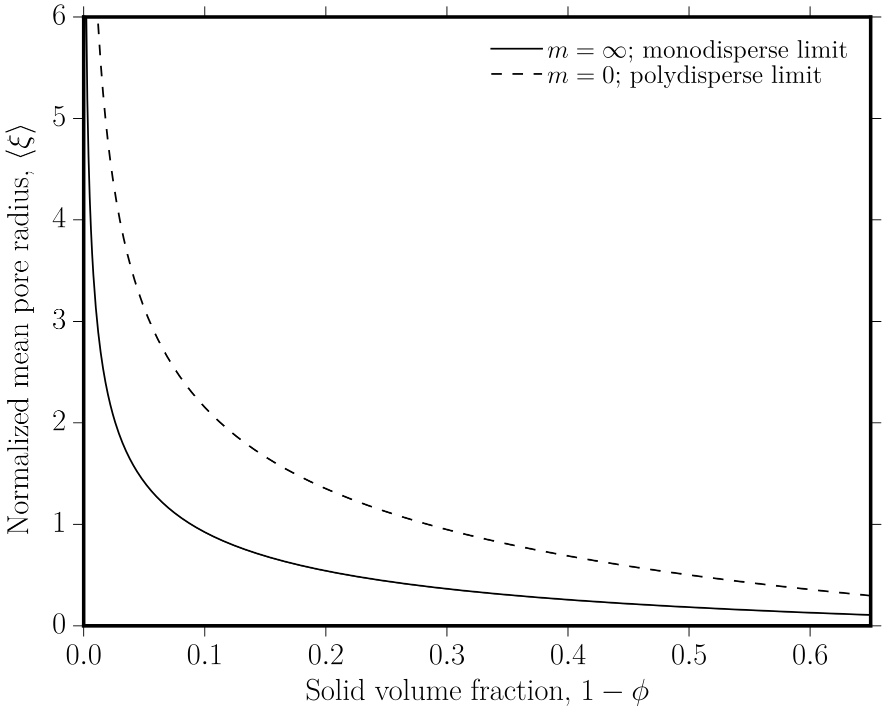

Figure 3.11: The prediction of the mean pore size $\langle a \rangle$ that can nestle between monodisperse or polydisperse particles of mean radius $\langle R \rangle$ and which are packed to a given porosity ϕ using the models presented in Torquato [2013].

critical to the theory given in Chapter 3.3 where the pore size a is a fundamental parameter controlling the rate of sintering throughout the process.

But the pressure was too great. He would have to find something to make good the equilibrium...
...For day by day he felt more and more like a bubble.

D. H. Lawrence [*from* Women in Love.]

4

Results: The densification of viscous liquids and magmas

Here I apply the theory from Chapter 3 to experimental data. Herein I use experimental data from the optical dilatometry method, which offers better spatial resolution on sample geometry than previously achieved, and so I can differentiate the efficacy of competing models for densification of viscous droplets. In this chapter I will take a step-by-step approach. In each step I will compare data, which I will render dimensionless, against models. First, I will test the densification of initially spherical and compositionally homogeneous glass beads (droplets at high temperature). This is designed to represent a calibration dataset which best represents the model geometry and so should be a true test of efficacy. Then in a second step, I will test the best model against systems which contain increasing complexity. The sample geometries I will test are

- Arrays of initially spherical droplets (using spherical glass beads as a starting geometry). In this system, the droplet composition is stable.
- Arrays of initially angular droplets (using angular glass shards as a starting material). In this system, the droplet composition is stable.
- Arrays of initially angular droplets that contain crystals and spatial distribution of liquid composition (by using natural volcanic ash).
- A porous magma (using high porosity pumice as a starting material). In this system, the liquid composition may be evolving during densification.

By testing three granular systems, followed by a highly porous system, I am testing a central hypothesis of this thesis: namely that densification models can be unified across two largely different geometries. To do this I will comment on the differences in the lengthscales involved in effect normalization of each system.

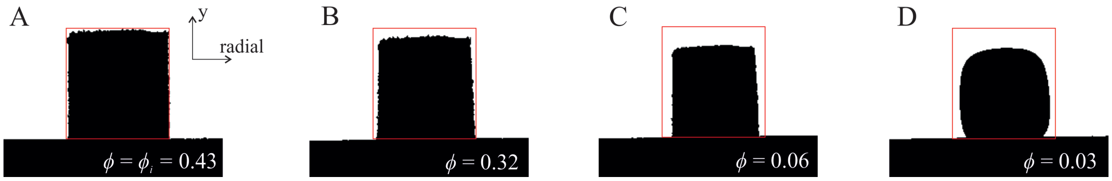

Figure 4.1: The time-dependent changes in sample volume as recorded by the camera in the optical dilatometer. Shown here are images for the densification of free-standing cylinders of glass beads. (A-D) Porosities are labelled for each cross-section. The initial diameter of each cylinder was $3\,\mathrm{mm}$.

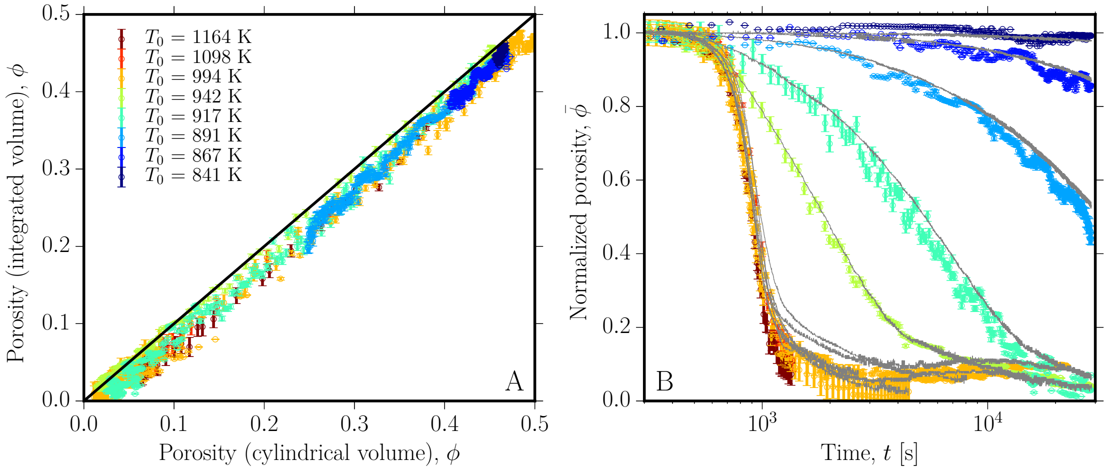

Figure 4.2: (A) Calibrating optical dilatometry volume data using the cylindrical approximation and the solid-of-rotation. Note that the cylindrical approximation consistently overestimates the volume by ∼5%. (B) The time dependent porosity during densification. Here, and throughout this chapter, the densification mechanism is by sintering under surface tension. The experimental data presented here will be the same data repeated in this section. The coloured symbols are from the solid-of-rotation volume while the grey lines are the cylindrical approximation. The latter method will not be used from here on.

I restate here that these models implicitly assume that the pore-fluid is highly permeable, such that the fluid can be evacuated from the sample as densification progresses and that outflow of the pore fluid does not hinder the densification

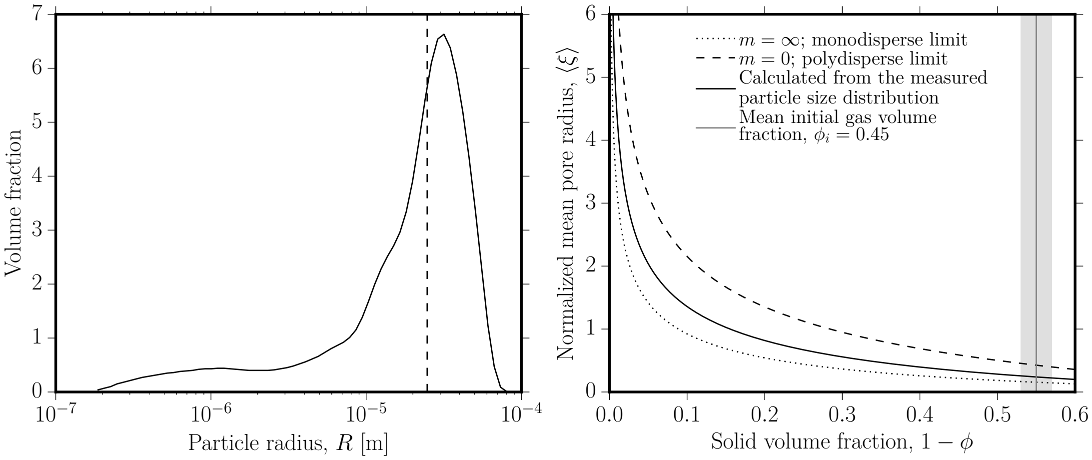

Figure 4.3: The geometry of the spherical glass beads. (A) The particle size distribution measured with the mean particle size labelled as a vertical dashed line. (B) The calculation of the mean pore radius from the polydisperse measurement of the particle sizes shown in (A). For the method used see Chapter 3.4.

at all. This is likely true for the high permeability systems here tested until the percolation threshold is approached. The implication of such a universality in densification models is that the most important difference between porous and granular materials is the porosity at which the percolation threshold is met. And it is well documented that the percolation threshold for granular materials is significantly lower than for most porous materials in the abscence of anisotropic deformation [*e.g.* Rintoul, 2000; Torquato, 2013; Klug & Cashman, 1996; Mueller et al., 2005]. The implications of this discussion are explored in Chapter 5.

4.1 SINTERING OF INITIALLY SPHERICAL VISCOUS DROPLETS UNDER SURFACE TENSION

After applying the solid of rotation to obtain time-dependent volumes of high temperature experimental samples *in situ* in voxels by the optical dilatometry method (*see* Figure 4.1 for the evolution of raw binary images), and subsequently converting these to $\phi(t)$ (*see* Chapter 2), I obtain the data presented in Figure 4.2. The curves all show a rapid onset of ϕ decay followed by a long tail at high values of t. While the shape of the curves is similar across all isothermal temperature, termed T_0, the absolute rate of this process is systematically dependent on T_0. I use these experimental results to test the theoretical models presented in Chapter 3. In all cases, the models are tested in dimensionless form, which necessitates transforming the raw datasets – *i.e.* $\phi(t)$ for each experimental run – into $\bar{\phi}(\bar{t_n})$, $\bar{\phi}(\bar{t_b})$ or $\bar{\phi}(\bar{t_b^*})$ depending on the model to be tested. Porosity is trivially normalized as $\bar{\phi} = \phi/\phi_i$ or $\bar{\phi}^* = (\phi - \phi_f)/(\phi_i - \phi_f)$. Where non-isothermal behaviour can be ignored, Eq. 3.23 & 3.24 are used to non-dimensionalize t as $\bar{t_n}$ or $\bar{t_b}$, respectively. In either case, viscosity is calculated after Chapter 2.3.1 and surface tension is constant at 0.3 $\mathrm{N\,m^{-1}}$ for the glass beads that are used as calibration data set herein. If Eq. 3.23 is used, the initial droplet radius R_i is either taken from the measured particle size distribution (Figure 4.3), or treated as a fitting parameter. If Eq. 3.24 is used, the initial pore radius a_i is either calculated from R_i following the approach outlined in Chapter 3, or treated as a fitting parameter.

Where non-isothermal behaviour is important, non-dimensionalizing t is slightly

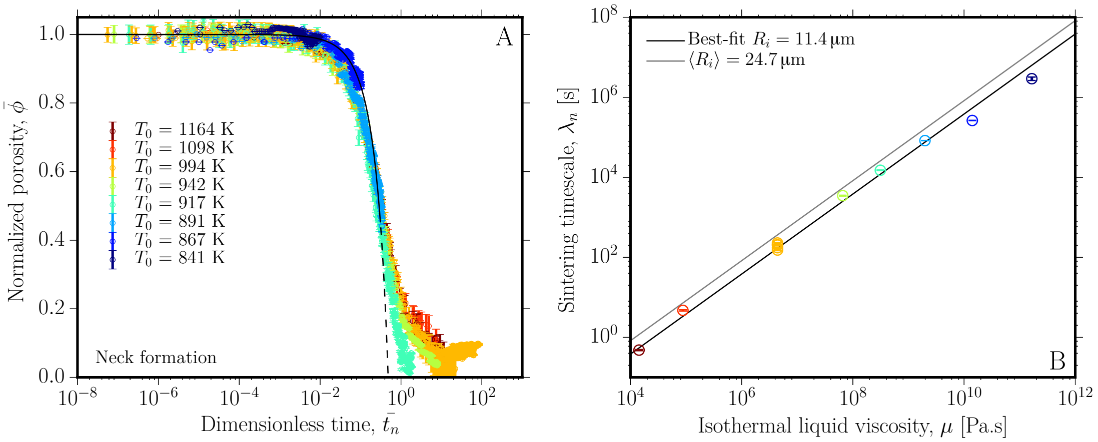

Figure 4.4: Experimental data for glass beads normalised by λ_n and compared with the neck-formation model proposed by Frenkel [1945] and adapted herein. (A) The comparison of the time-dependent porosities. (B) The best-fit lengthscale in λ_n across all experimental temperatures compared with the measured mean particle size $\langle R \rangle$.

more complex. The temperature-time data for the run is used to calculate $\bar{t_n}$ or $\bar{t_b}$ via Eq. 3.26 or 3.27, as required. As before, μ is calculated from the relationship given in Chapter 3, and surface tension is constant. If Eq. 3.26 is used, the initial droplet radius R_i is either taken from the measured particle size distribution, or treated as a fitting parameter. If Eq. 3.27 is used, the initial pore radius a_i is either calculated from R_i following the approach outlined in Chapter 3, or treated as a fitting parameter.

In Chapters 4.1.1-4.1.2, I allow the initial droplet radius R_i and initial pore radius a_i to vary freely, as fitting parameters; in Chapter 4.1.3 I constrain these radii based on measured particle size distributions (Figure 4.3). This two-step analysis allows me to assess the consistency of each model across the large range of liquid viscosities investigated before generalising the models without any fitting

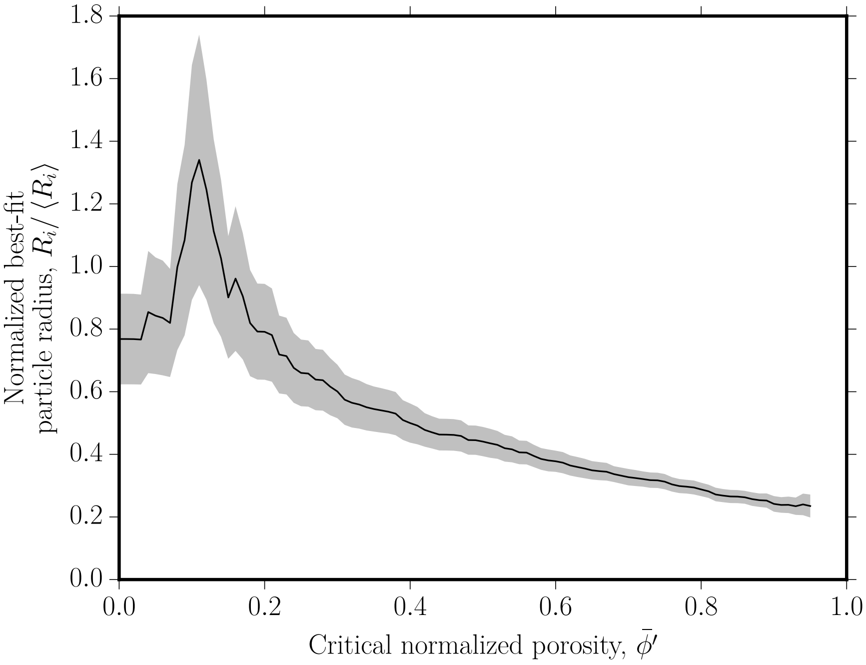

Figure 4.5: Testing the validity of the neck-formation model as different portions of the process are included in the fit proceedure.

procedure. First I will test the neck formation model [Frenkel, 1945], for which the characteristic lengthscale associated with sintering is R, before moving onto the family of models for which this lengthscale is rather a.

4.1.1 Testing the neck-formation model

For each dataset, the best fit of the neck formation model (Eq. 3.31) is found with R_i as a free fitting parameter using a least squares regression procedure. When the experimental time t is normalised using the best-fit value of R_i obtained, the data collapse to close to a single curve. Compared with the model itself (Eq. 3.31), this produces a moderate fit for all temperatures (Figure 4.4). Using Eq. 3.23 and

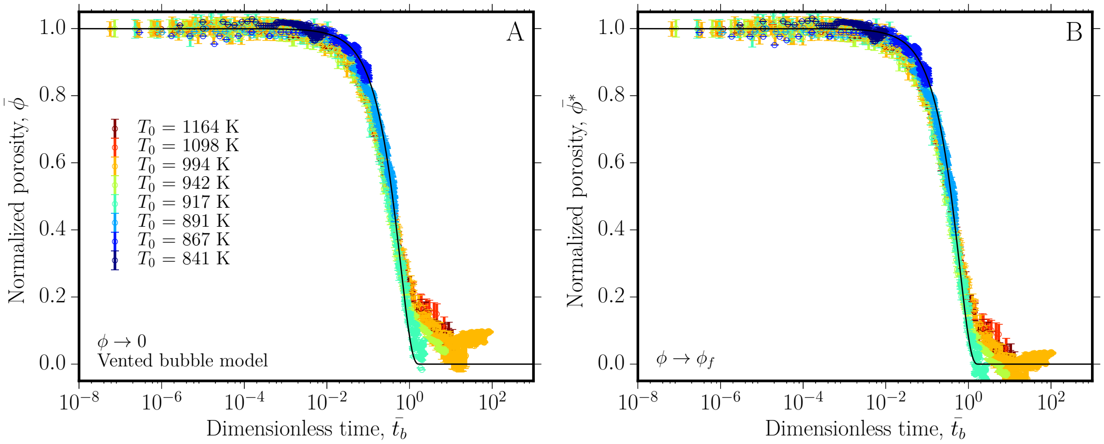

Figure 4.6: Experimental data for glass beads normalized using λ_b and compared with the vented bubble model proposed by Mackenzie & Shuttleworth [1949] and adapted herein. (A) The case when I let $\bar{\phi}$ decay to 0; (B) The case when I let $\bar{\phi}$ go to the observed ϕ_f.

the definitions of the isothermal viscosity μ and the surface tension Γ discussed, a linear regression in Figure 4.4 relates to the best-fit radius R_i and for all values of μ yields an estimated average $R_i = 11.4\pm1.2\,\mu\text{m}$. This compares favourably with the mean radius from the measured particle size distribution of $\langle R \rangle = 24.7\,\mu\text{m}$ and a coefficient of determination of 0.984. The model of Frenkel [1945] tested here is based on the formation of necks between liquid droplets and as-such is expected to describe the early part of the sintering process better than the later part. This is confirmed by Figure 4.4, in which the model curve decays to $\bar{\phi} = 0$ prior to the observed tail of the process. Therefore, if this model has validity, it is likely only for the initial part of the sintering process, when mass transport of liquid is dominantly in necks between particles.

In order to explore this further, I repeat the fitting process multiple times for

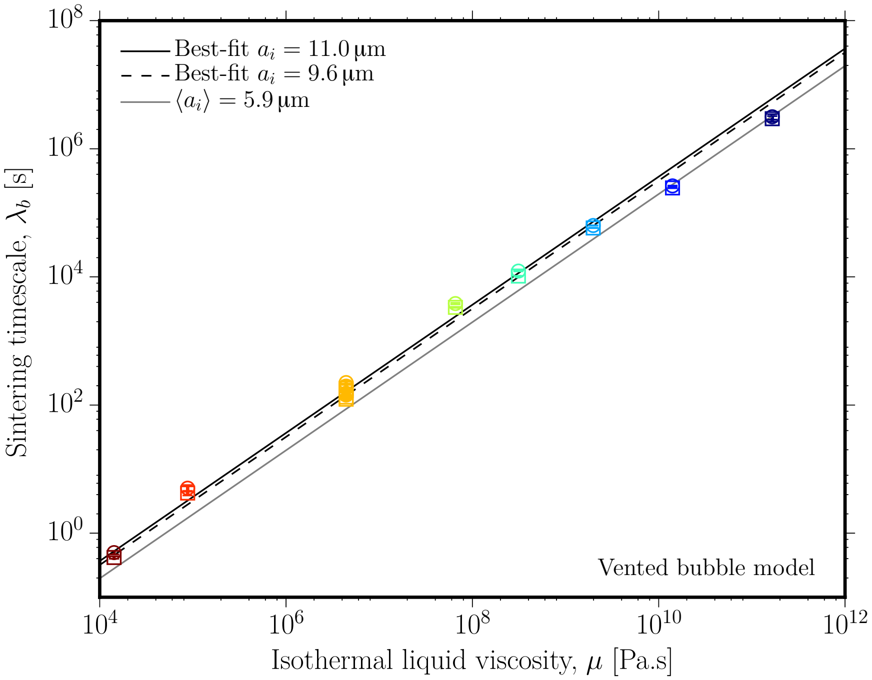

Figure 4.7: The best-fit lengthscale a_i in λ_b across all experimental temperatures compared with the measured mean bubble size $\langle a_i \rangle$ computed in Chapter 3.4 and shown in Figure 4.3 tested using the vented bubble model.

all datasets, each time fitting a slightly greater fraction of the data. In each case, I start the fit at $\bar{\phi} = 1$ (i.e at $t = 0$) and fit to a porosity $\bar{\phi}'$, deriving a best fit value for R_i for that fraction of the data. Figure 4.5 plots R_i against $\bar{\phi}'$, with R_i normalized by $\langle R \rangle$, such that a value of $R_i / \langle R \rangle$ closer to 1 indicates a good fit between computed and measured particle radius. The plot demonstrates that the model and data are in closest agreement when we fit only the early sintering data, and that the fit worsens as more data are included in the fit. The data presented in Figure 4.4 were calculated using $\bar{\phi}' = 0.44$, which, for our ϕ_i, corresponds to $\phi = 0.2$, which is the value above which Prado et al. [2001] claim the Frenkel

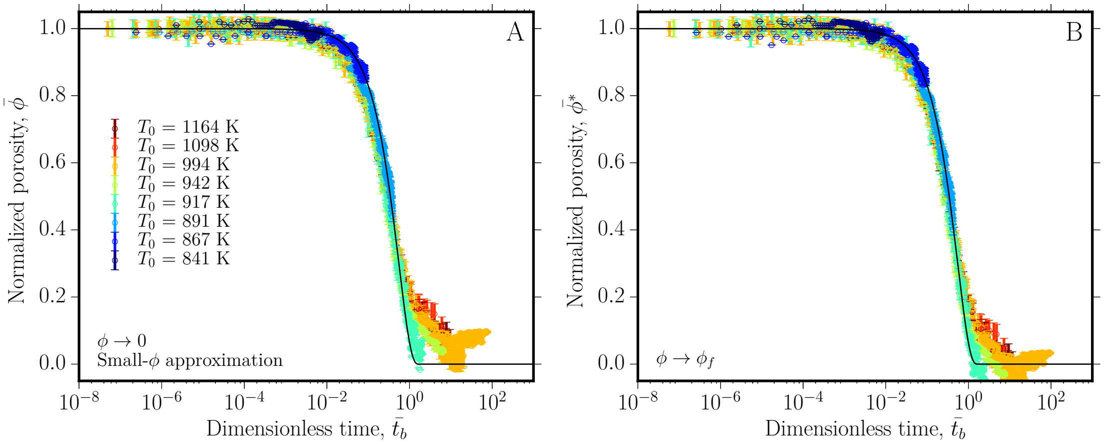

Figure 4.8: Experimental data for glass beads normalized using λ_b and compared with the small-ϕ approximation of the vented bubble model proposed herein. (A) The case when I let $\bar{\phi}$ decay to 0; (B) The case when I let $\bar{\phi}$ go to the observed ϕ_f.

model is applicable. However, here $\bar{\phi}' = 0.44$ is intended to be illustrative rather than diagnostic of the efficacy of this model.

4.1.2 TESTING THE VENTED BUBBLE MODEL

Next, I test the vented bubble model, which was modified after Mackenzie & Shuttleworth [1949] in Chapter 3. This model uses the dimensionless time $\bar{t}_b$ in which time t is normalised to the bubble capillary timescale λ_b. The model, which is solved numerically, can either go to $\bar{\phi} = 0$ (Eq. 3.47) or to $\bar{\phi} = \phi_f$ (Eq. 3.41; Figure 4.6). In the former case the best-fit timescale λ_b for all experiments yields a best-fit bubble radius a_i of 11.0±1.2 µm and in the latter case a best-fit a_i of 9.6±0.9 µm, both of which compare favourably with the $\langle a \rangle$ value of 5.9 µm computed following the approach described in Chapter 3.4 (Figure 4.7).

Additionally the agreement across all experiments is excellent, with a coefficient

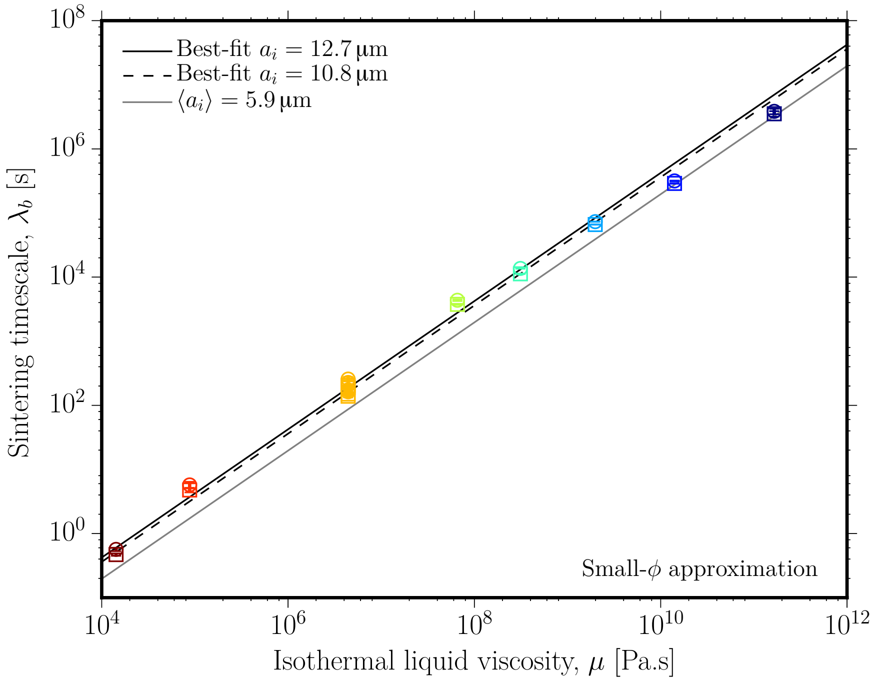

Figure 4.9: The best-fit lengthscale a_i in λ_b across all experimental temperatures compared with the measured mean bubble size $\langle a_i \rangle$ computed in Chapter 3.4 and shown in Figure 4.3 tested using the small-ϕ approximation.

of determination of 0.993 (Figure 4.7) which is manifest in the success of the collapse to a single curve of $\bar{\phi}$ with $\bar{t_b}$ (Figure 4.6). The final gas volume fraction ϕ_f refers to the minimum observed value that is confirmed by X-ray micro computed tomography and is measured to be ∼0.03.

The Mackenzie & Shuttleworth [1949] model yields an analytical approximation when $\phi \ll 1$ by Eq. 3.36. I test this against the experimental data in Figure 4.8. Whether $\bar{\phi}$ goes to zero or to the empirically observed ϕ_f, the best-fit a_i is within error of the estimated $\langle a_i \rangle$ for all experimental values of μ (Figure 4.9). For our samples, for which the average $\phi_i = 0.45 \pm 0.02$, the small-ϕ approximation

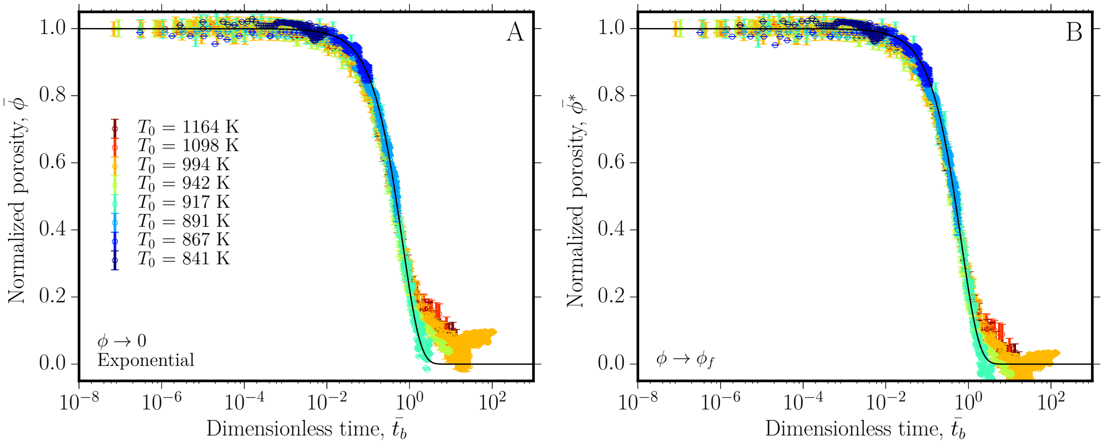

Figure 4.10: Experimental data for glass beads normalized using λ_b and compared with the exponential approximation of the vented bubble model proposed herein. (A) The case when I let $\bar{\phi}$ decay to 0; (B) The case when I let $\bar{\phi}$ go to the observed ϕ_f.

provides an excellent collapse of the data to a single curve, and the agreement across all T_0 yields a coefficient of determination of 0.994 (Figure 4.8).

Finally, I test the commonly used [Prado et al., 2001, 2003a,b; Soares et al., 2012; Eberstein et al., 2009; Lara et al., 2004; Vasseur et al., 2013] exponential approximation of the vented bubble model (Eq. 3.38) in Figure 4.10, where I note the implicit assumption that bubble radius is independent of time. Despite this assumption, which must, in reality, be violated, the results of fitting for the timescale λ_b for both the $\phi \to 0$ and $\phi \to \phi_f$ conditions are very close to each other (Figure 4.11) and almost indistinguishable from those of the small-ϕ approximation, resulting in average best-fit radii in excellent agreement with $\langle a_i \rangle$ and a coefficient of determination of 0.995.

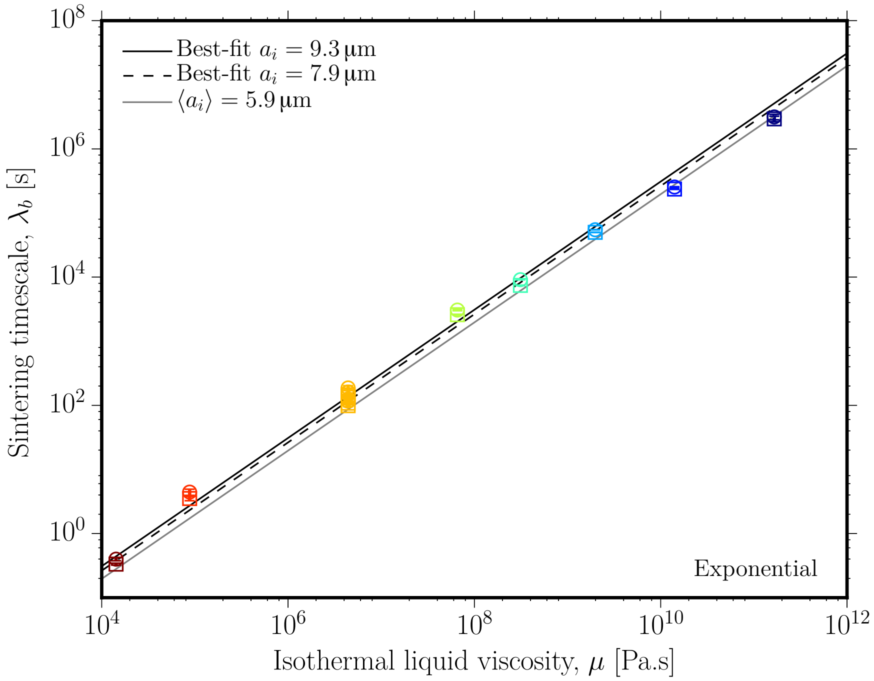

Figure 4.11: The best-fit lengthscale a_i in λ_b across all experimental temperatures compared with the measured mean bubble size $\langle a_i \rangle$ computed in Chapter 3.4 and shown in Figure 4.3 tested using the exponential approimation.

4.1.3 THE VENTED BUBBLE MODEL WITHOUT FITTING

In Figure 4.12 I show all data from Figure 4.2 normalized by the capillary timescale λ_b in which the lengthscale is the radius of the bubbles interstitial to the mean of the particles $\langle a_i \rangle$ estimated as shown in Figure 4.3, which I have shown provides a reasonable approximation to the lengthscale controlling the best-fit timescales across all experiments (Figure 4.7). This permits all data to be collapsed to a single description of $\bar{\phi}$ as a function of dimensionless time $\bar{t_b}$ without any fitting parameters. Furthermore it permits me to directly compare the three models that are based on interfacial tension around bubbles interstitial to the particles:

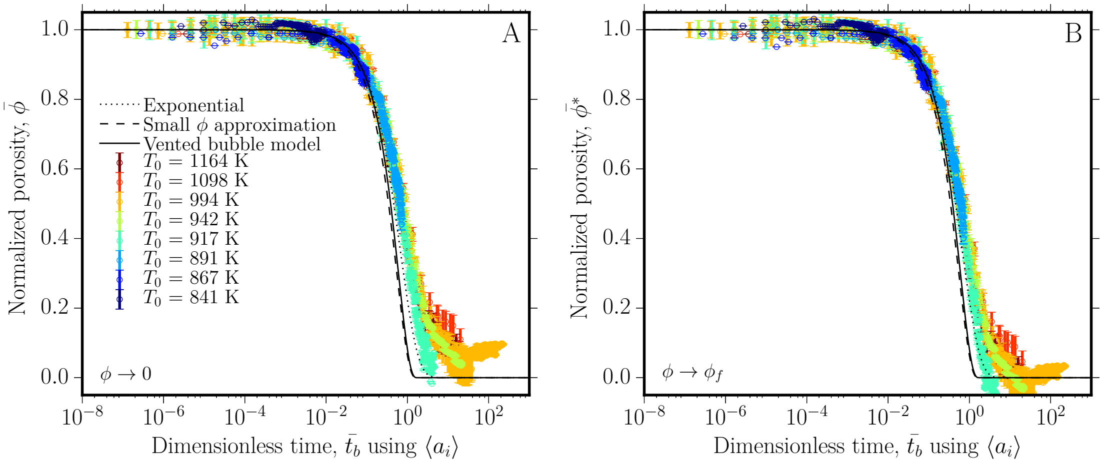

Figure 4.12: Experimental data for glass beads normalized using λ_b and compared with the (i) the vented bubble model; (ii) the small-ϕ approximation; and (iii) the exponential approximation. (A) The case when I let $\bar{\phi}$ decay to 0; (B) The case when I let $\bar{\phi}$ go to the observed ϕ_f.

(i) the vented bubble model modified from Mackenzie & Shuttleworth [1949]; (ii) the small-ϕ approximation of the vented bubble model; and (iii) the exponential approximation. I show both the solutions when $\bar{\phi} \rightarrow 0$ at $\bar{t_b} \rightarrow \infty$ and when $\bar{\phi} \rightarrow \phi_f$ at $\bar{t_b} \rightarrow \infty$ (Figure 4.12). The vented bubble model modified from Mackenzie & Shuttleworth [1949] and the small-ϕ approximation thereof are almost indistinguishable from one another for the values of ϕ_i represented by our samples, and both provide a good agreement with the data. However, we note that there is a systematic deviation from the predicted behaviour at values of $\bar{t_b}$ approaching unity. This phenomenon is discussed in Chapter 5. Nevertheless, the vented bubble model well captures the data across a huge range of experimental temperatures and thus, material viscosities. The agreement between the exponential approximation and data is slightly closer than for the vented bubble models, particularly as $\bar{t_b}$ approaches unity.

4.1.4 4D experiments at the TOMCAT beamline

The mismatch between the experimental data for glass beads and the vented bubble model (Figure 4.12) requires explanation. There are a few candidate causes to test:

- The value of $\langle a_i \rangle$ reported in Figure 4.3 is not a good description and, in fact, a_i is smaller, which would be consistent with a best-fit value shown in Figure 4.6.
- The system permeability is decaying with ϕ to a value where outgassing of the sample inhibits sintering and slows the rate of densification relative to the predictions of the vented bubble model.
- Some of the porosity is isolating as $\phi \to \phi_f$ such that $\bar{\phi}$ is overestimated.

These hypotheses can be tested by using *in situ* experiments described briefly in Chapter 2.

Herein I use only the vented bubble model and the exponential approximation thereof and neglect the neck-formation model. This is justified as the neck-formation model did not provide a superior fit to the data, while the vented bubble model, and variations thereof did. Using the same procedure of normalization of t by λ_b to yield $\bar{t_b}$, I present the collapsed data over 5 temperatures using $\langle a_i \rangle$ reported in Figure 4.3. As in Figure 4.6, the collapse is excellent. Moreover, the agreement between the vented bubble model and the data is out-competed by the

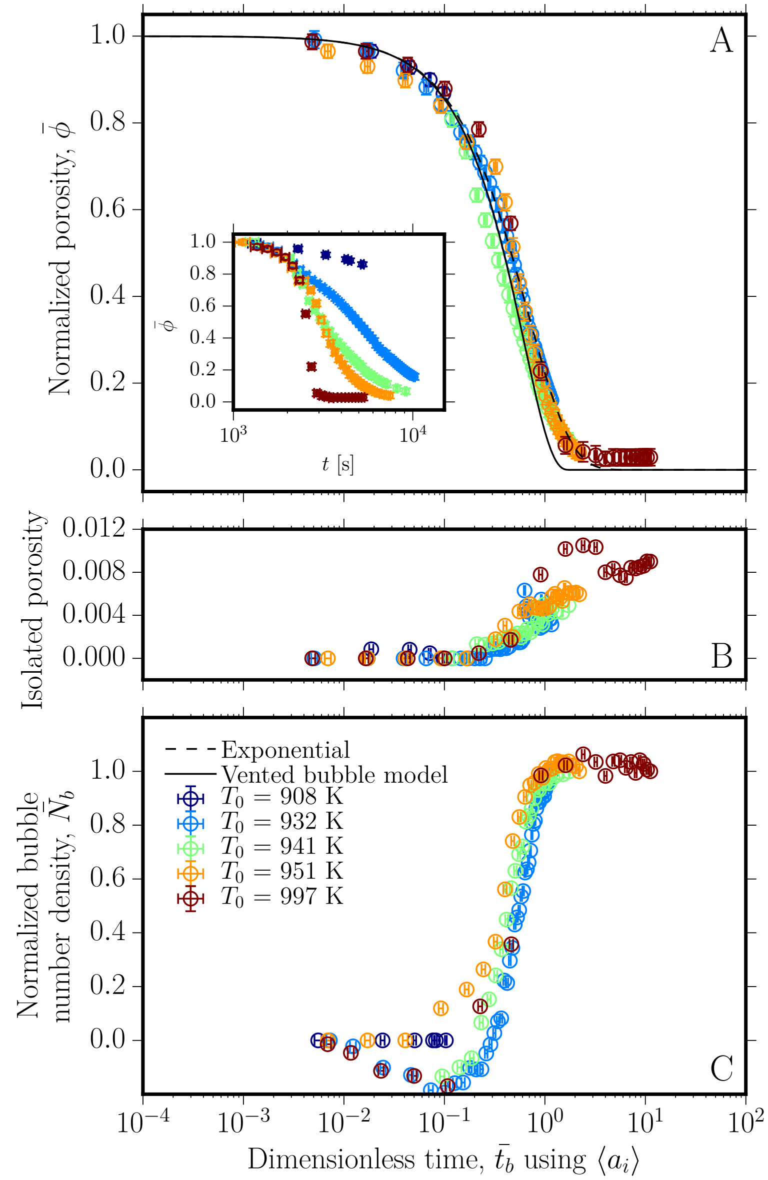

Figure 4.13: The results of densification of glass beads performed *in situ* at the TOMCAT beamline at the Swiss Light Source heated by a customized laser-heating system [Fife et al., 2012]. Here I show the evolution of (A) $\bar{\phi}$ (*inset:* the dimensional result prior to normalization); (B) the isolated porosity; and (C) the normalized pore cluster number density (or the equivalent bubble number density) $\bar{N}_b$.

exponential approximation. However, the cause of this mismatch, despite the invalid assumptions on which the exponential solution is founded, can be tested by the additional information I have from the computed tomographic reconstructions yielded by 4D experiments.

First, the isolated porosity increases from zero toward ϕ_f as $\bar{t_b} \rightarrow \infty$. This tells me that in fact, the porosity recorded during bulk volume changes is not all connected. Some clusters of pores become isolated at discrete times until ϕ_f when all porosity is isolated and thus volume equilibrium is achieved. This is further confirmed by the non-linear increase in the cluster number density (or pore number density) normalized by the initial value $\bar{N_b}$ (Figure 4.13). These results are the first of their kind and provide the explanation for why there has been a bias in published literature toward an exponential description of sintering [e.g. Prado et al., 2001, 2003a; Soares et al., 2012] without acknowledgment of its faulty underpinning. The onset of the deviation of the data from the vented bubble model indeed occurs at the onset of a non-zero isolated porosity.

If I use the above observations to recast $\bar{\phi}(\bar{t_b})$ as $\bar{\Phi}(\bar{t_b})$, which is now shown in Figure 4.14, we see that the hypothesis that pore-isolation is the cause of any discrepancy between observed and predicted ϕ is indeed correct. This new dataset permits the unequivocal validation of the vented bubble model and implicated pore-isolation as a continuous, rather than a discrete [Rintoul, 2000] event as $\phi \rightarrow \phi_f$. Future work might explore this in terms of the concept of a second-order phase transition.

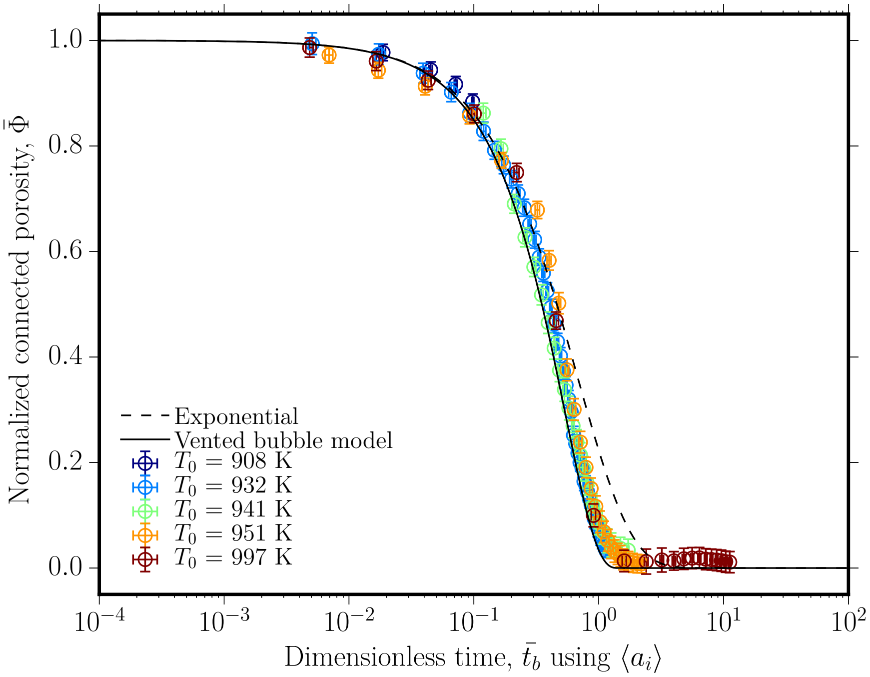

Figure 4.14: Validation that the vented bubble model is an effective description of sintering of viscous droplets when pore-isolation is considered and bulk techniques for determining ϕ are supplemented with *in situ* 4D observations.

4.2 Extension to initially angular particles

If the particles used for these sintering densification experiments are angular, as opposed to spherical in the case of the glass beads, then the dynamics must be different. However, the question of relevance to magma-densification is whether or not this difference is a first-order effect or not within the range of angularities that are exhibited by volcanic ash. The DGG- and NIST-glasses used herein, which are angular fragments when crushed to powders, have angularities that are captured by sphericity values much less than 1 (Figure 2.1). These are therefore good shape analogues for a mid-range angularity of volcanic ash.

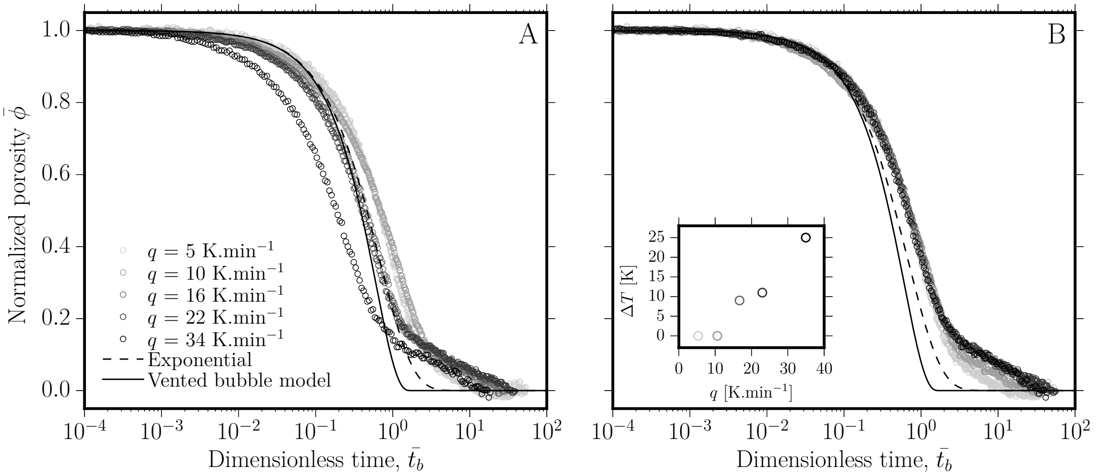

Figure 4.15: The results of sintering initially angular droplets (from angular glass shards of DGG glass; *see* Chapter 2). These data are all non-isothermal and q was constant such that T was a linear function of t. (A) The normalized data using $\langle a_i \rangle$ reported in Figure 4.3. (B) The data from (A) but for which T has been shifted after the thermal model presented in Chapter 3 to correct for thermal equilibrium arising from the high q used. *Inset:* The shift-value in T, labelled ΔT, for each q, showing the expected result that high heating rates induce a larger thermal gradient in the sample than low heating rates.

In Figure 4.15 I show the results of sintering a DGG-glass powder at $5 < q < 34\mathrm{K\,min^{-1}}$. At low heating rates ($q = 5\ \mathrm{K\,min^{-1}}$), I show that the normalized densification follows a similar evolution as the glass beads (Figure 4.12), albeit retarded moderately. The moderately slower sintering at high $\bar{t_b}$ must be due to the angularity of these particles. Another effect highlighted here is that at high q, thermal disequilibrium can be induced in these samples. When this is corrected for using the heat transfer models posed in Chapters 3 based on the scaling of D_T with ϕ presented in Chapter 2, the data again collapse to a single description. Here it is again highlighted that, while the glass bead data matched the exponential approximation, these angular particles do not at high $\bar{t_b}$. Therefore, while the

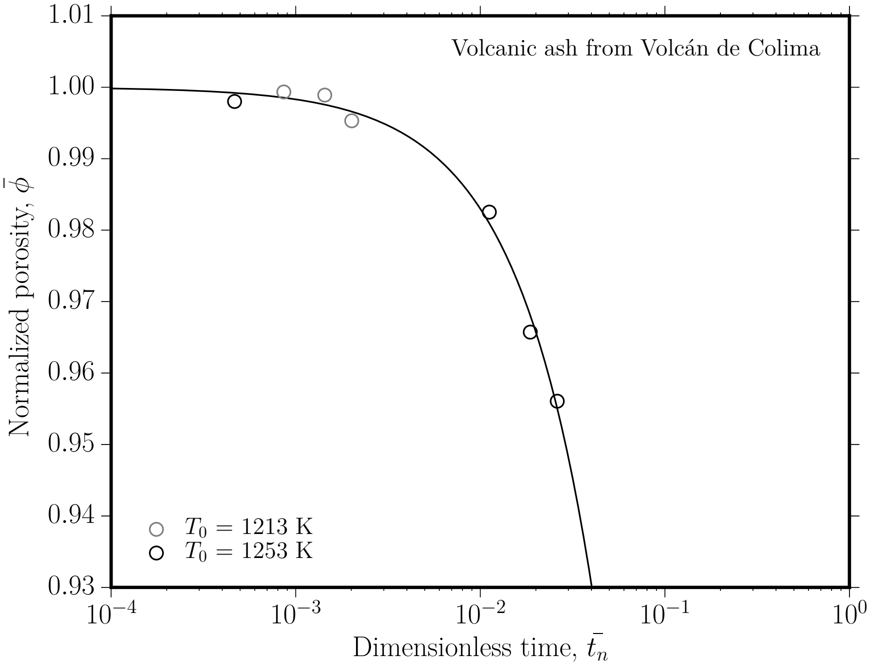

Figure 4.16: Experimental data using volcanic ash from Volcán de Colima, Mexico. This material is an extension of the analysis using angular particles in that the magma contains crystals and minor spatial distributions of composition on the particle lengthscale R. These data are compared with Eq. 3.31, the neck-formation model of Frenkel [1945].

vented bubble model captures the order-of-magnitude of sintering of droplets with natural shapes, in detail it under predicts the total time required for densification. As before, I highlight how this effect is not stated in published work on sintering [Prado et al., 2001, 2003a; Vasseur et al., 2013; Soares et al., 2012; Lara et al., 2004; Eberstein et al., 2009].

4.3 A VOLCANIC EXAMPLE OF THE NECK-FORMATION MODEL

As a specific volcanic example, I additionally show results in which the neck-formation model is tentatively applied to sintering of natural volcanic ash from Volcán de Colima, Mexico (Figure 4.16). Here the particles are partially crystalline. The high crystallinity ($\phi_x \approx 0.61$) retards the sintering process such that these data were collected over hours to hundreds of hours. The first implication is that the non-isothermal heating portion of the sample is negligible compared with the long isothermal segments applied. In this case there is a more striking difference in the form of the neck-formation model as compared with the vented bubble model; so as a first observation, these data do not have the correct kinetics to be eligible for analysis with vented bubble model. The next observation is that the temperature dependence disappears upon normalization. In this normalization, the crystal content correction is used via Eq. 3.48 using measured crystal volume fractions ϕ_x. These measured values of ϕ_x were converted to $\bar{\phi_x}$ by estimating r_p from 2D images as being 2 (Figure 2.1) before using Eq. 3.49 to convert these to ϕ_m. I recover $\phi_m \approx 0.62$, showing that $\bar{\phi_x}$ is close to 1 for these samples.

The agreement between these data and the neck-formation model is striking. However, as we saw in the analysis using the glass bead calibration data compared with the neck formation model, there tends to be good agreement at low values of $\bar{t_n}$. Were this data set continued to lower $\bar{\phi}$, it may prove less convincing. Certainly, future work is needed to constrain the sintering process for highly crystalline materials. Details, such as microstructural work, are not shown as this

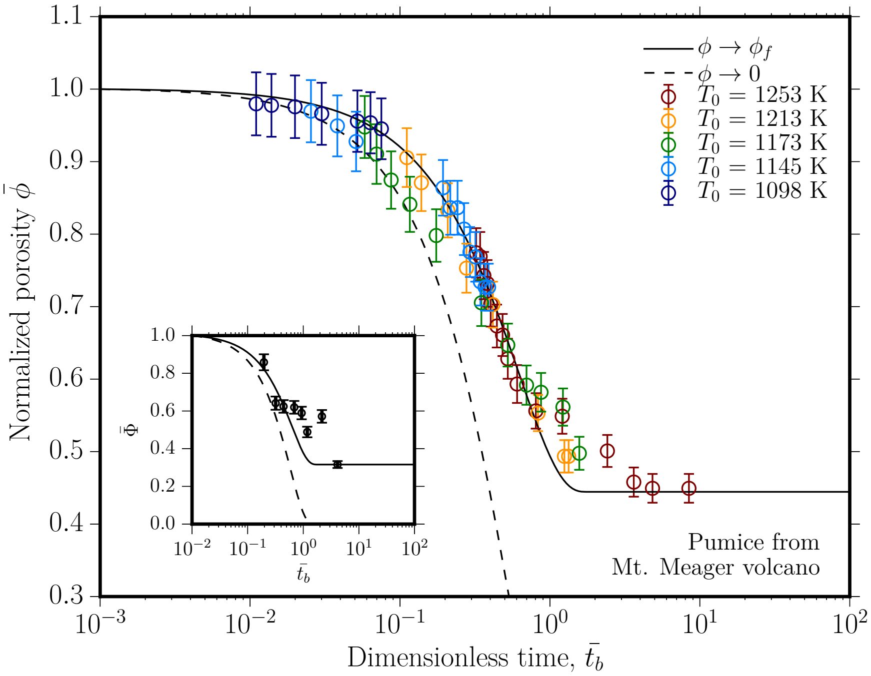

Figure 4.17: The densification kinetics in pumiceous magmas using data from Kennedy et al. [2016] here normalized as $\bar{\phi}$ and $\bar{t_b}$. As with granular viscous media, the collapse across a large range of T is excellent. A primary difference here is that the empirically observed ϕ_f is much higher than for granular samples. *Inset* the evolution of connected porosity Φ as a function of $\bar{t_b}$ for these same samples where these data are measured *ex situ* using helium pycnometry.

is not a core dataset of this thesis.

4.4 DENSIFICATION OF PUMICE UNDER SURFACE TENSION: BEYOND THE GRANULAR MODEL

While there is huge potential for the application of a granular model to many problems of volcanic relevance [Castro et al., 2012; Tuffen et al., 2003], it would be a useful extension of this work to show that the same physical concepts can be used to predict collapse of pumice. Indeed, the first densification experiments in volcanology were performed on pumice in an effort to produce dense obsidian [Westrich & Eichelberger, 1994].

The derivation of the vented bubble model is such that the densification is controlled by a bubble that shrinks under surface tension. I have shown that by approximating the space between particles in an initially granular medium as small spherical pores, this model approach works with excellent effect when the particles are both spherical (Chapter 4.1.2) and angular (Chapter 4.2). But this model is even more relevant to a pore network that is a convolute collection of partially coalesced bubbles, such as in pumice. In this way, no approximation is necessary, and the application is direct. There are two primary differences between this pumice case and the granular case.

The first is that while with granular media, ϕ_i may only be as high as the maximum packing porosity ϕ_m, which is typically $\phi_m \approx 0.4$, pumices can commonly have up to $\phi_i \approx 0.8$. At this end member, some authors have thought that this means that pumices are analagous to foams [Westrich & Eichelberger, 1994], however, they are also inherently permeable, where foams are not. This is a critical distinction to make when considering the dynamics that may dominate in the densification of the pumice, as compared with expectations for a foam. Whereas foams contain closed cells of gas in a liquid framework continuum that can drain through plateau borders [Koehler et al., 2000], pumices contain open cells of gas that are permeable, or ”vented”, and are more likely to collapse in a manner predicted by the vented bubble model [Kennedy et al., 2016].

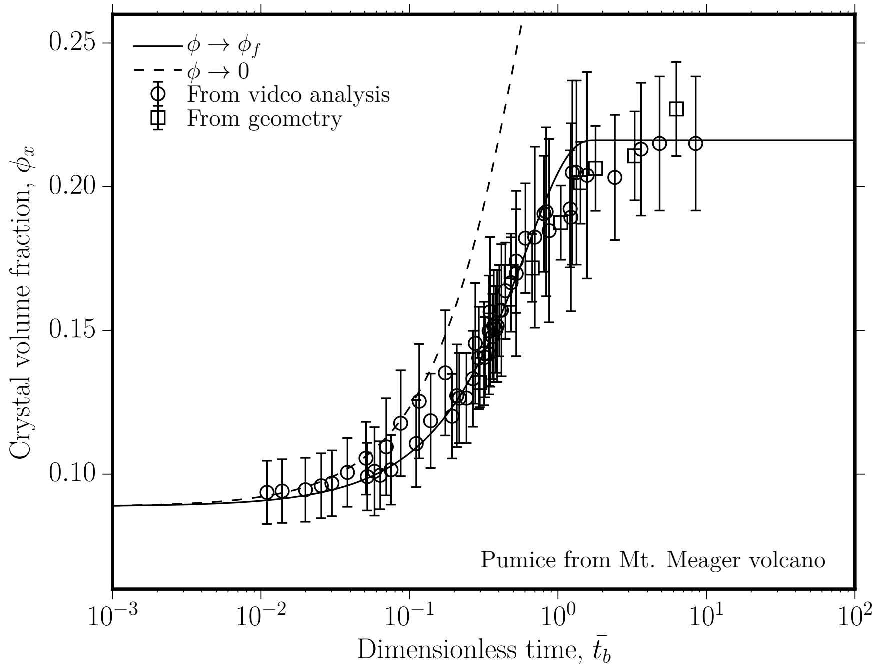

Figure 4.18: The relative enrichment of crystal phases during densification of pumice. Explicit here is the assumption that ϕ_x is not a function of t such that the apparent increase in ϕ_x arises from the decrease in ϕ only. The match to the vented bubble model with ϕ_f is good.

The second difference is that while the systems constrained thus far have been crystal poor or, in the case of the Volcán de Colima material, the experimental t was short compared with either λ_n or λ_b, in these pumices I will show that the measured equilibrium ϕ_f is much larger than for granular media. Moreover, while ϕ_f can be large (∼0.3-0.7) for a non-granular materials [Mueller et al., 2005; Blower, 2001], the prediction is still always that the connected porosity Φ falls to zero as $\phi \to \phi_f$. In the case of pumice samples in which there are often large phenocrysts, Φ does not fall to zero.

To test this, I re-analyze data from Kennedy et al. [2016] in which pumice samples from Mt. Meager volcano, Canada, are heated. In a similar way to the data in Figure 4.1.2, there is an equilibrium ϕ_f (Figure 4.17). The vented bubble model adapted for the case $\phi \rightarrow \phi_f$ provides good agreement using a bubble radius predicted.

To explain why the connected porosity does not fall to zero, I also show the evolution of ϕ_x with $\bar{t_b}$. This is computed knowing an initial ϕ_x constrained via X-ray computed tomography and propagating this value knowing that the change in volume is wholly due to a change in porosity. Using the same λ_b as in Figure 4.17, the data are fit with agreement by the vented bubble model when $\phi \rightarrow \phi_f$. The relative increase in crystal content toward some critical value at which a crystal framework is established may be the cause of the cessation of further densification prior to $\phi \rightarrow 0$ and the preservation of Φ.

Further work would be required to establish this hypothesis. However, what is certainly clear is that a far more effective method of forming a low porosity material is by densification of the granular geometry and not the porous geometry, which is in agreement with the conclusions from diffusion timescales in obsidian by Castro et al. [2012].

4.5 Microstructural evolution during densification

When interpreting the goodness of agreement between a model and experimental data, it is critical to test this against an independent prediction of the model if possible. Here, an easy qualitative observation is that the microstructure evolves from dominantly connected pores to isolated pores and from large to small pores,

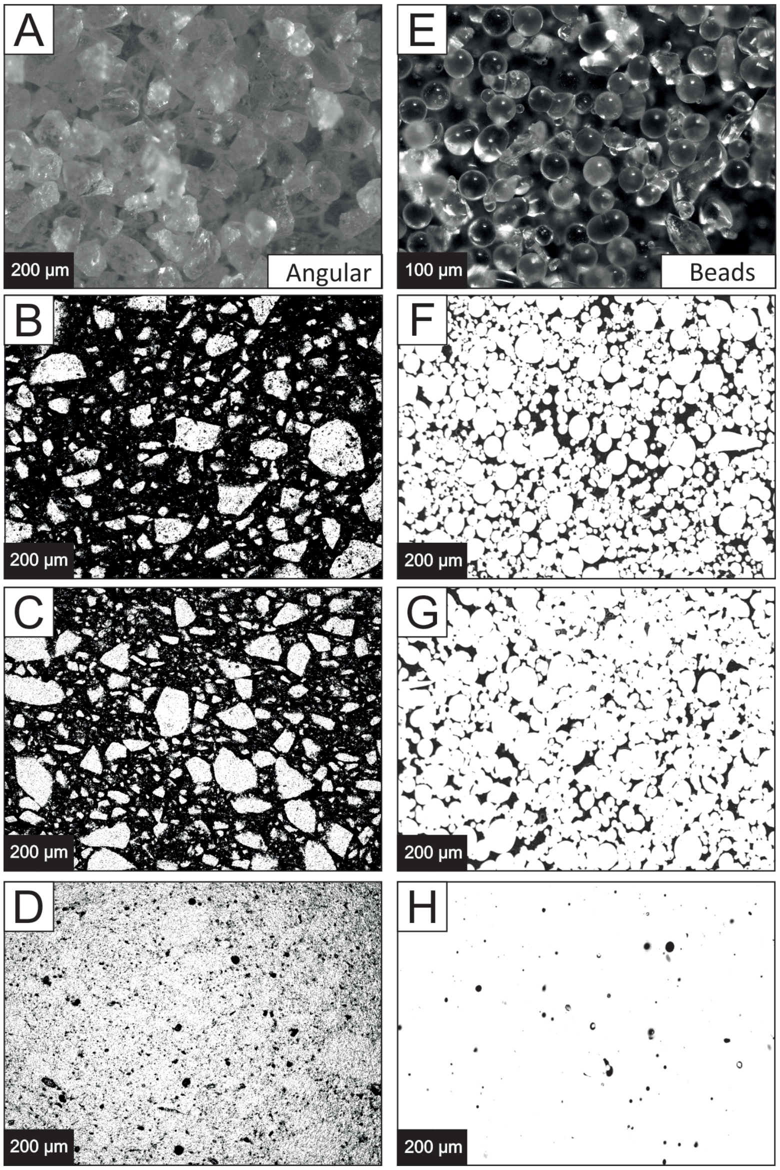

Figure 4.19: The evolution of the internal texture during isotropic densification under surface tension imaged using scanning electron microscopy. (A-D) The evolution of microstructure during densification of initially angular glass particles (Chapter 4.2). (E-H) The evolution of microstructure during densification of initially spherical glass particles (Chapter 4.1). These images also appear in Vasseur et al. [2016].

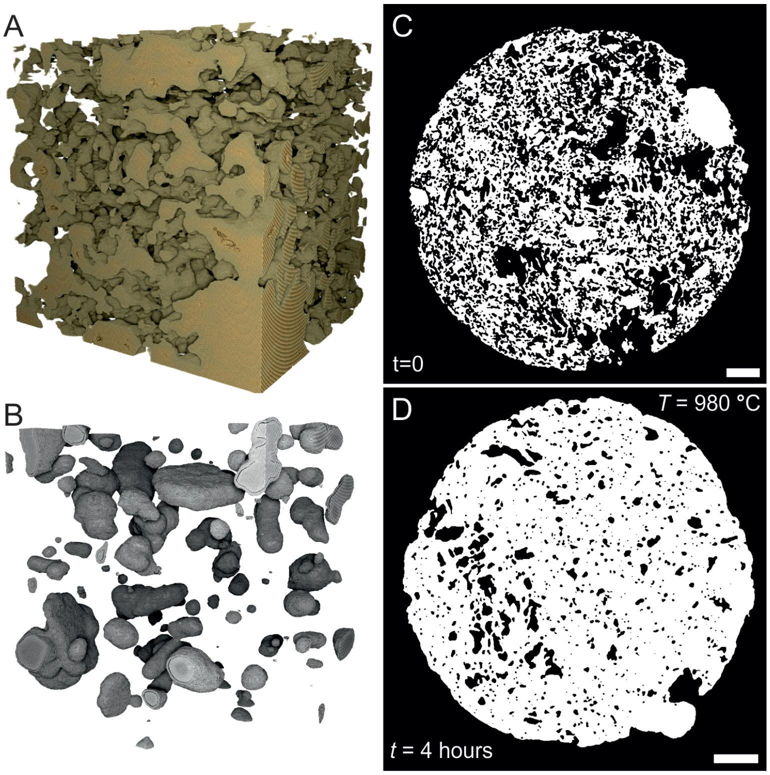

Figure 4.20: (A-B) 3D rendering of computed tomography data for (A) the segmented pore phase, and (B) the segmented crystal phase. Not shown in (A-B) is therefore the glass phase (liquid at high temperature). The edge length of the 3D rendering is $2\,\mathrm{mm}$. (C-D) 2D rendering of the computed tomography data the Θ-plane (*see* Chapter 2) for which the scale bar marks $1\,\mathrm{mm}$ and the black colour represents the pore phase while the white colour represents the glass and the crystals (solid phases). (C) The pre-experimental sample, and (D) the same sample after experimentation at $1253\,\mathrm{K}$ for $4\,\mathrm{hours}$.

regardless of geometry (Figure 4.19). The vented bubble model explicitly predicts a decrease of the pore size with time such that it is this parameter $a(t)$ that is scaled to account for the observable $\phi(t)$. The microstructural observations are consistent with the model. Furthermore, it is a decrease of pore size a that is thought to correlate with changes in other physical properties such as strength of the material [Vasseur et al., 2013, 2015]. These consequences will be discussed in Chapter 6.

The data presented in Figure 4.17 represent a proposed extension of the vented bubble model to porous magmas. This would represent a generalization of the model to all magmatic systems that are initially permeable to pore fluids. In Figure 4.20 I show the internal structure of these same pumice samples prior to and after experimentation. While the crystal phase remains unchanged, the pore phase has diminished, as predicted. Pore walls have thickened and the complex pore structure more resembles isolated bubbles by the time volume equilibrium is reached at ϕ_f.

They think they know those regions of the Earth

which never can be seen...

from having kindled a fire...

and looked into the bottom of a little crucible.

James Hutton

5

Discussion: Permeable outgassing

As porosity decreases during densification, so must the system permeability. This assertion is implicit in any of the wide range of solutions for the relationship between ϕ and the fluid permeability k. In this chapter I will first discuss how to scale ϕ with k across any densifying system of viscous droplets.

Then I will provide arguments for how the kinetics in Chapter 4 can be coupled with this scaling in order to explore, for the first time, the kinetics of changes in k as a function of time t. It is this extension of densification models that opens a new field of competing physical processes; namely, the outgassing process, which must inevitably become impossible as the system becomes impermeable, and the sintering viscous process, which acts to move liquid mass into the pore spaces. These kinetics are of direct importance in many areas of research; not least, volcanoscience. This is because it is the gas-permeability which has a first-order role to play in modulating the explosive potential of magma. This implication will be discussed at length in this chapter. Finally, I will provide a scaling between buoyancy-driven outgassing, termed compaction, and viscous sintering under surface tension which may serve as a full densification map for magmas at shallow depths. This map could be used to predict the timescale over which magmas can remain permeable in the shallow crust.

5.1 Scaling the permeability of densifying systems

The first step is to find a scaling between the system porosity ϕ and the system permeability k. Many such scaling laws have been suggested and, in their most simple form, these are power laws such that $k \propto k_r(\phi/\phi_r)^\zeta$ where r and ϕ_r are reference values which need to be calibrated, and ζ is an unknown exponent [*e.g.* Fowler & Yang, 1998]. However, such simple scaling attempts rely on empirical experimental work to provide a functional relationship between k_r, ϕ_r and n. The dominant parameter ζ has been constrained to be between 2 and 30 [Connolly

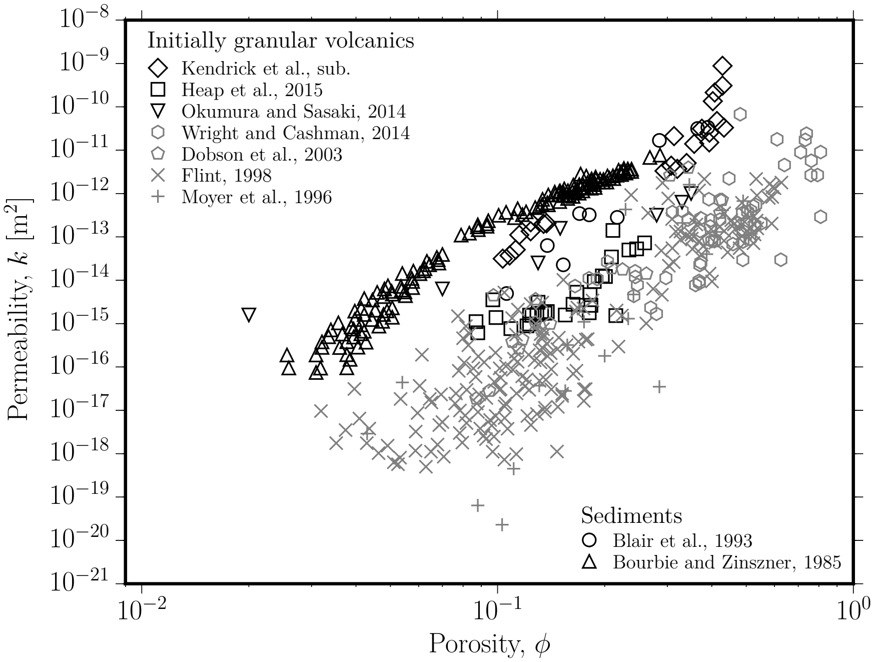

Figure 5.1: Bulk porosity and permeability of samples that underwent the granular to non-granular transition during volcanic welding or sedimentary diagenesis. Data in black are associated with sufficient information for subsequent analysis. Data are from a range of sources [Bourbie & Zinszner, 1985; Wright & Cashman, 2014; Blair et al., 1993; Heap et al., 2015; Dobson et al., 2003; Flint, 1998; Moyer et al., 1996]

et al., 2009], which is a huge range.

Contrastingly, the Kozeny-Carman relation $k = \phi^3/(2s^2)$ relates k to the specific surface area of the pore phase, which is the surface area relative to the entire system volume. This scaling has proved to be useful but not universal across all values of ϕ for any system [Martys et al., 1994].

The most promising scaling that has been proposed has been that of Martys et al. [1994] which, again, relates k to ϕ via s. Here, additionally, ϕ is reduced to an approximate value of connected porosity Φ by removing the final isolated percolation porosity, which is here termed ϕ_c (identical to the ϕ_f that was discussed when the kinetic component of densification was constrained). The Martys et al. [1994] relation is

$$k = \frac{2\phi_*}{s^2}(\phi - \phi_c)^\zeta \tag{5.1}$$

for which

$$\phi_* = 1 - (\phi - \phi_c) \tag{5.2}$$

To test the validity of this relationship, I collate literature data for k and ϕ for any rocks where I can show that the initial material state was granular. That is, rocks that are formed through deposition of particles followed by varying degrees of subsequent densification. Examples are sandstones [Bourbie & Zinszner, 1985], variably welded ignimbrites [Wright & Cashman, 2014], sintered glasses [Blair et al., 1993] and sintered volcanic ash [Okumura & Sasaki, 2014]. These are presented in raw form in Figure 5.1.

For the data from Blair et al. [1993], the value of s is measured. However, for all other data, this parameter is unknown. For the least densified samples – those which approximate a deposit of particles at or above some maximum packing porosity – the relationship for s as a function of the particle size R is simply geometrical as follows

$$s(R) = \frac{3(1-\phi)}{R} \tag{5.3}$$

However, to relate s to the pore size a, which is more likely to be valid when densification has proceeded to some degree beyond the initial case, this is more involved. Here I can rely again on the microstructural indicators defined in detail in Chapter 3.4 to constrain this. Once $a(R)$ is defined following Chapter 3.4 and Figure 3.11, I must decide if the particles and the pores are overlapping or if they are approximately hard spheres. In the former case, the relationship is given by [Torquato, 2013]

$$s(a) = \frac{3(1-\phi)\ln(1-\phi)}{a} \tag{5.4}$$

and in the latter case, Eq. 5.3 can be used but for which R is replaced by a and $(1-\phi)$ is replaced by ϕ. Finally, if we rather think the system is described by overlapping particles, rather than by overlapping pores, then the relationship is

$$s(R) = \frac{3\phi\ln\phi}{R} \tag{5.5}$$

which is the same as in Eq. 5.4 but where $(1-\phi)$ and a are replaced by ϕ and R, respectively.

Using the above constraints on s, and the constraints on ϕ_c and a described in Chapters 4 & 3.4, respectively, the data can be normalized as in Figure 5.2. The parameters are summarized in Table 5.1. The curve through the data is for Eq. 5.2 for which I follow exactly the constraint of Martys et al. [1994] in defining ζ as 4.2. Therefore, these data are not fit whatsoever and the collapse and agreement with Martys et al. [1994] is promising.

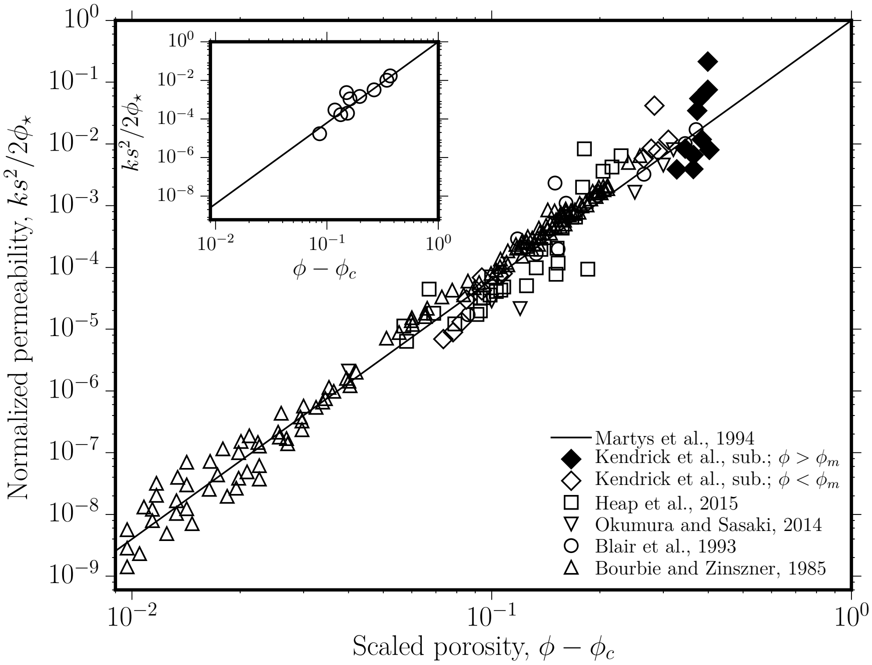

Figure 5.2: The universal scaling of fluid permeability in rocks across the granular to non-granular transition (via Eq. 5.2) using either the measured s or, if unknown, the calculated evolution of s during densification showing good agreement without any fitting parameters ($r^2 = 0.96$) over a large range of normalized permeability. *Inset*: The data from Blair et al. [1993] for which s was measured directly by image analysis. See Table 5.1 for the samples and parameters used and the references cited.

Alternative scaling arguments can be tested with the same datasets. First, a Stokes scaling (for a Stokes permeability k_s) in which

$$k_s = \frac{2R^2}{9(1-\phi)}(\phi - \phi_c) \tag{5.6}$$

derived for dispersions of particles in a gas phase, yields the scaling shown in Figure 5.3. I note that this is far less effective in describing the full range of data than the scaling from Martys et al. [1994].

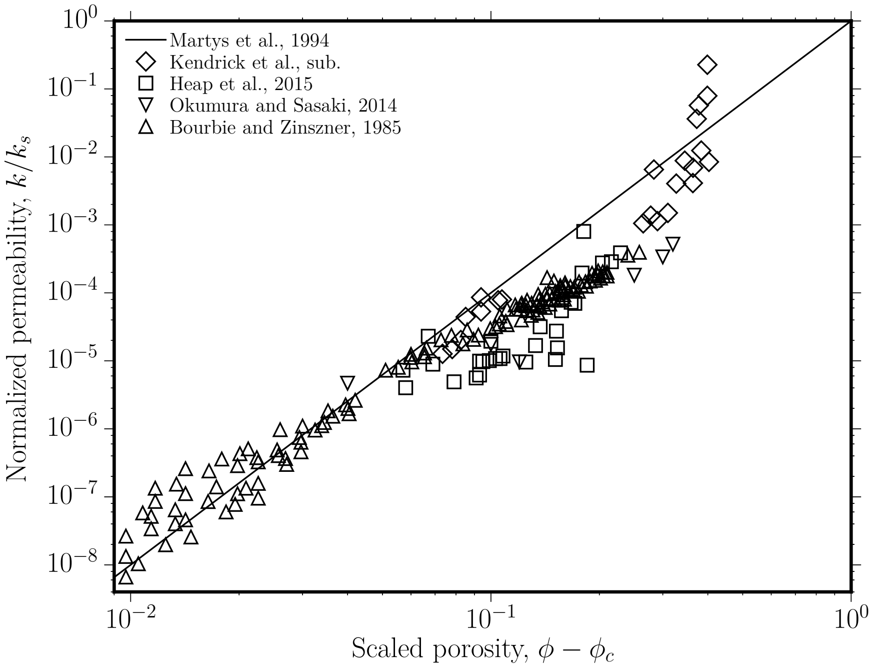

Figure 5.3: The data from Figure 5.1 but scaled using Eq. 5.6.

Finally, variations on the definition of s based on whether the pores or particles are selected and whether those elements are overlapping or not are tested in Figure 5.4. I conclude that the result presented in Figure 5.2 is the most effective.

5.2 Simulating permeable flow in 3D

Using the 4D datasets collected at the TOMCAT X-ray beamline of the Swiss Light Source, and using the numerical lattice-Boltzmann fluid flow simulation tool LBflow [Llewellin, 2010], I can predict the evolution of k with $\bar{t_b}$. To do this, I run simulations following the method outlined in Llewellin [2010] for each 3D dataset. In essence, this procedure populated the gas phase between the sintering

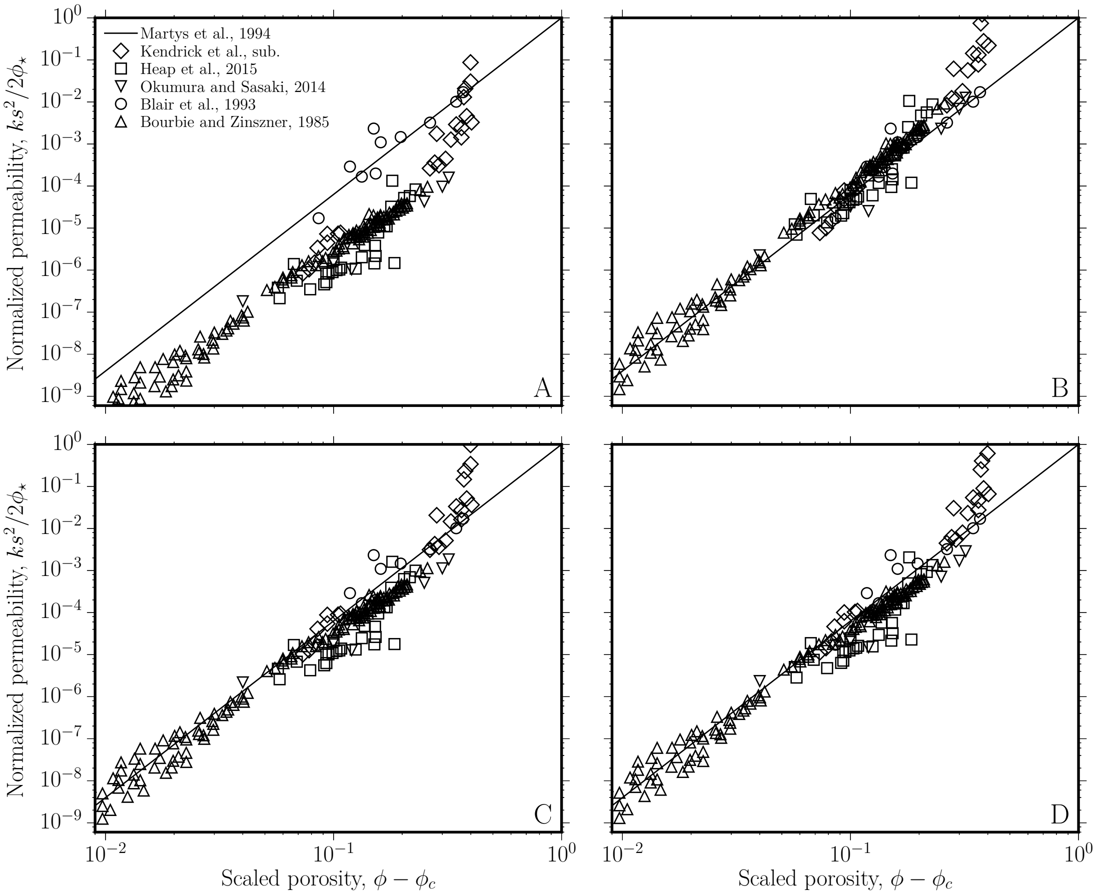

Figure 5.4: The same scaling as presented in Figure 5.2, but for where the definition of s is varied. (A) The case where s is computed from R and where the particles are overlapping. (B) The case where s is computed from a and where both the particles and the pores are considered as hard non-overlapping spheres. (C) The case where s is calculated from a and where both the particles and the pores are overlapping. (D) The case where s is calculated from a and the particles are overlapping but the pores are not.

glass beads with fluid nodes. Each simulation iteration involves the computation of the local gas velocity by the lattice Bolzmann method and the full methodology is described in detail in Llewellin [2010]. This method has the implication that the

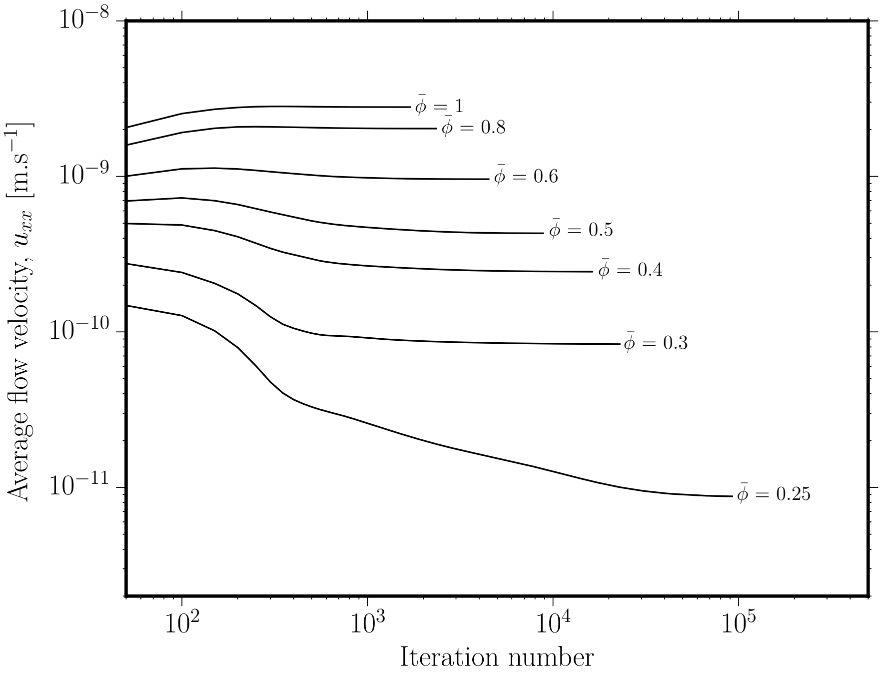

Figure 5.5: The results of using LBflow [Llewellin, 2010] to simulate the fluid flow through sintering glass bead packs that have densified to variable porosities (labelled as $\bar{\phi}$). The driving pressure gradient in this case was $\sim 0.1\,\mathrm{Pa\,m^{-1}}$.

permeable flow is decoupled from the sintering because the simulation is performed *ex situ* after the sintering has occurred. The pressure driving the simulated fluid is exerted at one edge of the box subvolume of the full 3D dataset. Then the average fluid velocity in the direction in which the driving pressure is applied is recorded. This is noted as $\langle u_{xx} \rangle$, $\langle u_{yy} \rangle$, $\langle u_{zz} \rangle$ in a Cartesian coordinate system such as that used here. This is also useful for determining isotropy during sintering because, for a given driving fluid pressure, I would expect the same average fluid velocity in each direction. Permeability is then calculated from the length of the sub-volume, the fluid velocity term and the driving pressure using Darcy's law. Computations

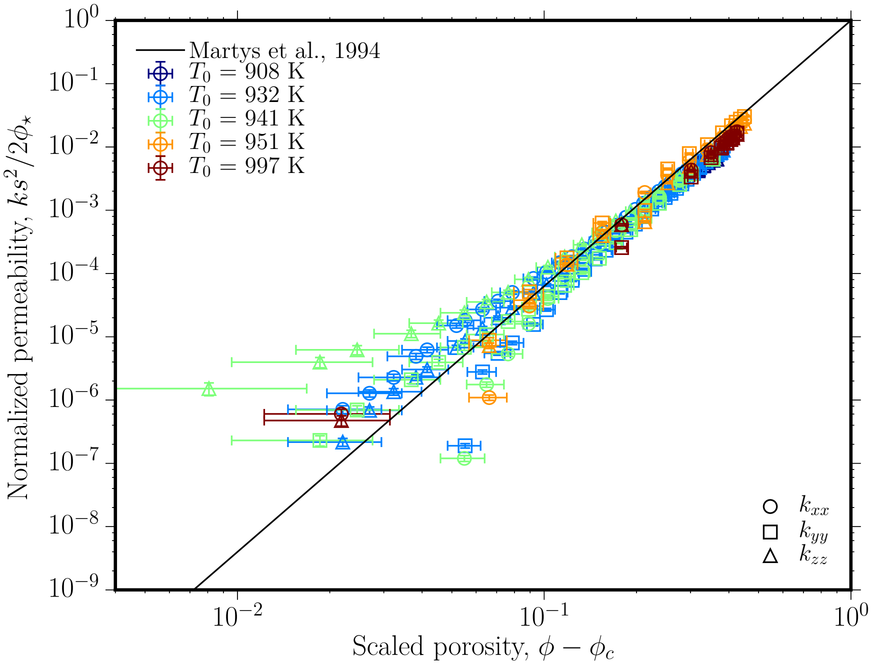

Figure 5.6: The scaling found by Martys et al. [1994] applied to the glass bead packs sintered at the TOMCAT beamline *in situ*.

are always independent of the fluid driving pressure such that creeping flow is maintained and a steady-flow criterion is applied which requires that the average fluid-speed does not vary by a critical value over 50 iterations (assessed two times consecutively; 100 iterations total) for the simulation to be rendered complete. The results for the example of $\langle u_{xx} \rangle$ are presented in Figure 5.5 for which the final data point is that which is used in the computation of the permeability.

The resultant permeability, a vector quantity that I present in each principle direction as k_{xx}, k_{yy}, and k_{zz} can then be normalized following Eq. 5.2 as was done with natural data above. To do this the surface area internal to the sample is measured using an algorithm similar to that available in the software Avizo^{TM}. The

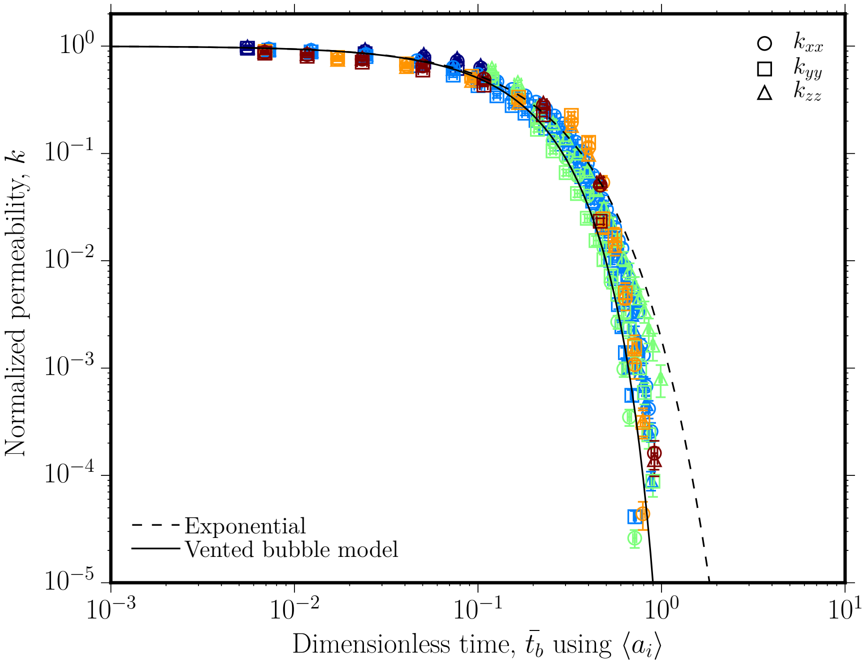

Figure 5.7: The evolution of normalized permeability $\bar{k}$ with time $\bar{t}_b$ for the data for glass beads sintering *in situ* at the TOMCAT beamline of the Swiss Light Source synchrotron. The adapted vented bubble model is shown for comparison.

scaling achieved is shown in Figure 5.6. This again demonstrates that the scaling proposed by Martys et al. [1994] is a good description for these isotropic materials. It further implies that the sintering process does indeed maintain isotropy of the pore network even down to low permeabilities.

5.3 The kinetics of permeability changes

I have shown how porosity evolves with time (Chapter 4) and how porosity is used to scale to permeability. Combining these two concepts yields a model by which permeability is a function of time. To do this I normalize k by the initial

k_i, to give $\bar{k}$ and then I convert this to a function of $\bar{\phi}$ using Eq. 5.2. This gives $\bar{k} = \bar{\phi}^{\zeta}$ and again, the calibrated value $\zeta = 4.2$ [Martys et al., 1994] permits me to plot $\bar{k}$ as a function of $\bar{t_b}$. Figure 5.7 shows the results of this conversion. Here the simulated permeability is converted to $\bar{k}$ by its initial value. Independently, the vented bubble model is plotted and shows excellent agreement without fitting. This also shows that permeability collapses toward zero at a finite $\bar{t_b}$ at which ϕ_f is achieved. This is in agreement with Figure 4.13. Finally, I note that isotropy of permeability is indeed maintained down to the percolation threshold.

5.4 Summary of this chapter: Volcanic implications and a volcano-densification map

In this chapter I have extended densification models to account for permeability. This provides a versatile tool when considering a volcano in which porosity is only transient in the permeable upper parts of a silicic volcanic conduit. The collapse of all densification data by a single timescale λ_b, is a powerful tool for volcanologists to scale processes that might be controlled by the time-dependent reduction in permeability. For example, in the uppermost conduit of Soufriere Hills volcano, degassing is thought to occur through permeable magma itself [Edmonds & Herd, 2007]. Degassing cycles in recorded SO_2 flux would be a good observable to normalize by λ_b to see if a universal description can be achieved. To do this, one would need to know the viscosity and the pore network lengthscale involved in the densification, both of which can be predicted for a particular magma.

A key consideration is the permeability-limit on densification when pressure is

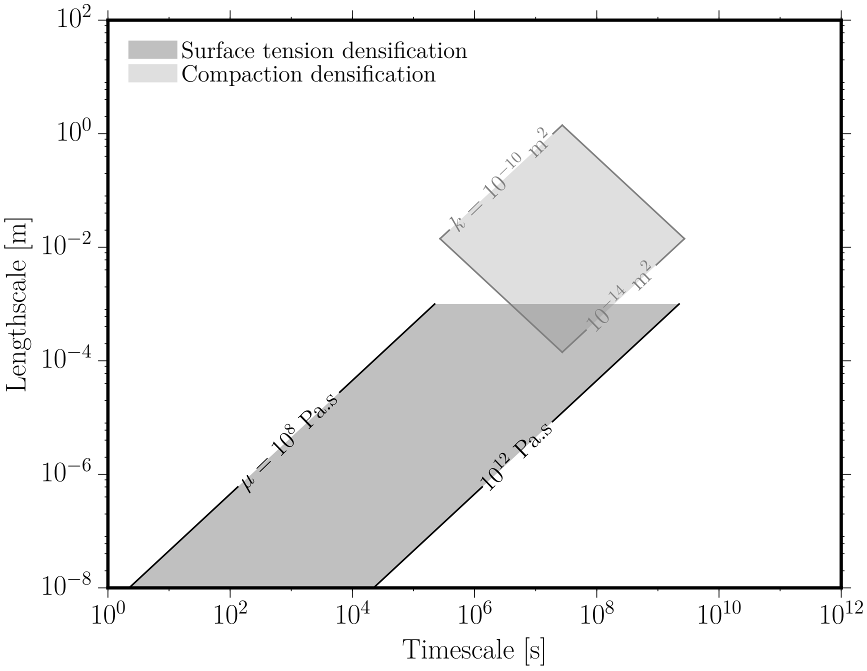

Figure 5.8: The windows for magmatic densification processes when they are driven by either surface tension processes (small lengthscales) or Darcian compaction dynamics (large lengthscales). This map can be used to predict the timescales involved in a magmatic densification process when the material properties are known.

involved. This is called compaction and occurs on a timescale λ_{Da} and a lengthscale L_{Da} that can be predicted by Darcy's law. The implication is that if the timescale or lengthscale of observation are greater than these critical time and lengthscales, then compaction effects may dominate over the high-permeability end member of densification processes. These critical values are

$$L_{Da} = \sqrt{k_i \frac{\mu}{\mu_g}} \tag{5.7}$$

and

$$\lambda_{Da} = \frac{1}{\rho g}\sqrt{\frac{\mu_g \mu}{k_i}} \tag{5.8}$$

If I take a range of values for magma permeabilities of $10^{-14} < k < 10^{-10}$ m^2 Mueller et al. [2005] and a range of magma viscosities $10^8 < \mu < 10^{12}$ Pa s, I can map out a region of L_{Da} and λ_{Da} in which magmas most commonly reside. Furthermore, I can plot the region for the surface-tension driven densification end-member process for the same range of viscosities. In Figure 5.8 I show these windows of densification which may prove useful to volcano scientists who wish to predict the timescale involved in a densification process based on a few simple material constraints.

Table 5.1: Summary of the samples used in the scaling of permeability for granular and densified rocks; Fig. 5.2

reference	R	a	ϕ_c	data type	comment
–	µm	µm	–	–	–
J. Kendrick data	100	14.5	0.03	Experimental	Crushed andesite from the 2012 lava dome at Volcán de Colima
Okumura & Sasaki [2014]	75, 250	8.02, 26.7	0.03	Experimental	Wadatouge rhyolitic obsidian
Heap et al. [2015]	25	1.8	0.03	Natural	Welded block and ash flow deposit from Mt. Meager
Bourbie & Zinszner [1985]	250	20.4	0.03	Natural	Fontainbleu sandstone
Blair et al. [1993]	–	–	0.03	Natural & experimental	Sintered glass beads & sandstones

The promise is kept. The masterwork is made.

John Tams, in review of *The Wrong Sunshine* by
Ray Hearne

6

Conclusions and outlook

In this thesis, I have explored densification processes in viscous liquids that are initially permeable, with special focus on volcanically-relevant examples. In the introduction I summarized some motivating problems that remain unconstrained about how magmas can outgas volatiles and what timescales might be involved in this process. In the following chapters I focus on constraining exactly these timescales, showing how pressure, water content and crystal content – key parameters in the magmatic system – can modify this timescale. It is this densification timescale that might prove key in assessing the propensity of magmas to build gas pressure and to fracture in the most catastophic eruptions. Here, by way of conclusion, I provide additional consequences of the work in this thesis which may prove to be fruitful future lines of investigation. Where possible, I lay out how experimental work could be conducted to test these ideas or which natural phenomena might be pertinent to interrogate further.

6.1 Volcanic implications

First and foremost, densification of magma has a large effect on the material strength, regardless of the loading conditions [Vasseur et al., 2013, 2015; Heap et al., 2015]. This means that as magma outgases and densifies, the stress required to fracture it in catastrophic explosive events becomes large compared with the pre-densification strength. Simultaneously, the pressure in the gas phase is likely to drop during outgassing [*see* Edmonds & Herd, 2007], which means that the stress available to drive fracturing drops. We can see conceptually that there will be scenarios in which highly porous magma will repetitively fracture without time sufficient for densification; and other scenarios in which densification can occur sufficiently fast such that both the strength increases and the pressure drops, yielding a stable system that will not break until the next pressure-building cycle occurs. Heap et al. [2015] explored this explicitly by comparing the evolution of strength with the evolution of permeability. However, it remains to be constrained how these two parameters compete to result in explosive fragmentation or not. The ideal experimental investigation would be to deform high viscosity permeable liquids in a triaxial deformation apparatus [*such as that used in* Benson et al., 2008] during dynamic fluid flow conditions through the porous network. The result would be a phase diagram in which large fluid flow timescales compared with densification timescales would result in stability, whereas small fluid flow timescales compared with densification would result in explosions.

Another consequence of the work provided herein is that diffusive mass transfer, in particular that of water (Chapter 2) can compete with densification. Work on the diffusive hydration of volcanic liquids during cooling [McIntosh et al., 2014] shows that this can result in large volume changes in the gas phase. It's clear that whether hydration or dehydration is occurring coincident with densification, the kinetics of bulk system-volume changes will be either enhanced or retarded. The complexity arises when we consider the fluxing effect of water hydration on the liquid viscosity [Hess & Dingwell, 1996]. As with the strength scenario, there will be hydration rates that lead to run-away densification rates as there will be dehydration scenarios that can thrust the liquid through the glass transition kinetic boundary, halting viscous flow altogether, and preserve higher porosities than anticipated. In concert these complexities yield a dynamic picture of upper-conduit conditions in volcanoes and serve to remind us how unconstrained the problem remains.

Both of the above processes – strength recovery and diffusion – compete with densification. The textural record discussed in Chapter 1 in which particulate volcanic ash is partially sintered in tuffisite cracks in otherwise dense volcanic rock [Tuffen et al., 2003; Tuffen & Dingwell, 2005; Berlo et al., 2013] have complex diffusion-driven gradients of water toward the bounding crack interfaces and are variably strong. And the evidence that these fracutre-degassing processes occur repeatedly [Tuffen et al., 2003; Castro et al., 2012] clearly demonstrates that conditions for explosive fracturing are met multiple times during ascent to the surface. Future work could constrain the minimum inter-fracture time required for diffusion of water and densification to render further fracturing impossible for the conditions tested.

6.2 Sintering and densification in antiquity and the Iron Age engineers

An altogether different application of the results presented in this thesis is one that relates to a phenomenon prevalent in the European Iron Age. Namely, that of vitrified forts in which prodigious evidence suggests that human-made fort walls were burned at high temperature for prolonged periods (up to ~ 48 hours) until partial melting of the stonework occurred and fluidal behaviour of parts of the walls was induced [Friend et al., 2007, 2008; Childe & Thorneycroft, 1938b,a; Ralston, 1986; Nisbet, 1974]. Concensus has converged on a destructive motive for these processes in which it is envisioned that fort-attackers burned the walls to weaken them [MacKie, 1969]. However, based on the evidence for sintering-induced strength-recovery in molten and partially molten particulate materials

[Vasseur et al., 2013; Heap et al., 2015], it's more likely that the walls became much stronger as a function of the kinetics of densification. This is more consistent with the observations that the large blocks in these walls remain much less affected than the small granular material in the wall interstices, which is sintered, glassy and dense [Youngblood et al., 1978]. If true, this would mean that it is more likely that the fort-wall was burned intentionally and may provide support for an alternative hypothesis: that Iron Age fort vitrification was an engineering solution to the problem of building large walls before mortar-technology. This would be another application of densification theory that would be ripe for further study. I do not present my work which contributes to this field [*see* Wadsworth et al., 2015; **?**] in this thesis, but mention of the extension to other realms of investigation of the densification models proposed is warranted.

6.3 Outlook and future directions

Future experimental work that would be essential to further the constraints provided herein can be summarized as follows

- It remains an outstanding question how particle shape and polydispersivity affect sintering rates. Herein I test some values and find moderate differences from the spherical case. But natural volcanic ash straddles a much wider geometric range which could be tested systematically.
- Sintering under variable loading conditions to test the proposed effect of pressure on sintering. Most important would be the hydrostatic case, fol-

lowed by sintering under differential stresses such that anisotropy development would be increasingly a component of the shear-enhanced compaction. This could be done in high temperature triaxial conditions [Benson et al., 2008] and in a rotary shear device [Lavallée et al., 2012].

- Densification of hydrous materials in regimes in which they either nucleate additional gas phases during the densification (particles larger than a diffusion length) or in which they diffusively degas (particles small than a diffusion length). This would couple several physical processes each of which has volcanic relevance.

References

Alidibirov, M. & Dingwell, D. B. (1996). Magma fragmentation by rapid decompression. *Nature*, 380(6570), 146–148.

Bagdassarov, N., Dorfman, A., & Dingwell, D. B. (2000). Effect of alkalis, phosphorus, and water on the surface tension of haplogranite melt. *American Mineralogist*, 85(1), 33–40.

Bagdassarov, N. S., Dingwell, D. B., & Webb, S. L. (1994). Viscoelasticity of crystal-and bubble-bearing rhyolite melts. *Physics of the earth and planetary interiors*, 83(2), 83–99.

Baker, D., Brun, F., & O'Shaughnessy, C. (2012). A four-dimensional X-ray tomographic microscopy study of bubble growth in basaltic foam. *Nature ...*.

Benson, P., Vinciguerra, S., Meredith, P., & Young, R. (2008). Laboratory simulation of volcano seismicity. *Science*, 322(5899), 249–252.

Berlo, K., Tuffen, H., Smith, V. C., Castro, J. M., Pyle, D. M., Mather, T. A., & Geraki, K. (2013). Element variations in rhyolitic magma resulting from gas transport. *Geochimica et cosmochimica acta*, 121, 436–451.

Blair, S. C., Berge, P. A., & Berryman, J. G. (1993). *Two-point correlation functions to characterize microgeometry and estimate permeabilities of synthetic and natural sandstones*. Technical report.

Blower, J. (2001). Factors controlling permeability–porosity relationships in magma. *Bulletin of Volcanology*, 63(7), 497–504.

Bourbie, T. & Zinszner, B. (1985). Hydraulic and acoustic properties as a function of porosity in Fontainebleau sandstone. *Journal of Geophysical Research: Solid Earth (1978–2012)*, 90(B13), 11524–11532.

Cabrera, A., Weinberg, R. F., Wright, H. M. N., Zlotnik, S., & Cas, R. A. F. (2011). Melt fracturing and healing: A mechanism for degassing and origin of silicic obsidian. *Geology*, 39(1), 67–70.

Castro, J. M., Bindeman, I. N., Tuffen, H., & Schipper, C. I. (2014). Explosive origin of silicic lava: Textural and δD–H2O evidence for pyroclastic degassing during rhyolite effusion. *Earth and Planetary Science Letters*, 405, 52–61.

Castro, J. M., Cordonnier, B., Tuffen, H., Tobin, M. J., Puskar, L., Martin, M. C., & Bechtel, H. A. (2012). The role of melt-fracture degassing in defusing explosive rhyolite eruptions at volcán Chaitén. *Earth and Planetary Science Letters*, 333(0), 63–69.

Castro, J. M. & Dingwell, D. B. (2009). Rapid ascent of rhyolitic magma at Chaitén Volcano, Chile. *Nature*, 461(7265), 780–783.

Chiang, Y.-M., Birnie, D. P., & Kingery, W. D. (1997). *Physical ceramics.* J. Wiley NY.

Childe, V. G. & Thorneycroft, W. (1938a). *The experimental production of the phenomena distinctive of vitrified forts.*

Childe, V. G. & Thorneycroft, W. (1938b). *The vitrified fort at Rahoy, Morvern, Argyll.*

Cimarelli, C., Costa, A., Mueller, S., & Mader, H. M. (2011). Rheology of magmas with bimodal crystal size and shape distributions: Insights from analog experiments. *Geochemistry Geophysics Geosystems*, 12.

Clarke, A. B., Stephens, S., Teasdale, R., Sparks, R. S. J., & Diller, K. (2007). Petrologic constraints on the decompression history of magma prior to Vulcanian explosions at the Soufrière Hills volcano, Montserrat. *Journal of Volcanology and Geothermal Research*, 161(4), 261–274.

Connolly, J. A. D., Schmidt, M. W., Solferino, G., & Bagdassarov, N. (2009). Permeability of asthenospheric mantle and melt extraction rates at mid-ocean ridges. *Nature*, 462(7270), 209–212.

Connor, C. B., Lichtner, P. C., Conway, F. M., Hill, B. E., Ovsyannikov, A. A., Federchenko, I., Doubik, Y., Shapar, V. N., & Taran, Y. A. (1997). Cooling of an igneous dike 20 yr after intrusion. *Geology*, 25(8), 711–714.

Costa, A., Melnik, O., Sparks, R. S. J., & Voight, B. (2007). Control of magma flow in dykes on cyclic lava dome extrusion. *Geophysical Research Letters*, 34(2).

Crank, J. (1975). The mathematics of diffusion.

Diller, K., Clarke, A. B., Voight, B., & Neri, A. (2006). Mechanisms of conduit plug formation: Implications for vulcanian explosions. *Geophysical Research Letters*, 33(20).

Dingwell, D., Brearley, M., & Dickinson, J. (1988). Melt densities in the Na 2 O-FeO-Fe 2 O 3-SiO 2 system and the partial molar volume of tetrahedrally-coordinated ferric iron in silicate melts. *Geochimica et Cosmochimica Acta*.

Dingwell, D. B. (1996). Volcanic dilemma: Flow or blow? *Science*, 273(5278), 1054–1055.

Dingwell, D. B. & Webb, S. L. (1989). Structural relaxation in silicate melts and non-Newtonian melt rheology in geologic processes. *Physics and Chemistry of Minerals*, 16(5), 508–516.

Dingwell, D. B. & Webb, S. L. (1990). Relaxation in silicate melts. *European journal of mineralogy*, (4), 427–449.

Dobson, P. F., Kneafsey, T. J., Hulen, J., & Simmons, A. (2003). Porosity, permeability, and fluid flow in the Yellowstone geothermal system, Wyoming. *Journal of Volcanology and Geothermal Research*, 123(3), 313–324.

Eberstein, M., Reinsch, S., Müller, R., Deubener, J., & Schiller, W. A. (2009). Sintering of glass matrix composites with small rigid inclusions. *Journal of the European Ceramic Society*, 29(12), 2469–2479.

Edmonds, M. & Herd, R. A. (2007). A volcanic degassing event at the explosive-effusive transition. *Geophysical Research Letters*, 34(21).

Fife, J. L., Rappaz, M., Pistone, M., Celcer, T., Mikuljan, G., & Stampanoni, M. (2012). Development of a laser-based heating system for in situ synchrotron-based X-ray tomographic microscopy. *Journal of synchrotron radiation*, 19(3), 352–358.

Flint, L. E. (1998). *Characterization of hydrogeologic units using matrix properties, Yucca Mountain, Nevada*. US Department of the Interior, US Geological Survey.

Fluegel, A. (2007). Glass viscosity calculation based on a global statistical modelling approach. *Glass Technology-European Journal of Glass Science and Technology Part A*, 48(1), 13–30.

Fowler, A. C. & Yang, X.-S. (1998). Fast and slow compaction in sedimentary basins. *SIAM Journal on Applied Mathematics*, 59(1), 365–385.

Frenkel, J. (1945). Viscous flow of crystalline bodies under the action of surface tension. *J. Phys*, 9(5), 385–391.

Friend, C. R. L., Charnley, N. R., Clyne, H., & Dye, J. (2008). Experimentally produced glass compared with that occurring at The Torr, NW Scotland, UK: vitrification through biotite melting. *Journal of archaeological science*, 35(12), 3130–3143.

Friend, C. R. L., Dye, J., & Fowler, M. B. (2007). New field and geochemical evidence from vitrified forts in South Morar and Moidart, NW Scotland: further insight into melting and the process of vitrification. *Journal of archaeological science*, 34(10), 1685–1701.

Gardner, J. (2012). Surface tension and bubble nucleation in phonolite magmas. *Geochimica et Cosmochimica Acta*.

Gardner, J., Ketcham, R., & Moore, G. (2013). Surface tension of hydrous silicate melts: Constraints on the impact of melt composition. *Journal of Volcanology and Geothermal Research*.

Gardner, J. E. & Ketcham, R. A. (2011). Bubble nucleation in rhyolite and dacite melts: temperature dependence of surface tension. *Contributions to Mineralogy and Petrology*, 162(5), 929–943.

Giachetti, T., Burgisser, A., Arbaret, L., Druitt, T. H., & Kelfoun, K. (2011). Quantitative textural analysis of Vulcanian pyroclasts (Montserrat) using multiscale X-ray computed microtomography: comparison with results from 2D image analysis. *Bulletin of Volcanology*, 73(9), 1295–1309.

Giachetti, T., Druitt, T. H., Burgisser, A., Arbaret, L., & Galven, C. (2010). Bubble nucleation, growth and coalescence during the 1997 Vulcanian explosions of Soufriere Hills Volcano, Montserrat. *Journal of Volcanology and Geothermal Research*, 193(3-4), 215–231.

Giordano, D., Russell, J. K., & Dingwell, D. B. (2008). Viscosity of magmatic liquids: a model. *Earth and Planetary Science Letters*, 271(1), 123–134.

Gonnermann, H. M. (2014). Magma Fragmentation. *Annual Review of Earth and Planetary Sciences*, (0).

Gonnermann, H. M. & Manga, M. (2003). Explosive volcanism may not be an inevitable consequence of magma fragmentation. *Nature*, 426(6965), 432–435.

Gonnermann, H. M. & Manga, M. (2007). The Fluid Mechanics Inside a Volcano. *Annual Review of Fluid Mechanics*, 39(1), 321–356.

Gottsmann, J., Giordano, D., & Dingwell, D. B. (2002). Predicting shear viscosity during volcanic processes at the glass transition: a calorimetric calibration. *Earth and Planetary Science Letters*, 198(3), 417–427.

Heap, M. J., Farquharson, J. I., Wadsworth, F. B., Kolzenburg, S., & Russell, J. K. (2015). Timescales for permeability reduction and strength recovery in densifying magma. *Earth and Planetary Science Letters*.

Hess, K.-U. (1996). *Zur Temperaturabhängigkeit der Viskosität von haplogranitischen Schmelzen*. PhD thesis.

Hess, K. U. & Dingwell, D. B. (1996). Viscosities of hydrous leucogranitic melts: A non-Arrhenian model. *American Mineralogist*, 81(9-10), 1297–1300.

Kang, S.-J. L. (2004). *Sintering: densification, grain growth and microstructure*. Butterworth-Heinemann.

Kendrick, J. E., Lavallée, Y., Hess, K. U., Heap, M. J., Gaunt, H. E., Meredith, P. G., & Dingwell, D. B. (2013). Tracking the permeable porous network during strain-dependent magmatic flow. *Journal of Volcanology and Geothermal Research*, 260(0), 117–126.

Kennedy, B. M., Wadsworth, F. B., Vasseur, J., Ian Schipper, C., Mark Jellinek, A., von Aulock, F. W., Hess, K.-U., Kelly Russell, J., Lavallée, Y., Nichols, A. R., & Dingwell, D. B. (2016). Surface tension driven processes densify and retain permeability in magma and lava. *Earth and Planetary Science Letters*, 433, 116–124.

Klug, C. & Cashman, K. V. (1996). Permeability development in vesiculating magmas: implications for fragmentation. *Bulletin of Volcanology*, 58(2-3), 87–100.

Knoche, R., Dingwell, D., & Webb, S. (1995). Melt Densities for Leucogranites and Granitic Pegmatites: Partial Molar Volumes for SiO2, Al2O3, Na2O, K2O, Li2O, Rb2O, Cs2O, MgO, CaO, SrO, BaO, B2O. *Geochimica et cosmochimica acta.*

Koehler, S., Hilgenfeldt, S., & Stone, H. (2000). A generalized view of foam drainage: experiment and theory. *Langmuir.*

Kraxner, J., Liška, M., Klement, R., & Chromčíková, M. (2009). Surface tension of borosilicate melts with the composition close to the E-glass. *Ceramics-Silikáty*, 53(2), 141–143.

Kueppers, U., Perugini, D., & Dingwell, D. B. (2006). "Explosive energy" during volcanic eruptions from fractal analysis of pyroclasts. *Earth and Planetary Science Letters*, 248(3), 800–807.

Lange, R. A. & Carmichael, I. S. E. (1987). Densities of Na 2O-K 2O-MgO-MgO-FeO-Fe 2O 3-Al 3O 3-TiO 2-SiO 2 liquids: New measurements and derived partial molar properties. *Geochimica et cosmochimica acta*, 51, 2931–2946.

Lara, C., Pascual, M. J., Prado, M. O., & Duran, A. (2004). Sintering of glasses in the system RO–Al2O3–BaO–SiO2(R= Ca, Mg, Zn) studied by hot-stage microscopy. *Solid State Ionics*, 170(3), 201–208.

Lavallée, Y., Mitchell, T. M., Heap, M. J., Vasseur, J. J., Hess, K.-U., Hirose, T., Dingwell, D. B., Lavallee, Y., Mitchell, T. M., Heap, M. J., Vasseur, J. J., Hess, K.-U., Hirose, T., & Dingwell, D. B. (2012). Experimental generation of volcanic pseudotachylytes: Constraining rheology. *Journal of Structural Geology*, 38, 222–233.

Lavallée, Y., Wadsworth, F. B., Vasseur, J., Russell, J. K., Andrews, G. D. M., Hess, K.-U., von Aulock, F. W., Kendrick, J. E., Tuffen, H., & Biggin, A. (2015). Eruption and emplacement timescales of ignimbrite super-eruptions from thermo-kinetics of glass shards. *Frontiers in Earth Science*, 3, 2.

Llewellin, E. W. (2010). LBflow: An extensible lattice Boltzmann framework for the simulation of geophysical flows. Part II: usage and validation. *Computers & Geosciences*, 36(2), 115–122.

Llewellin, E. W., Mader, H. M., & Wilson, S. D. R. (2002). The rheology of a bubbly liquid. *Proceedings of the Royal Society of London. Series A: Mathematical, Physical and Engineering Sciences*, 458(2020), 987–1016.

Llewellin, E. W. & Manga, M. (2005). Bubble suspension rheology and implications for conduit flow. *Journal of Volcanology and Geothermal Research*, 143(1), 205–217.

Lowenstern, J. B., Bleick, H., Vazquez, J. A., Castro, J. M., & Larson, P. B. (2012). Degassing of Cl, F, Li, and Be during extrusion and crystallization of the rhyolite dome at Volcán Chaitén, Chile during 2008 and 2009. *Bulletin of Volcanology*, 74(10), 2303–2319.

Lu, B. & Torquato, S. (1992). Nearest-surface distribution functions for polydispersed particle systems. *Physical Review A*, 45(8), 5530.

Mackenzie, J. K. & Shuttleworth, R. (1949). A phenomenological theory of sintering. *Proceedings of the Physical Society. Section B*, 62(12), 833.

MacKie, E. W. (1969). Timber-laced and vitrified walls in Iron Age forts: causes of vitrification. *Glasgow Archaeological Journal*, (pp. 69–71).

Mader, H. M., Llewellin, E. W., & Mueller, S. P. (2013). The rheology of two-phase magmas: A review and analysis. *Journal of Volcanology and Geothermal Research*, 257, 135.

Martys, N. S., Torquato, S., & Bentz, D. P. (1994). Universal scaling of fluid permeability for sphere packings. *Physical Review E*, 50(1), 403.

Mason, R. M., Starostin, A. B., Melnik, O. E., & Sparks, R. S. J. (2006). From Vulcanian explosions to sustained explosive eruptions: the role of diffusive mass transfer in conduit flow dynamics. *Journal of Volcanology and Geothermal Research*, 153(1), 148–165.

McIntosh, I. M., Llewellin, E. W., Humphreys, M. C. S., Nichols, A. R. L., Burgisser, A., Schipper, C. I., & Larsen, J. F. (2014). Distribution of dissolved water in magmatic glass records growth and resorption of bubbles. *Earth and Planetary Science Letters*, 401, 1–11.

Melnik, O., Barmin, A. A., & Sparks, R. S. J. (2005). Dynamics of magma flow inside volcanic conduits with bubble overpressure buildup and gas loss through permeable magma. *Journal of Volcanology and Geothermal Research*, 143(1), 53–68.

Michaut, C., Bercovici, D., & Sparks, R. S. J. (2009). Ascent and compaction of gas rich magma and the effects of hysteretic permeability. *Earth and Planetary Science Letters*, 282(1), 258–267.

Moyer, T. C., Geslin, J. K., & Flint, L. E. (1996). *Stratigraphic relations and hydrologic properties of the Paintbrush Tuff nonwelded (PTn) hydrologic unit, Yucca Mountain, Nevada.* Technical report.

Mueller, S., Llewellin, E. W., & Mader, H. M. (2010). The rheology of suspensions of solid particles. *Proceedings of the Royal Society A: Mathematical, Physical and Engineering Science*, 466(2116), 1201–1228.

Mueller, S., Melnik, O., Spieler, O., Scheu, B., & Dingwell, D. B. (2005). Permeability and degassing of dome lavas undergoing rapid decompression: An experimental determination. *Bulletin of Volcanology*, 67(6), 526–538.

Mungall, J. E., Bagdassarov, N. S., Romano, C., & Dingwell, D. B. (1996). Numerical modelling of stress generation and microfracturing of vesicle walls in glassy rocks. *Journal of Volcanology and Geothermal Research*, 73(1), 33–46.

Nisbet, H. C. (1974). A geological approach to vitrified forts. *Sci. Archaeol*, 12, 3–12.

Okumura, S. & Sasaki, O. (2014). Permeability reduction of fractured rhyolite in volcanic conduits and its control on eruption cyclicity. *Geology*, 42(10), 843–846.

Oppenheimer, J., Rust, A., Cashman, K., & Sandnes, B. (2015). Gas migration regimes and outgassing in particle-rich suspensions. *Front. Phys.*, 3(60).

Prado, M., Dutra Zanotto, E., & Müller, R. (2001). Model for sintering polydispersed glass particles. *Journal of non-crystalline solids*, 279(2), 169–178.

Prado, M. O., Fredericci, C., & Zanotto, E. D. (2003a). Isothermal sintering with concurrent crystallization of polydispersed soda–lime–silica glass beads. *Journal of non-crystalline solids*, 331(1), 145–156.

Prado, M. O., Zanotto, E. D., & Fredericci, C. (2003b). Sintering polydispersed spherical glass particles. *Journal of materials research*, 18(06), 1347–1354.

Prousevitch, A. A., Sahagian, D. L., & Anderson, A. T. (1993). Dynamics of diffusive bubble growth in magmas: isothermal case. *Journal of Geophysical Research: Solid Earth (1978–2012)*, 98(B12), 22283–22307.

Proussevitch, A. A., Sahagian, D. L., & Kutolin, V. A. (1993). Stability of foams in silicate melts. *Journal of Volcanology and Geothermal Research*, 59(1), 161–178.

Quane, S. L. & Russell, J. K. (2003). Rock strength as a metric of welding intensity in pyroclastic deposits. *European journal of mineralogy*, 15(5), 855–864.

Quane, S. L. & Russell, J. K. (2005). Welding: insights from high-temperature analogue experiments. *Journal of Volcanology and Geothermal Research*, 142(1–2), 67–87.

Rallison, J. (1984). The deformation of small viscous drops and bubbles in shear flows. *Annual Review of Fluid Mechanics*.

Ralston, I. (1986). The Yorkshire Television vitrified wall experiment at East Tullos, City of Aberdeen District. In *Proceedings of the Society of Antiquaries of Scotland*, volume 116 (pp. 17–40).: National Museum of Antiquities of Scotland.

Rintoul, M. D. (2000). Precise determination of the void percolation threshold for two distributions of overlapping spheres. *Physical Review E*, 62(1), 68.

Russell, J. K. & Quane, S. L. (2005). Rheology of welding: inversion of field constraints. *Journal of Volcanology and Geothermal Research*, 142(1–2), 173–191.

Rust, A. C., Cashman, K. V., & Wallace, P. J. (2004). Magma degassing buffered by vapor flow through brecciated conduit margins. *Geology*, 32(4), 349–352.

Rust, A. C., Manga, M., & Cashman, K. V. (2003). Determining flow type, shear rate and shear stress in magmas from bubble shapes and orientations. *Journal of Volcanology and Geothermal Research*, 122(1–2), 111–132.

Schipper, C. I., Castro, J. M., Tuffen, H., James, M. R., & How, P. (2013). Shallow vent architecture during hybrid explosive–effusive activity at Cordón Caulle (Chile, 2011–12): Evidence from direct observations and pyroclast textures. *Journal of Volcanology and Geothermal Research*, 262, 25–37.

Schultz, G. V. (1939). Uber Die Kinetik Der Kettenpolymerisationen. *Z. Phys. Cheme, Leipzig*, 43, 25.

Shea, T., Houghton, B. F., Gurioli, L., Cashman, K. V., Hammer, J. E., & Hobden, B. J. (2010). Textural studies of vesicles in volcanic rocks: An integrated methodology. *Journal of Volcanology and Geothermal Research*, 190(3–4), 271–289.

Shelby, J. (2008). A limited review of water diffusivity and solubility in glasses and melts. *Journal of the American Ceramic Society*.

Soares, V. O., Reis, R. C. V. M., Zanotto, E. D., Pascual, M. J., & Duran, A. (2012). Non-isothermal sinter-crystallization of jagged Li2O–Al2O3–SiO2 glass and simulation using a modified form of the Clusters model. *Journal of non-crystalline solids*, 358(23), 3234.

Spieler, O., Kennedy, B., Kueppers, U., Dingwell, D. B., Scheu, B., & Taddeucci, J. (2004). The fragmentation threshold of pyroclastic rocks. *Earth and Planetary Science Letters*, 226(1), 139–148.

Stevenson, R. J., Dingwell, D. B., Webb, S. L., & Bagdassarov, N. S. (1995). The equivalence of enthalpy and shear stress relaxation in rhyolitic obsidians and quantification of the liquid-glass transition in volcanic processes. *Journal of Volcanology and Geothermal Research*, 68(4), 297–306.

Torquato, S. (2013). *Random heterogeneous materials: microstructure and macroscopic properties*, volume 16. Springer Science & Business Media.

Torquato, S. & Avellaneda, M. (1991). Diffusion and reaction in heterogeneous media: Pore size distribution, relaxation times, and mean survival time. *The Journal of Chemical Physics*, 95(9), 6477–6489.

Truby, J. M., Mueller, S. P., Llewellin, E. W., & Mader, H. M. (2015). The rheology of three-phase suspensions at low bubble capillary number. In *Proceedings of the Royal Society of London A: Mathematical, Physical and Engineering Sciences*, volume 471 (pp. 20140557).: The Royal Society.

Tuffen, H. & Dingwell, D. (2005). Fault textures in volcanic conduits: evidence for seismic trigger mechanisms during silicic eruptions. *Bulletin of Volcanology*, 67(4), 370–387.

Tuffen, H., Dingwell, D. B., & Pinkerton, H. (2003). Repeated fracture and healing of silicic magma generate flow banding and earthquakes? *Geology*, 31(12), 1089–1092.

Vasseur, J., Wadsworth, F., Lavallée, Y., & Dingwell, D. (2016). Dynamic elastic moduli during isotropic densification of initially granular media. *Geophysical Journal International*, 204, 1721–1728.

Vasseur, J., Wadsworth, F. B., Lavallée, Y., Bell, A. F., Main, I. G., & Dingwell, D. B. (2015). Heterogeneity: The key to failure forecasting. *Scientific reports*, 5.

Vasseur, J., Wadsworth, F. B., Lavallée, Y., Hess, K., & Dingwell, D. B. (2013). Volcanic sintering: Timescales of viscous densification and strength recovery. *Geophysical Research Letters*, 40(21), 5658–5664.

Wadsworth, F. B., Damby, D. E., Hearne, R. L., Le Blond, J. S., Vasseur, J., Najorka, J., Hess, K.-U., & Dingwell, D. B. (2015). The feasibility of vitrifying a sandstone enclosure in the British Iron Age. *Journal of Archaeological Science: Reports*.

Walker, D. & Mullins Jr, O. (1981). Surface tension of natural silicate melts from 1,200–1,500 C and implications for melt structure. *Contributions to Mineralogy and Petrology*, 76(4), 455–462.

Westrich, H. R. & Eichelberger, J. C. (1994). Gas transport and bubble collapse in rhyolitic magma: an experimental approach. *Bulletin of Volcanology*, 56(6-7), 447–458.

Wiederhorn, S. M. (1969). Fracture surface energy of glass. *Journal of the American Ceramic Society*, 52(2), 99–105.

Wright, H. M. & Cashman, K. V. (2014). Compaction and gas loss in welded pyroclastic deposits as revealed by porosity, permeability, and electrical conductivity measurements of the Shevlin Park Tuff. *Geological Society of America Bulletin*, 126(1-2), 234–247.

Youngblood, E., Fredriksson, B. J., Kraut, F., & Fredriksson, K. (1978). Celtic vitrified forts: implications of a chemical-petrological study of glasses and source rocks. *Journal of archaeological science*, 5(2), 99–121.

Zhang, Y. & Ni, H. (2010). Diffusion of H, C, and O components in silicate melts. *Reviews in Mineralogy and Geochemistry*, 72(1), 171–225.

Zhang, Y., Ni, H., & Chen, Y. (2010). Diffusion data in silicate melts. *Reviews in Mineralogy and Geochemistry*, 72(1), 311–408.

Zhang, Y., Stolper, E. M., & Wasserburg, G. J. (1991). Diffusion of a multi-species component and its role in oxygen and water transport in silicates. *Earth and Planetary Science Letters*, 103(1), 228–240.